

GOLD-SILICIDE EUTECTIC DYNAMICS OF
MESOTEXTURED MATERIALS AND THEIR
OPTICAL PROPERTIES

By

NATHAN PHILIP DICE

Bachelor of Science Physics
University Of Idaho
Moscow, Idaho
2018

Submitted to the Faculty of the
Graduate College of the
Oklahoma State University
in partial fulfillment of
the requirements for
the Degree of
DOCTOR OF PHILOSOPHY
May 2022

GOLD-SILICIDE EUTECTIC DYNAMICS OF
MESOTEXTURED MATERIALS AND THEIR
OPTICAL PROPERTIES

Dissertation Approved:

Dr. David McIlroy

Dissertation Adviser

Dr. Mario Borunda

Dr. Derek Meyers

Dr. Andrew Yost

Dr. John Ohara

To my wife Jessica and her endless love and support. Also, to our three children Tucker,
Lily and Violet.

Name: NATHAN PHILIP DICE

Date of Degree: MAY 2022

Title of Study: GOLD-SILICIDE EUTECTIC DYNAMICS OF MESOTEXTURED MATERIALS AND THEIR OPTICAL PROPERTIES

Major Field: PHYSICS

Abstract: Meso scaled pyramidal and inverse pyramidal structures, hereon referred to as Mesopyramids and Inverse Mesopyramids, are observed on Si[100] post annealing of a tri-layer of gold and silicon thin films. The structures are striated with a stochastic distribution of nano scaled plateaus and cavities. The cavities are on the order of tens of nano meters deep with a width up to a single micron. Growth of these pyramids is governed by the behavior of a eutectic under vacuo during annealing. The lattice structure of substrate plays an active role in the orientation of the array of mesopyramids on the silicon wafer. A native oxide promotes a wetting environment and acts as a barrier to diffusion of the eutectic into the silicon reservoir of the wafer. The quenching stage of pyramid fabrication initiates a final phase separation that results in the observed texturing. Dimensions of this texturing create optically active surfaces both in the far and near field. Diffraction patterns were generated with a beam of well collimated P-polarized light illuminating the concavity of the structures and the effect of the pyramid's rounded edges. Calculating the radius of curvature allows for these structures to be modeled as spherical mirrors and explains the magnification or minimization of the Fraunhofer pattern produced. This square aperture effect also facilitated the creation of a mathematical model which is in good agreement with the physical results. Performing near field analysis allowed for the confirmation both visually and spectrally of the effective coupling of energy from photons to surface plasmon modes. This energy is observed to propagate as surface plasmon polaritons in the cavities of the mesopyramid and down an individual facet for the inverse mesopyramid. The spectral data obtained confirmed the presence of band transitions for gold from d-band to sp-band at 550nm and 650 nm wavelengths of light. Back scattered light from these surface plasmon polaritons is analyzed as the average of the behavior at the gold-silicide dielectric interface. The opportunity to further develop these surfaces into optoelectronic devices as well as metalens materials provide impetus for this body of research.

TABLE OF CONTENTS

Chapter	Page
I. INTRODUCTION.....	1
II. EXPERIMENTAL METHODS.....	6
Section 1: Introduction.....	6
Section 2: Scanning Electron Microscope	7
Section 3: Energy Dispersive Spectroscopy	10
Section 4: Atomic Force Microscopy	25
Section 5: Magnetron Sputtering Thin Film Deposition	30
III. EXPLOITING EUTECTIC FORMATION AND PHASE SEPERATION TO PRODUCE PLASMONIC METAMATERIALS.....	33
Section 1: Introduction.....	33
Section 2: Methods	33
Section 3: Results.....	34
Section 4: Discussion	35
Section 5: Conclusion	43
IV. GOLD SILICIDE EUTECTIC DYNAMICS AND MESOPYRAMIDS FORMATION.....	44
Section 1: Introduction.....	44
Section 2: Au Mesopyramid Preparation	45
Section 3: Sample Characterization	47
Section 4: Results.....	48
Section 5: Discussion	53
Section 6: Conclusion	60
V. FAR-FIELD DIFFRACTION AND OPTICAL PROPERTIES FROM MESO- SCALED AU PYRAMIDS.....	62
Section 1: Introduction.....	62
Section 2: Materials Preparation and Experimental Details	63
Section 3: Results.....	65

Chapter	Page
Section 4: Discussion	70
Section 5: Conclusion	73
VI. SURFACE PLASMON POLARITON THEORY	75
Section 1: Introduction.....	75
Section 2: Maxwell's Equations and the Wave Equation	76
Section 3: SPP at the Dielectric Conductor Interface and the Dispersion Relation	80
Section 4: Mechanisms for SPP Coupling and Launching	82
VII. SPP Manuscript	84
Section 1: Introduction.....	84
Section 2: Experimental Setup	85
Section 3: Results.....	87
Section 4: Discussion	94
Section 5: Conclusion	97
VIII. CONCLUSION.....	99
REFERENCES	104
APPENDICES	119

LIST OF TABLES

Table	Page
2.1 Statistical data for EDS sample sights.	15
2.2 Statistical data for EDS map area.	19
2.3 Statistical Data of mesopyramid substrate interface.	22

LIST OF FIGURES

Figure	Page
2.1 Schematic of scanning electron microscope.	7
2.2 Mesopyramid SEM micrograph taken at 17 degrees with respect to the horizon with secondary electrons.	9
2.3 Spot EDS sample site of a mesopyramid.	12
2.4 EDS Spot Data.	13
2.5 EDS Spot Data.	14
2.6 Data for corresponding EDS spots on mesopyramid.	15
2.7 Elemental area map of a mesopyramid.	17
2.8 EDS split channel maps and corresponding data.	18
2.9 EDS area map of interface of a mesopyramid and substrate.	20
2.10 Split channel of area EDS map along with corresponding spectroscopic data.	21
2.11 EDS line scan report of a mesopyramid.	23
2.12 Basic schematic of AFM system.	25
2.13 AFM scanning a denuded zone with a mesopyramid centered.	27
2.14 AFM data for a single mesopyramid.	28
2.15 SEM/AFM Data set for a single mesopyramid.	29
2.16 Magnetron sputter system basic components.	31
2.17 Magnetron sputter head setup.	32
3.1(a) A SEM image of a large Au pyramid surrounded by a cluster of smaller Au pyramids, (b) a SEM image of a single Au pyramid, where the surface texturing is resolved, and (c) a high-resolution SEM image of an Au pyramid that was quickly quenched, where SP1 is a region where Si remained in what are usually cavities and SP2 is the typical Au rich region of the pyramid.	35
3.2 (a) Cross sectional SEM image of an Au pyramid, (b) an EDS map of Au pyramid-Si substrate interface, and (c) a SEM image of a partially formed pyramid that shows the etching of the Si(100) substrate caused by the formation of the Au-Si eutectic.	38
3.3(a) The scattering spectrum of an Au pyramid. (b) Far field specular data taken with the same light source.	40
3.4 Specular collected polarized light intensity as a function of polarization angle from the surface of a pyramid.	42
4.1 An SEM micrograph of a mesopyramid taken at 17 degrees with respect to the horizontal plane to illustrate the pyramid like geometry.	46

Figure	Page
4.2 An SEM top-down micrograph of a mesopyramid, where the crosses marked SP1 (channel) and SP2 (plateau) indicate the locations where EDS analysis was performed.....	49
4.3 An SEM micrograph of three aligned mesopyramids.....	50
4.4 An SEM micrograph of AuSi eutectic-induced etching of the Si substrate.	51
4.5 (a) An SEM micrograph of the cross section of an Au mesopyramid. The bright region above the pyramid is epoxy used to cast the sample for cross-sectioning. The dark regions within the pyramid are cavities that form due to phase separation of the AuSi eutectic. (b) The elemental at% line scan for Si and Au along and in the direction of the white arrow in (a).	52
4.6 A schematic diagram of the surface tensions of a liquid drop on a solid surface for non-wetting (top) and wetting (bottom) geometries. γ_{SL} , γ_{VL} , and γ_{SV} are the surface tensions at the solid-liquid, vapor-liquid, and solid-vapor interfaces, respectively.	53
4.7 Mesopyramid formation process: (a) Thin Au & Si film deposition. (b) Formation of eutectic at $T > T_E$. (c) Nucleation of mesopyramids at silicon oxide film defects (d) Etching along primary axis of Si substrate. (e) Mesopyramid growth due to Ostwald ripening. (f) During cool down phase separation occurs and a eutectic boundary layer forms at the interface of the two phases through which Si diffuses back into the Si Substrate. A native oxide at the Si surface is assumed but not shown.	56
4.8 AuSi phase diagram superimposed with experimental data.	57
5.1 Experimental setup used for the diffraction studies.....	64
5.2 (a) A SEM micrograph of the denuded zone with a Au mesopyramid at the center. (b) A high magnification SEM micrograph of the mesopyramid located in the center of the denuded zone in (a). (c) 3D rendering of the AFM imaging of the mesopyramid in (b). (d) The AFM line scan profile of the mesopyramid in (b), where the inset shows the location of the line scan on the mesopyramid. The dashed blue line is the calculated radius of curvature for the MP.	66
5.3 (a) An SEM image of the denuded zone with a Au inverse mesopyramid at the center. (b) A high magnification SEM of the Au inverse mesopyramid located in the center of the denuded zone in (a). (c) 3D rendering of the AFM data of the inverse mesopyramid in (b). (d) The AFM line scan profile of the inverse mesopyramid in (b), where the inset shows the location of the line scan on the inverse mesopyramid. The fit line is the calculated radius of curvature for the inverse mesopyramid.	67
5.4 (a) The diffraction pattern produced by the mesopyramid in Figure 2(b) and (b) is a 3D thermal map of the diffraction pattern. (c) The diffraction pattern produced by IMP in Figure 3(b) and (d) is a 3D thermal map of the diffraction pattern.	69
5.5 A simulation of the Fraunhofer diffraction pattern using Equation 3.....	71
5.6 The light ray trace of (a) a convex mirror (mesopyramid) and (b) a concave mirror (inverse mesopyramid).	72
6.1 Configuration of conductor and dielectric with defined axis.....	77

6.2 Dispersion curve of a Drude metal and air.	81
7.1 Scanning electron micrographs of (a) a mesopyramid and (b) inverse mesopyramid grown Si[100] wafer.	84
7.2 Experimental Setup.....	85
7.3 (a) An SEM micrograph of a MP and (b) the optical microscope image of the MP in (a) using white light and with oil immersion. (c) An SEM micrograph of a MP (d) the optical microscope image of the MP in (c) using white light and with oil immersion.	87
7.4 Reflectivity spectrum using a white light source of a single MP, where the arrows indicate SPP absorption bands at roughly 550nm and 650nm.	88
7.5 (a) An SEM of an inverse mesopyramid, (b) its corresponding atomic force microscopy profile, and (c) the line scan corresponding to the arrow in (b).	89
7.6 A schematic of the field of view of the microscope, where blue bands indicate areas within the field of view that SPP activity can be observed. The green triangles indicate the facets of the IMP that SPP behavior is observed. The red arrow indicates the direction of polarization of the light source.	91
7.7 (a) Reflectivity spectra of a denuded zone, an IMP, a Si wafer, an AuSi tri-layer, and an Au thin film, (b) difference curves between the denuded zone, the IMP, and an AuSi tri-layer and the reference Si wafer spectrum, (c) a difference curve of the difference curves between the IMP and the denuded zone.	92
7.8 SPP Absorption and Scattering	96
1.....	1

CHAPTER I

INTRODUCTION

The body of work in this dissertation is split into three areas of investigation. The first is an examination in the eutectic dynamics that produce meso-scaled pyramidal structures as a result of annealing Au or Au/Si/Au thin films supported on Si[100]. Why we refer to them as mesopyramids will become apparent. A eutectic is a material that has a lower melting point than that of its individual components. The second area is the far field optical properties of these structures. More specifically, the diffraction patterns they produce when light is reflected off their surface. The third and final area of research centers on the plasmonic characteristics of the mesopyramids.

Surface plasmons (SP) and surface plasmon polaritons (SPP) are nonlinear many-body excitations that couple light with the electron density of states of a material, in particular, metals[1]. The nonlinear nature of SP and SPP can be used for frequency doubling of light (second harmonic generation) [2] [3] and the formation of evanescent waves that enhance the Raman signature of molecules on a surface (Surface Enhanced Raman Spectroscopy), [4][5] to name a few. More recently, plasmonics are being utilized in metalenses, a two-dimensional lens that mitigates aberrations associated with traditional 3D lenses [6]. The future of metalens technology rests on the shoulders of the materials science community to develop new plasmonic

materials that have a broader suite of capabilities and superior nonlinear responses. The goal of my dissertation is tackle this challenge by exploiting the unique kinetics of the gold-silicon eutectic[7][8] to produce highly active gold silicide plasmonic mesostructures, i.e. mesopyramids.

Chapter 2 gives a brief explanation of the experimental techniques used to investigate the mesopyramids. This information is provided to give the reader context for the characterization methods chosen and basic details of operations for these systems. It also briefly touches on the considerations made with respect to our particular experimental setup. It is not provided to be an in-depth dive into the topics of microscopy. I refer the reader to the manufacturer, whose names and instrument models are provided, for further details about a specific analytical device used.

In this chapters 3 and 4, I report on my initial materials physics research on mesopyramid formation and our initial success in creating a repeatable process for producing them. I employed materials characterization techniques to build a framework of knowledge from which I could develop a complete theory of pyramid formation. Specifically, I used Scanning Election Microscopy (SEM) and Energy Dispersive Spectroscopy (EDS) to quantify the elemental composition of these structures. We refer to the structures as mesopyramids because they are mesoscopic polyhedron structures. These structures have been previously reported [9][10], therefore, we do not claim to be the first to observe them. However, in the previous studies, demonstrative proof of certain steps in the process of their formation was unavailable and relied instead on logical conjecture, modeling, or a combination of both to bridge the gaps. The results presented in this dissertation conclusively verify the hypotheses previously put forward. In addition, I report a previously unobserved surface morphology consisting of chevron like surface channels that only occurs when the Au pyramids has dimensions on the order of tens of microns. I also report for the first time the surface plasmon polariton spectrum of this novel meso-structures and their ability to produce polarized reflected light, which served to motivate the work presented in Chapters 5 and 7.

In this chapter 5 I present the results of far-field diffraction experiments performed with mesopyramids and the subsequent discovery of an inverse mesopyramids. Based on the results of these experiments, hypothesize that we can replace traditional bulky 3D lenses with near 2D metalenses constructed with our Au mesopyramids [11]–[15]. The development of 2D metalenses will significantly reduce the overall dimension of optical components, spectrometers, and optoelectronic devices to name a few. Gold is an essential material for the fabrication of metaoptics due to its surface plasmon polaritons properties [16]–[21]. For example, ordered perforations in a 30 nm thick Au film that are smaller than the diffraction limit of the light have been shown to focus and polarize the transmitted light [22]. Similar approaches have been used to construct metalenses that operate in the THz range [23]. Furthermore, with the appropriate surface texturing, one can manipulate the light line such that it crosses the nonlinear SPP dispersion curve, thereby exciting SPP over micron distances [24], [25].

In chapter 6 I present the theoretical background surface plasmon polaritons. I do this to give the reader context for the result that will be presented in chapter 7. I choose to format the flow of information in this manner as to no distract form the work proved in previous chapters. The derivation follows convention by addressing this phenomenon at a single dielectric conductor interface formed from two semi-infinite planar continuous surfaces[26]. This provides the reader a starting point from which we build on in our interpretation of results in the following chapter.

In chapter 7 I present my research on the excitation and scattering of surface plasmon polaritons on the surface of the Au mesopyramids. The results represent the current state of our knowledge, and therefore, are not presented as a definite or complete explanation of the SPP properties of the mesopyramids. There is still a great deal of work to be done. Consequently, the results in Chapter 6 are intended to be the foundation upon which we develop a robust model of SPP launching and scattering in microcavities. This work is important because SPP launching materials have been the focus of research endeavors at the forefront of optoelectronic device

development[27]–[31]. At the cutting edge of this research, the materials development community has been the driving force behind finding new applications for plasmon active metamaterials integrated into SPP centered optics. New geometries and material configurations broaden the possibilities for SPP technologies. The meso-scaled pyramidal configurations are striated with a stochastic distribution of cavities and plateaus, hereon referred to as a defect ensemble. The height differential for these structures is on the order of microns, while their bases are on the order of up to tens of microns. The topography of the MP and IMP is due to a phase separation that takes place of the binary eutectic of AuSi during pyramid growth. The subwavelength dimensions of these features make them prime candidates for SPP excitations and scattering. Due to the unique topography of our pyramidal structures, a stochastic distribution of defects is formed on the facets of the structure. These facets should be suitable for coupling multiple angles of incident light, i.e., continuity breaking at the surface at the mesopyramids that allow one to access a range of wave vectors. Using a simple optics experimental setup, I demonstrate that SPP are efficiently launched on the surface of the SPP and subsequent scattered back into visible light. Furthermore, I demonstrate that convex and concave mesopyramids allows us to control how SPP scattering into light. By taking advantage of the unique topography and course, grating-like texture of the MP and IMP, I demonstrate that with the right optics we can effectively couple photons to the plasma of electrons in the Au surface to launch SPP either down a facet of an IMP or within the cavities of the MP. Note that the physics is the same, it is simply the effect of the convex or concave geometry of the structures, which we can exploit in metalenses and metamirrors, per the results in Chapter 4. In closing, SPP metamaterials are playing an ever more significant role in the development of optoelectronic devices such as SPP Microcopy[32]–[34], near field optics[35]–[37], and nano-optics[38], to name a few.

In chapter 8 I concluded with a brief review of the entire body of work reiterating the most important knowledge gained in each chapter. I present this material following the same flow of

information in the body of the dissertation. I end with my recommendation for future research and address any unanswered questions.

CHAPTER II

EXPERIMENTAL METHODS

Section 1: Introduction

In this chapter I will discuss the experimental methods used to characterize a variety of properties of the MP and IMP. As was discussed earlier in the introduction in Chapter 1, this investigation was approached in a bifurcated fashion. One branch of research centered on the eutectic dynamics initially investigating the relative surface atomic composition of the mesopyramids with SEM and EDS. This provided a starting point to work from in terms of organizing an effective energetics model to explain pyramid formation. SEM/EDS of the bulk was also explored using a cross-sectional analysis and was made possible by creating a smooth surface after surface stabilization with a polymer rosin was applied to the substrates. The other branch of research was characterizing the optical properties of both pyramidal configurations. This was achieved with the use of enhanced signal detection by a photomultiplier tube as well as signal analysis with a Lock-in Amplifier. Spectroscopic data was also obtained using a tabletop microscope equipped with a variety of lenses such as: long working distance objective lenses and oil immersion lenses. These setups were specifically chosen to probe the efficiency of coupling of photons to the sea of electrons that exist on the surface of gold and propagates as a wave packet in the form of a surface plasmon polariton. We begin by examining the back scattered light from

surface plasmon polariton as well as local surface plasmons. I was able to characterize the transfer of energy that propagated through the body of these conduction electrons as a wave packet by analyzing the spectrum from the scattered SPPs.

Section 2: Scanning Electron Microscopy

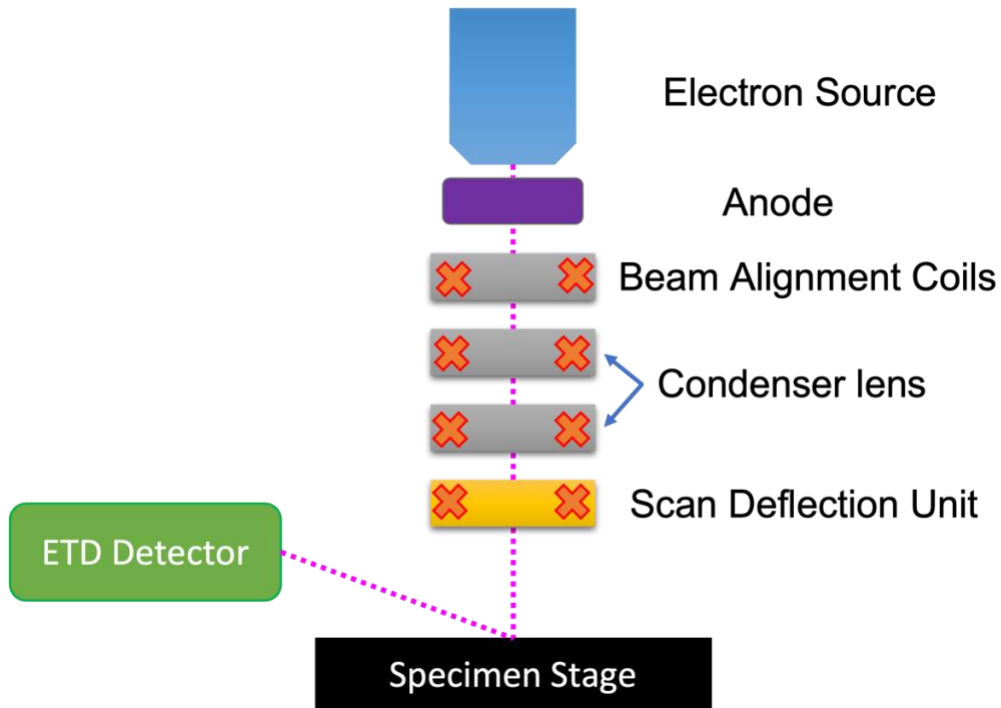


Figure 2.1 Schematic of scanning electron microscope.

Scanning Electron Microscopy was one of the primary methods of both surface and bulk characterization of mesopyramids. This was accomplished with an Everhart-Thornley Detector (ETD) on a FEI Quanta 600ESEM. ETD detectors are commonly used for scattered secondary electrons analysis [39]. The lower energy secondary electrons provided surface topography information used to characterize the mesopyramids. SEM components can be broken up into four general categories and brief description of these parts will be provided here. The SEM general components are as follows: the electron gun or source, lens assembly, scan unit and detector. See

Figure 2.1. For a more in-depth discussion of SEM, I refer the reader to the manufacture customer resources.

The electron gun, or source, is where the electrons are obtained that will interact with the surface of the sample in the imaging system. The SEM micrographs presented in this body of work were sourced from a cold cathode field emitter. The electrons are pulled from the tip of an electron source with the application of an electric field. They are subsequently accelerated toward the lens assembly with the use of two cathode anodes. The high resolution of this SEM is a result of the small diameter of the beam size due to the microscopic dimensions of the tip. The next component is the lens assembly. These lenses are electromagnetic coils that narrow the beam path of electrons emitted from the source tip. These condenser lenses can reduce the spot size from micrometers to nanometers [40], [41]. The beam deflection system rasters the beam in the field of view of the sample on the surface of the specimen stage. The stage brings the specimen within working distance of the last condenser lens. We can increase the working distance to obtain more depth of field but do this at a cost. With this increase of depth of field, resolution is sacrificed. There is a balance that must be made to see enough of the mesopyramid topography without losing the resolution of the nanometer dimensions of the cavities and plateaus. The detector is the final component of the SEM covered in this description. When the electron beam strikes the surface of the specimen that are two kinds of scattering that take place. Elastic scattering occurs when the electrons interact with the specimen without losing energy and only change direction; these are classified as back scattered electrons. The other kind of scattering interaction is secondary electrons; these electrons lose energy as they interact with the specimen. Secondary electrons were used primarily to obtain the micrographs presented in this body of work. The Everhart-Thornely Secondary Electron Detector gathers secondary electrons from the sample to form images. Positively charged components of the detector attract the lower energy electrons. With the use of PMT the image can be enhanced to show contrast between the light and dark

areas of the sample. This contrast is what gives the appearance of three dimensionality of the micrographs. Again, it should be noted that these are only the broad strokes of the components that make up the SEM system that was used to obtain data for this research. They are only provided to give context for which the study was performed.

SEM micrographs were obtained with an electron beam energy level between 5 and 20 kV. Changes were made to the energy level to prevent surface charging of the pyramid samples. Due to the conductive properties of gold, the samples were imaged uncoated. Another advantage of changing the beam intensity was to provide more contrast in the micrographs. This allowed for the pyramid's topography to be easily observed thus resulting in important conclusions while building a model of pyramid growth. Back scattered electrons were used with samples that the substrate was normal to the beam path. These high energy electrons were also used to probe the elemental configurations of different regions on the pyramids themselves. These regions, classified into two main categories are plateaus and channels. The subwavelength dimensions of this texturing were the primary motivation for the pyramid investigation.

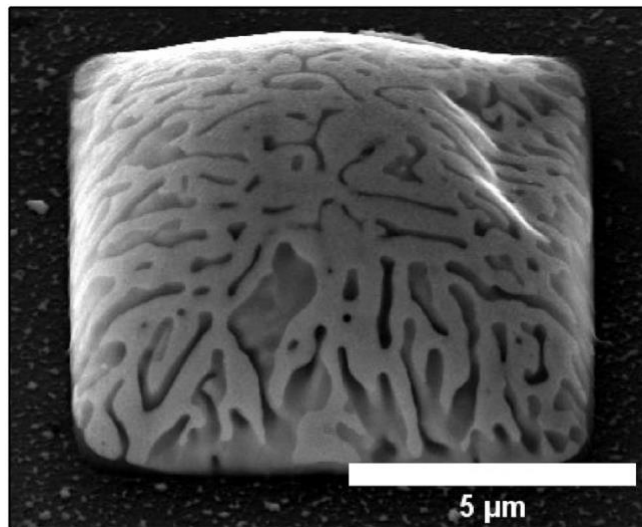


Figure 2.2 Mesopyramid Micrograph taken at 17 degrees with respect to the horizon with secondary electrons.

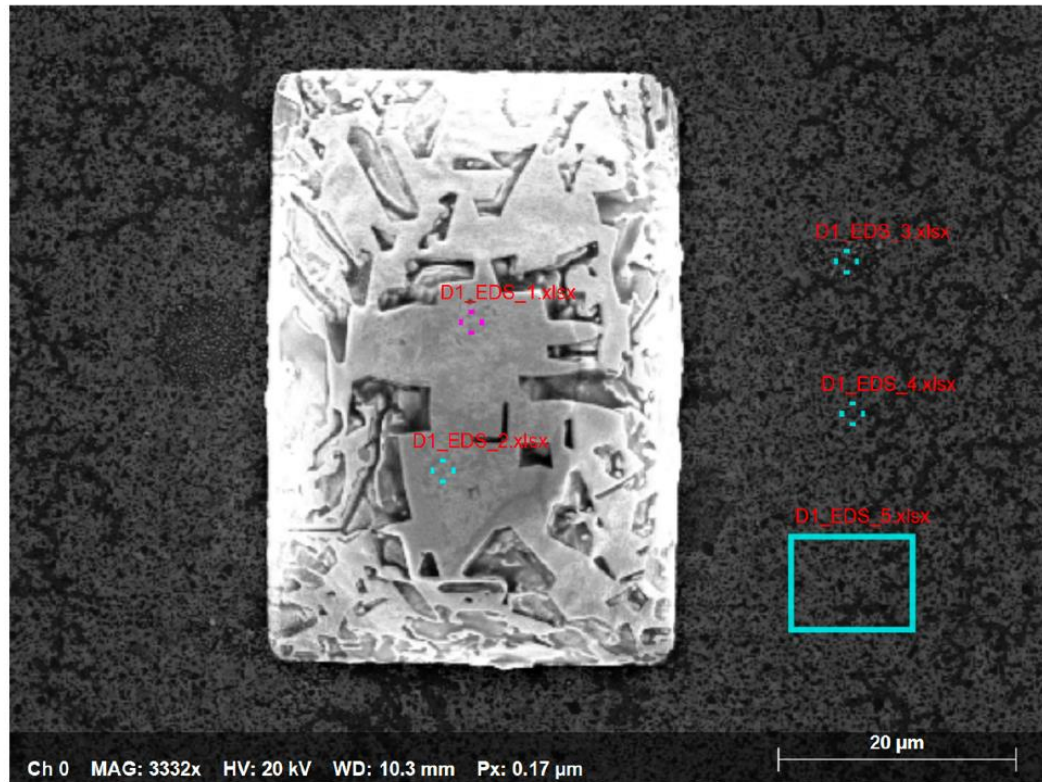
One of the advantages of our SEM setup was that it allowed for imaging to be done at angles offset from the horizontal. This provided a better understanding of the overall geometry of the structures. Samples that were imaged at an angle offset had to be imaged with lower energy secondary electrons to overcome alignment issues with the detector. This was done early in the investigation into pyramids formation and their geometry. Pyramids were imaged at an angle of 17 degrees with respect to the horizon to better illustrate the four-fold geometry. Axis of high symmetry can easily be seen and allow for a better understanding about the relationship between the base to height ratio. This was a very important consideration when designing optical experiments for reflected light. Small deviation in the angle of the surface when observed with long working distance objective must be accounted for during signal alignment. See Figure 2.2 for example of tilted mesopyramid. When collecting spectral data from the mesopyramids, the collection point had to be offset to account for this change in slope of the facets of the structure assuming the signal was normal to that surface. Any collection directly over the structure would result in a low or complete missed signal.

Section 3: Energy Dispersive Spectroscopy

Energy Dispersive Spectroscopy (EDS) was used extensively in the eutectic dynamics portion of this investigation. The SEM used is equipped with a Bruker Quanta Xflash SDD system. Probing the relative ratios of gold to silicon provided insight as to how the eutectic was responding to changes in the environment with parameters like temperature and vacuum. EDS is done by analyzing the x-rays produced by the beam-sample interaction[42]. The incident electrons create holes in the atom's inner electron shell and when an electron from the outer band drops down to fill this hole an x-ray is emitted to conserve energy. The energy of the x-ray is the difference from the outer and inner bands and is unique for all elements and can be used to identify the atom being probed. Intensity can be plotted as a function of energy level and a spectroscopic data plot is generated. Using the elemental library provided in the software with our

detector, we could select which elements we wanted to look for. This minimizes the occurrence of overlapping peaks thus mitigating false positives. A note about this type of analysis; the normalized atomic ratios provided are not to be interpreted as an exact number of atoms present at a given site under investigation. This tool is used to establish the relative ratio difference between two sites being probed on a single sample. The interaction volume of EDS is just that, a volume, not an infinitely small point. There is going to be some cross talk from the surrounding regions when taking data[43]. This is why the data presented was not a strict quantitative analysis, but more of a qualitative analysis. We wanted to demonstrate the average behavior from one region to another, i.e., cavities vs plateaus. For our samples, at the energy levels we probed at, the penetration depth of the beam was 30nm for gold and 10nm for silicon. This depth is much smaller than the overall height of the meso structures, which on average was between 5 and 7 microns. Keeping the probing depth shallow allowed for an analysis to be done without worrying that we were getting signal from the substrate itself.

EDS Report



Date	Time	HV [kV]	Mag	WD [mm]
9/12/2019	3:00:42 PM	20.0 keV	3332x	10.3 mm

Figure 2.3 Spot EDS Sample site of a mesopyramid

EDS Report

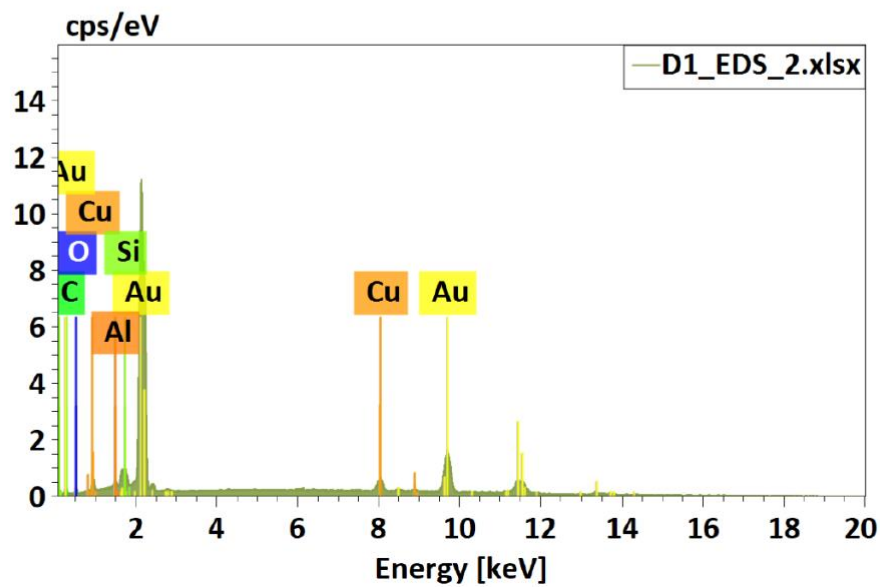
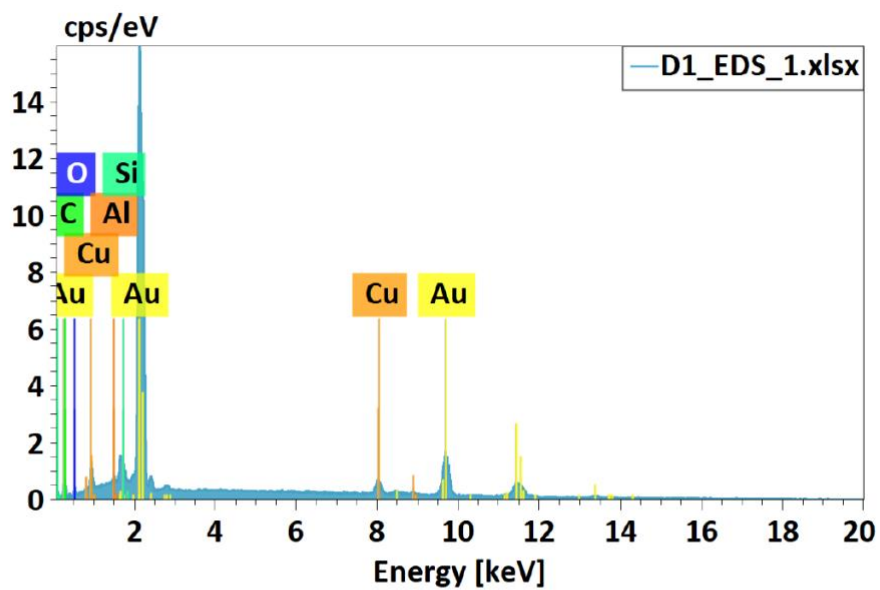


Figure 2.4 EDS Spot Data

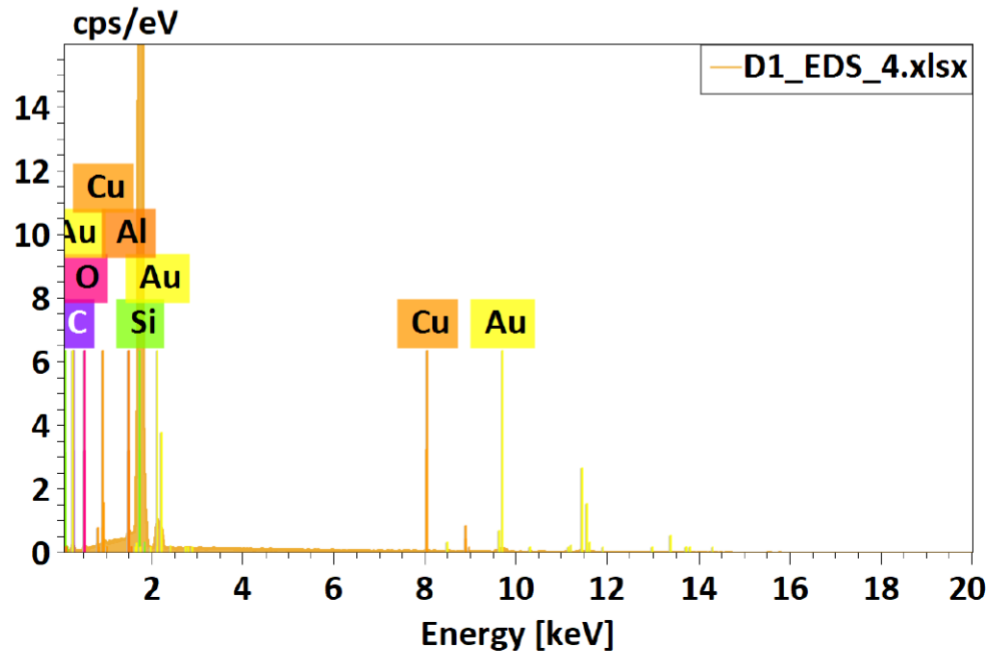
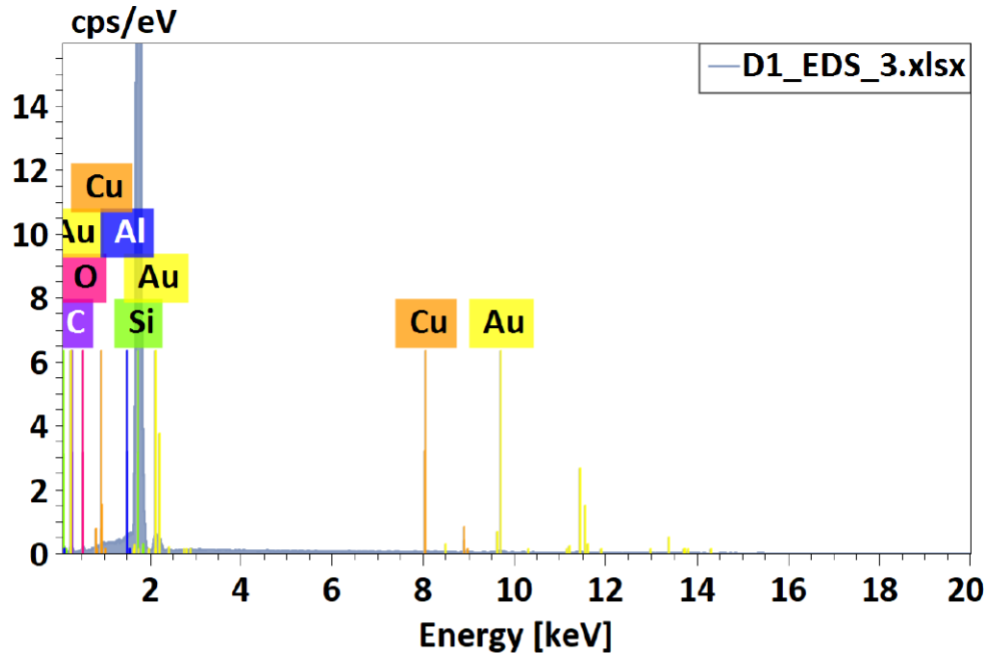


Figure 2.5 EDS Spot Data

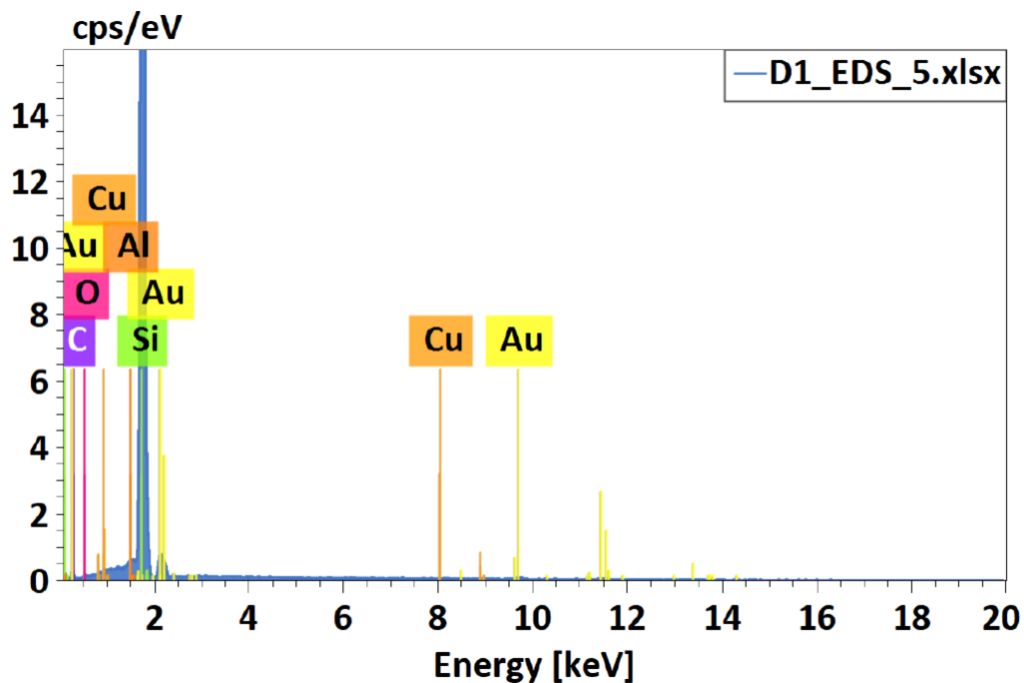


Figure 2.6 Data for corresponding EDS Spots on mesopyramid.

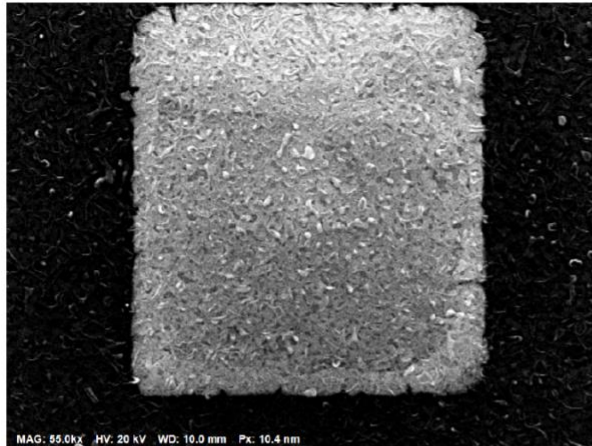
Normalized mass concentration [%]						
Spectrum	Carbon	Oxygen	Aluminium	Silicon	Copper	Gold
D1_EDS_1.xlsx	4.80	1.75	0.60	1.37	3.39	88.08
D1_EDS_2.xlsx	2.45	1.73	1.13	2.41	3.27	89.01
D1_EDS_3.xlsx	4.99	1.30	0.36	88.18	0.03	5.13
D1_EDS_4.xlsx	6.89	1.22	0.44	83.30	0.26	7.89
D1_EDS_5.xlsx	5.80	1.17	0.45	87.29	0.03	5.25
Mean	4.99	1.44	0.60	52.51	1.40	39.07
Sigma	1.64	0.28	0.31	46.25	1.77	45.18
SigmaMean	0.73	0.13	0.14	20.68	0.79	20.20

Table 2.1 Statistical data EDS spot sample sights.

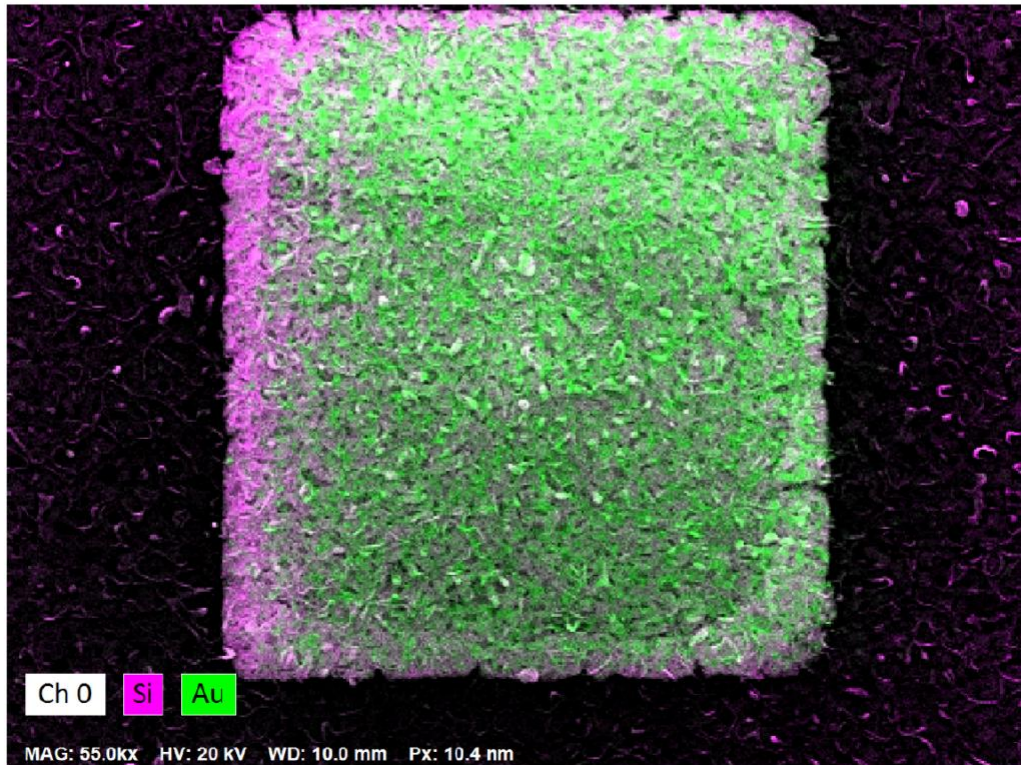
Two methods were used when taking EDS data to characterize pyramid growth. The first was spot EDS. This gave us the relative atomic ratios of silicon to gold at a given point keeping the volume as small as possible within the bound of the limitation of our experimental apparatus. This type of analysis was used during the surface characterization of the mesopyramids. See Figures 2.3 through 2.6 for an example of a complete Spot EDS report with corresponding SEM micrograph and spectra data as well a table of statistical data. See Table 2.1. This was one of the

first characterization studies performed to examine the ratio of silicon in the mesopyramid compared to the substrate. Note that fifth sample site was a large area that allowed for totals to be calculated within that given region. This function was applied to the entire area of a pyramid to contrast total surface pyramid composition to the substrate. This mapping feature shed light on the nature of the interphase of the pyramid and the substrate.

Report



Name	Date	Time	HV [kV]	Mag	WD [mm]
Ch 0	5/6/2020	2:16:27 PM	20.0 keV	55000x	10.0 mm



Date	Time	HV [kV]	Mag	WD [mm]
5/6/2020	2:16:27 PM	20.0 keV	55000x	10.0 mm

Figure 2.7 Elemental Area Map of a mesopyramid.

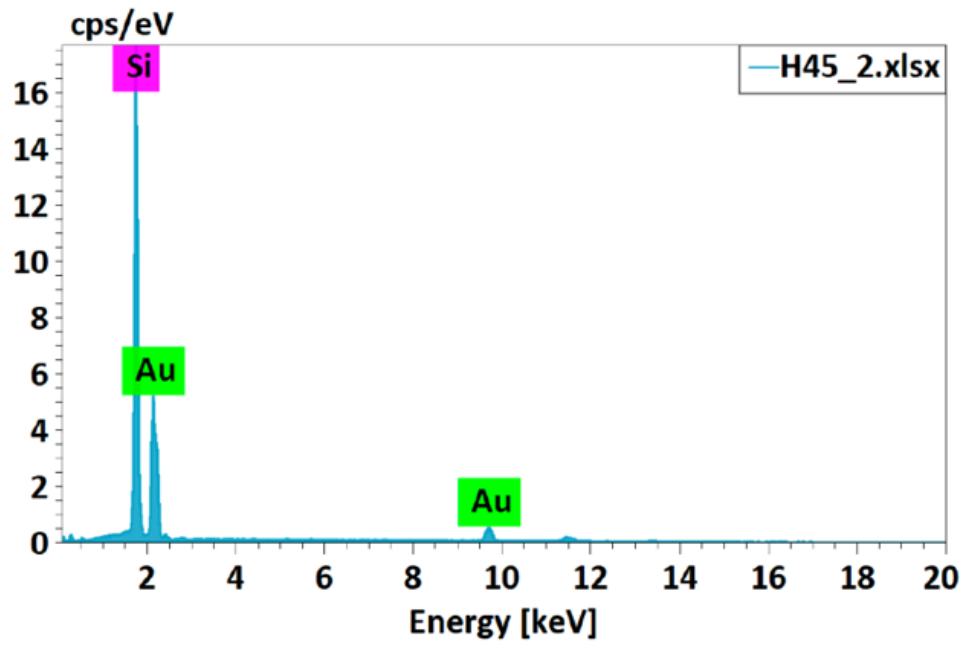
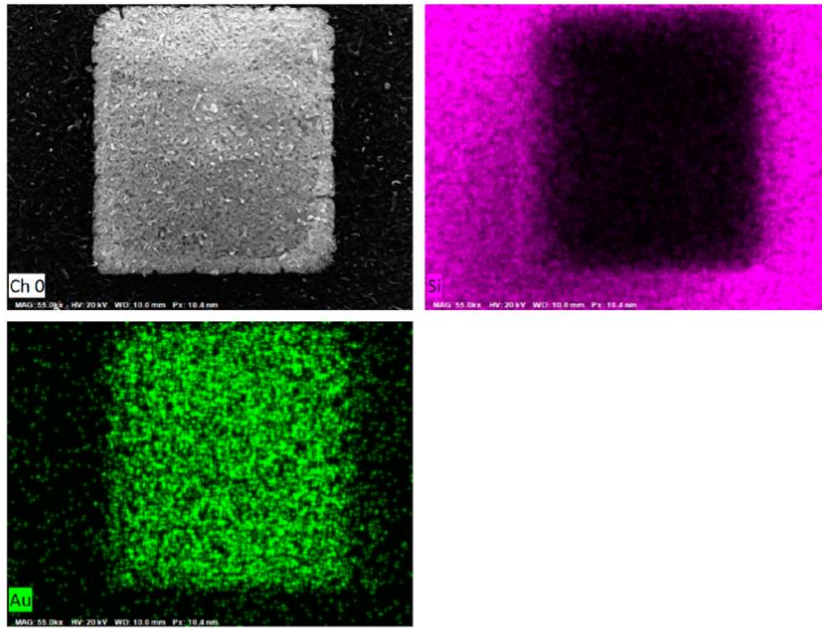


Figure 2.8 EDS split channel maps and corresponding data.

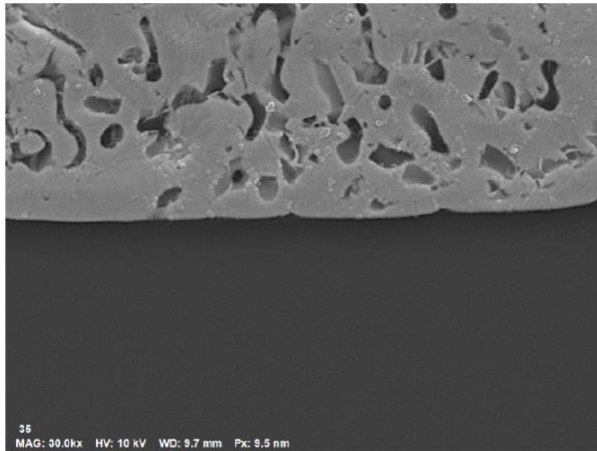
H45_2.xlsx

Element	At. No.	Mass [%]	Mass Norm. [%]	Atom [%]
Silicon	14	43.64	45.67	85.50
Gold	79	51.92	54.33	14.50
		95.56	100.00	100.00

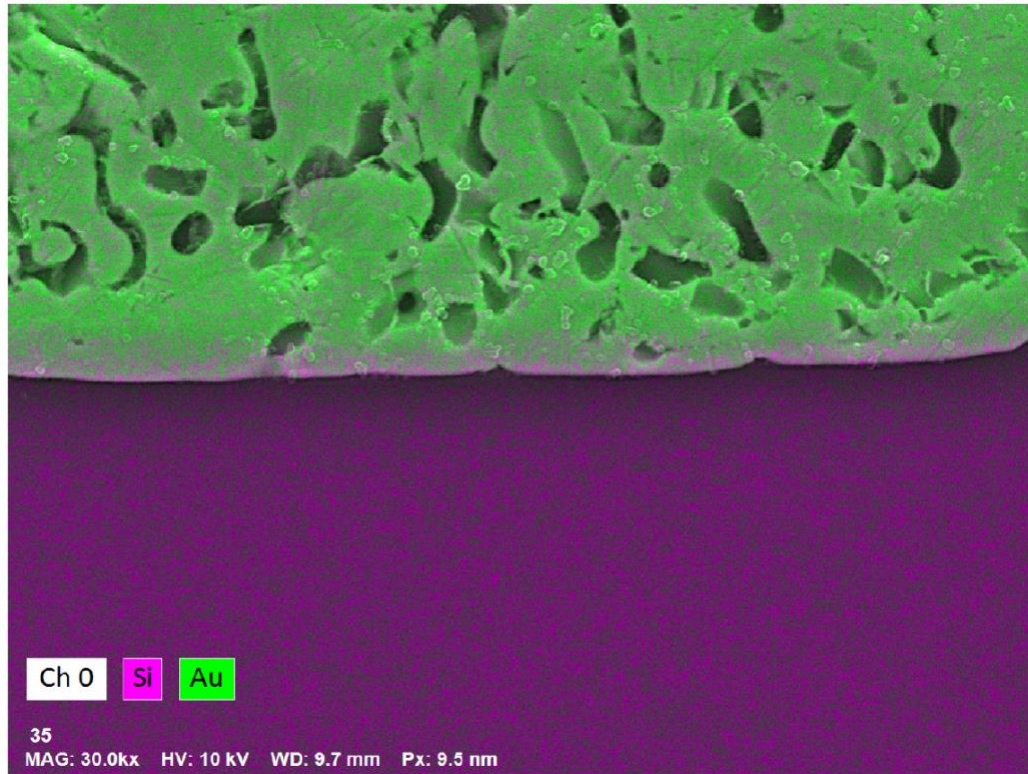
Table 2.2 Statical Data of EDS map.

Data from Figure 2.7 and 2.8 shows how the sides of the mesopyramid articulate with the surface of the substrate in an elemental map. Also provided are the corresponding elemental ratios as well as a table of statistical data. See Table 2.2. This understanding was vital when constructing an energetics-based argument for pyramid formation. The use of the binary phase diagram of AuSi [44] allowed for analysis of the elemental configuration to be compared to that of the phase diagram. The phase lines plotted on a graph change as a function of temperature and relative atomic ratio of Si to Au. This information is explained in detail in chapter 4. To gain a better understanding of the bulk properties of the meso structures a cross-section was created to examine the bulk properties of the MP and IMP. As was discussed in chapter 2, surface stabilization was accomplished with a polymer rosin that stabilizes the structures. This was needed due to the delicate nature of the structure. Sample prepared with a precision polisher created a biface that allowed of two facets of a sample to be prepared at one time. This was done to double the chances of getting a good pyramid to image. The samples were then mounted uncoated and imaged and would be then analyzed with map and line scan EDS.

H59_map



Name	Date	Time	HV [kV]	Mag	WD [mm]
Ch 0	6/4/2020	1:57:21 PM	10.0 keV	30000x	9.7 mm



Name	Date	Time	HV [kV]	Mag	WD [mm]
35	6/4/2020	1:57:22 PM	10.0 keV	30000x	9.7 mm

Figure 2.9 EDS Area map of interface of a mesopyramid and substrate.

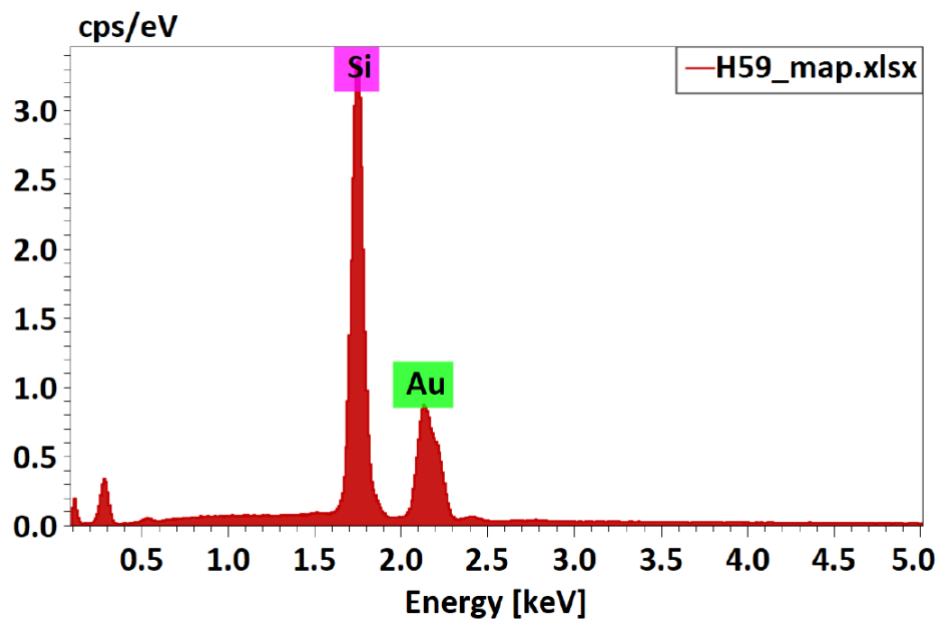
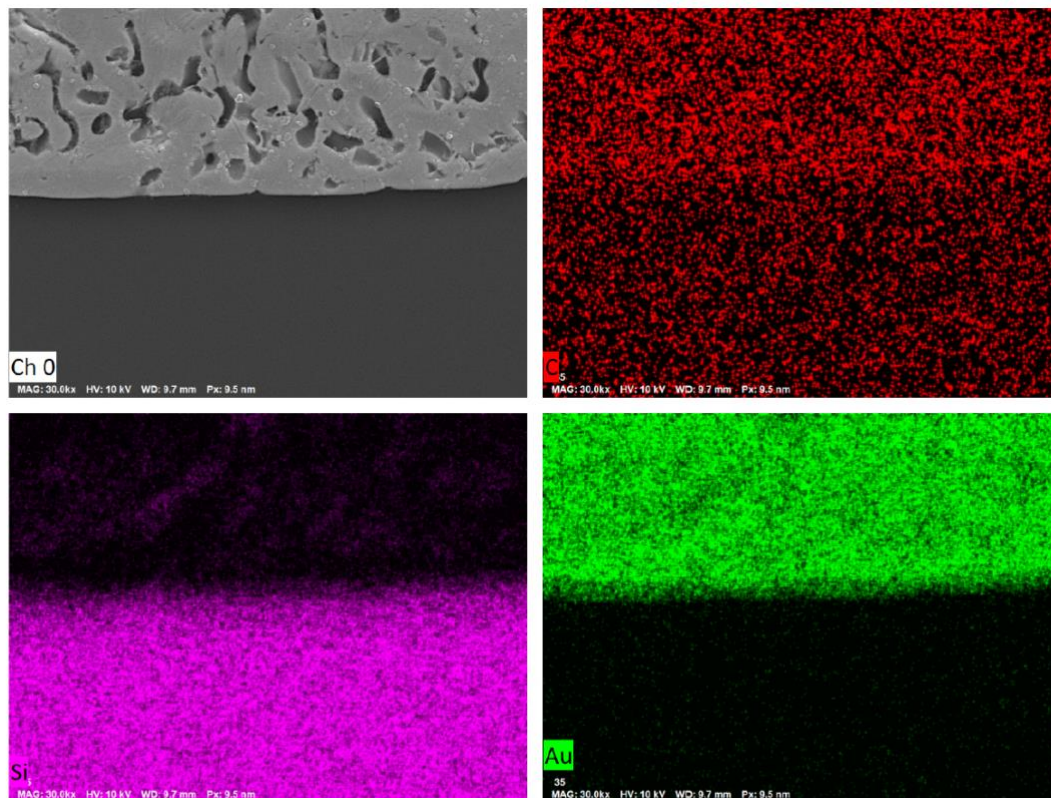


Figure 2.10 Split channel of area EDS map along with corresponding spectroscopic data.

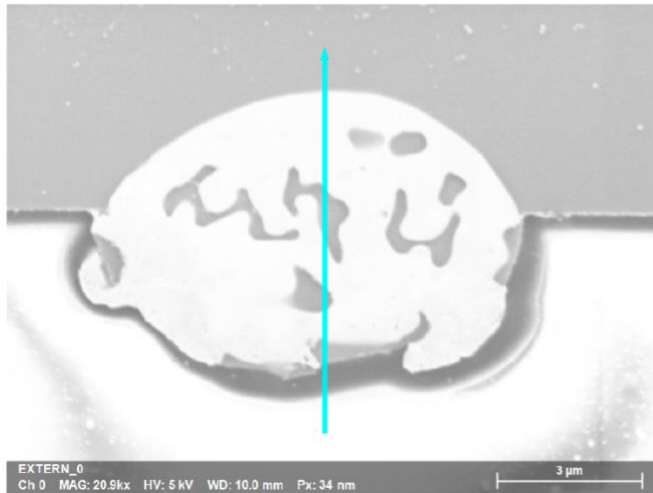
H59_map.xlsx

Element	At. No.	Mass [%]	Mass Norm. [%]	Atom [%]
Silicon	14	62.49	53.49	88.97
Gold	79	54.33	46.51	11.03
		116.82	100.00	100.00

Table 2.3 Statistical Data of mesopyramid substrate interface.

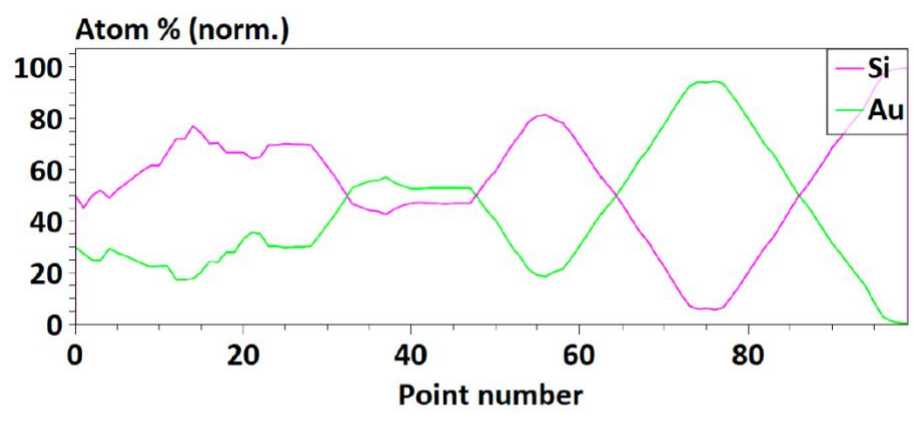
Area mapping was performed on these cross sectioned samples as can be seen in the reposts, Figures 2.9-2.10. These samples provided important data sets that demonstrate the way that these pyramids interact with the substrate. See Table 2.3 for statistical data on elemental ratios. This information led to one of the main conclusions from chapter 4, that the substrate was an active participant in mesopyramid formation. The contrast in color demonstrated to what level the phase separation occurs in the final stage of MP and IMP formation. We can again split the channels and then do single overlay allowed for us to gain good insight into what the boundaries looked like between the structure and the substrate. This information played an important role in the development of the eutectic dynamics argument.

Report



EXTERN_0
Ch 0 MAG: 20.9kx HV: 5 kV WD: 10.0 mm Px: 34 nm 3 μm

Name	Date	Time	HV [kV]	Mag	WD [mm]
EXTERN_0	12/11/2020	2:08:29 PM	5.0 keV	20945x	10.0 mm



Name	Date	Time	Points	Length [mm]
10	12/11/2020	4:19:22 PM	100	8.0 μm

Figure 2.11 EDS line scan report of a mesopyramid.

The decision to move from a spot analysis to that of a line scan was because it would provide a way to calculate the ratios of gold to silicon in the bulk of the structure. This would give an overall picture of the atomic ratio of the entire pyramid that was probed as a function of maximum annealing temperature. A line starting at the bottom of the pyramid drawn to the top will pass through the bulk and the cavities of the structure. Choosing a line keeps biases from being introduced into the data by drawing it through the middle of three randomly chosen pyramids for a specific growth cycle. An example of one of these line scanned pyramids can be seen in Figure 2.11. This is a pyramid on the top of a biface section. In the orientation presented in the report, the substrate is on top, and the polymer section is on the bottom. The data can be truncated to ensure that signal from the substrate or casting polymer was excluded from the ratio calculation. This ensured that we were not getting signal from the substrate giving a higher percentage of silicon in the data with respect to gold. This cross-sectional data was plotted against the binary eutectic phase diagram and was the central argument that we made in chapter 4. This data coupled with a computational model was how we explained mesopyramid formation from start to finish.

Section 4: Atomic Force Microscopy

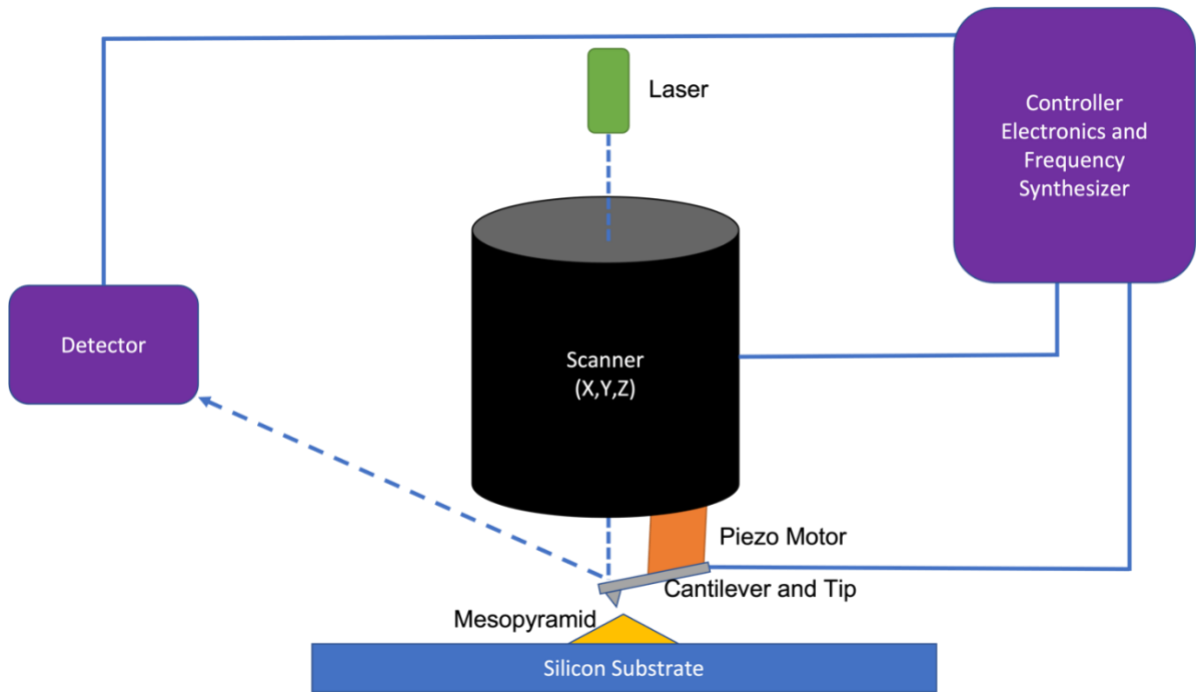


Figure 2.12 Basic schematic of AFM system.

Atomic Force Microscopy (AFM) was used to characterize the geometry of the meso-structures. Our system is an Oxford Asylum MFP3D Atomic Force Microscope. This was a critical method of characterization in that when viewing the structures spectrally, due to their facets, it was easy to assume that all the structures were super-surface. The presence of axis of high symmetry created an illusion that all the pyramidal structures were above the surface of the substrate. However, this wasn't the case. It wasn't until we were deep into the investigation of the diffraction patterns, that it was discovered that there were in fact two types of pyramidal geometry, the mesopyramid and the inverse mesopyramid. In inverse mesopyramids the axis of symmetry is still preserved. When observed spectrally, it is almost identical to that of a mesopyramid. These differences were confirmed with AFM analysis. Due to the delicate nature of the meso structures, no direct mechanical contact can probe the surface without damaging the structures. AMF tapping mode was chosen to do this topography analysis. Tapping mode, although the name is a little

deceptive, drives a silicon AFM tip slightly above the resonance frequency closet to the structure but does not actually make physical contact. This tip is referred to the cantilever. The type of cantilever that used was a AC160TS-R3 and had a diameter of 7nm at the tip. Due to the interaction of the Van Der Waals forces between the tip and the sample and the close distances, the tip oscillation change near the surface creating feedback loop to move the time up to return the tip to near resonance oscillation [43], [45]–[48]. This movement provides topological data from the surface of the sample. Ensuring that the system moves slow enough to keep the tip from disassociating with the surface of the substrate was one of the challenges of the method of investigation. Most scan windows for AFM data sets were around 60 microns squared. The window needed to capture the entire structure as well as enough substrate to be able to perform a good analysis of the height differential between the MP or IMP and the substrate. This as a particularly challenging aspect of this method of investigation. The system has no automatic approach to bring the tip to within the working distance of surface. See figure 2.12 for the basic components of the system. Due to the angle of the camera, as the tip made its approach the target structure it would move out from under the tip and would require realignment.

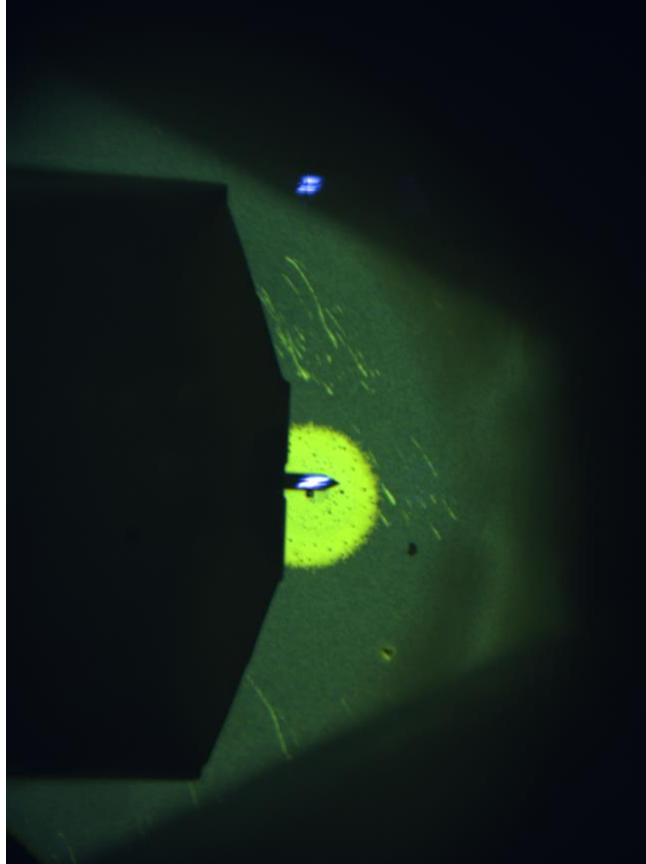


Figure 2.13 AFM scanning a denuded zone with a mesopyramid centered.

One of the advantages of the experimental results is that pyramids are grown at the center of easily identifiable denuded zones (DZ). See Figure 2.13. Central to these zones are a large pyramidal structure where the mesopyramid had nucleated. The volume of the thin film that makes up the DZ has gone into the central MP or IMP. The contrast of the remaining thin film and DZ was easy to identify under the camera of the AFM. Making ink marks of the surface of the substrates allowed for the identification of a particular mesostructures and their corresponding DZs thus allowing me to get an exact topological survey and couple it to the optical properties I investigated in both diffraction and surface plasmon polariton experiments.

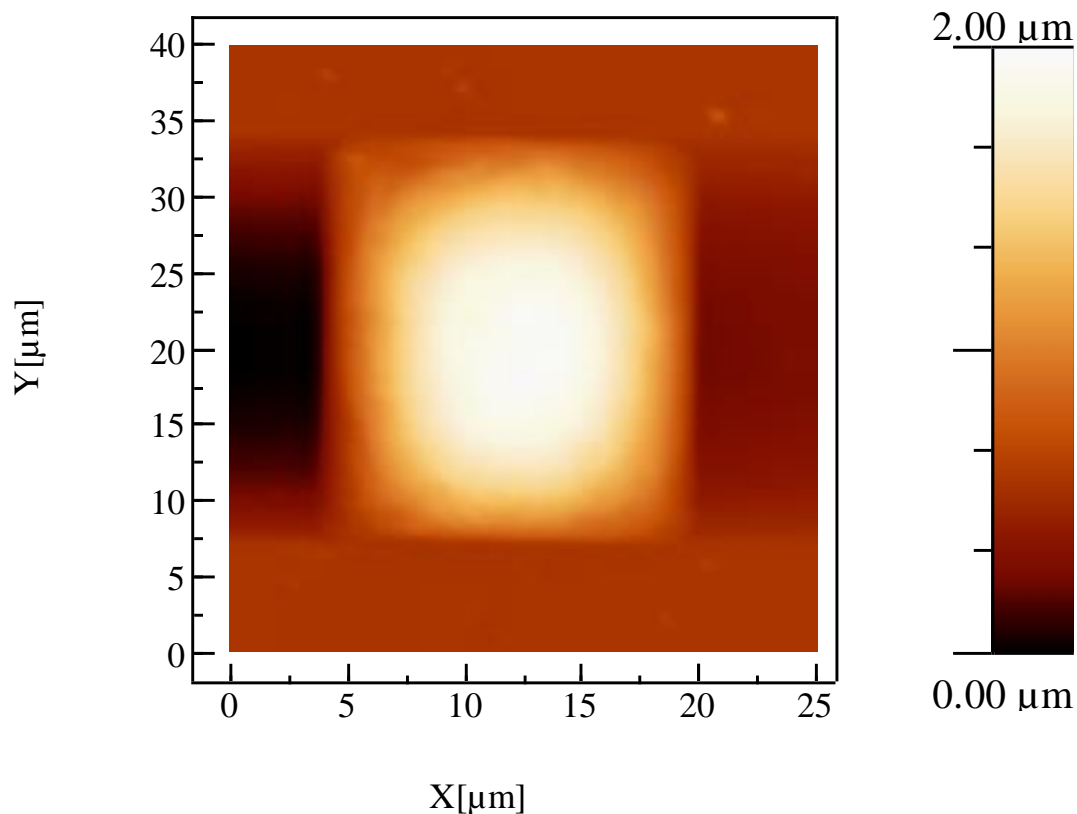


Figure 2.14 AFM data for a single mesopyramid.

Due to the height of the structures, there was an artifact created by the rapid change in frequency of oscillation of the tip once it cleared the structure as can be seen as dark regions to the left of the mesopyramid in Figure 2.14. The tip momentarily oscillates beyond the near resonance frequency and takes time to settle. This gives the appearance of a deep trough in the line of motion of the tip as it moves back and forth. To overcome this artifact, the analysis was always taken perpendicular to the line of the motion of the tip. This was presented as a scan line on all data presented in this body of work. The height differential taken perpendicular to travel path of the tip illustrated the base to height ratio of the mesostructures with respect to the substrate. This data was critical when modeling the structures as spherical mirrors. Being able to calculate

the radius of curvature facilitated in the formation of a model that characterized light incident on a square aperture.

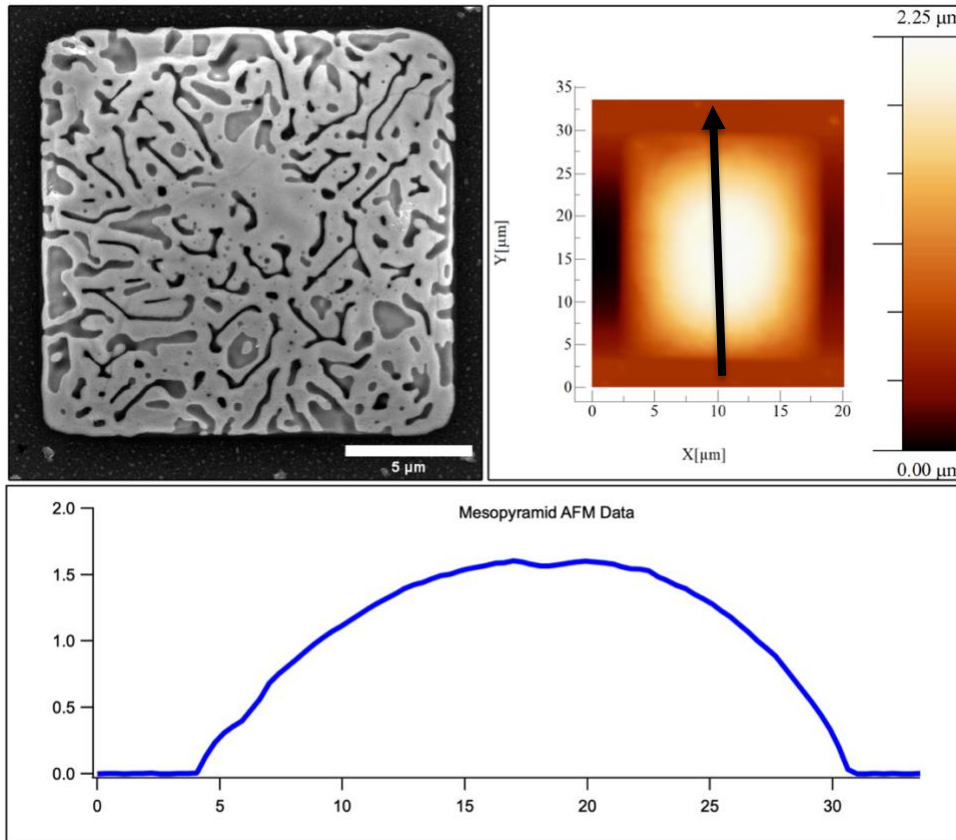


Figure 2.15 SEM/AFM Data set for a single mesopyramid.

The AMF data presented in this body of work followed the format as can be seen in Figure 2.15. A note about the graph provided, the scale in the x axis is not the same as that of the y axis. This can give the impression that the structure has an exaggerated pyramidal geometry, when in reality the 4 facets, when viewed spectrally, have a very gradual incline. This data became critical when calculating the focal points of diffraction patterns generated by these structures when modeled as an elliptical mirror.

Section 5: Magnetron Sputtering Thin Film Deposition

Pyramid growth consist of three deposited thin films on the surface of the substrate. These films are deposited through a physical deposition process (PVD). Amorphous Au and Si are applied to the surface of the RCA cleaned substrates via magnetron sputtering. This deposition is done at room temperature. Sputtering a tri layer of thin films allowed for a nearly uniform thickness of film to be grown. This was very important due to the fact that the eutectic melting point is dictated by the ratio of silicon to gold on the surface of Si[100] as will be discussed in more detail in chapters 3 and 4. Changing the thickness of gold and silicon films allowed for the optimization of this ratio to be achieved, thus obtaining the lowest phase transition temperature possible for the AuSi eutectic. Our experimental setup for thin film deposition is a custom designed UHV chamber with a mechanical arm that allowed us to move the wafer between to the two-sputter head without having to vent the system. This feature came into play in an important way since the silicon thin film would start to oxidize when exposed to air when moving the sample between sputter heads before the mechanical arm upgrade. This is what lead to a gold capping layer being used to minimize this silicon oxidation.

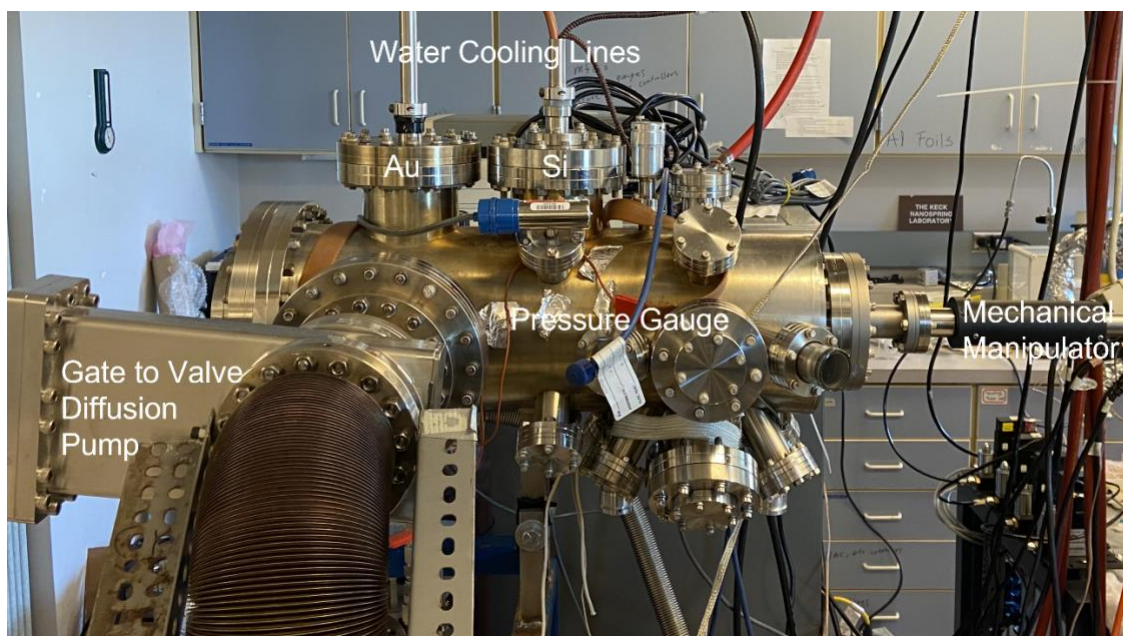


Figure 2.16 Magnetron sputter system basic components.

A single large multiport UHV chamber houses 2 sputter heads. The vacuum system is a mechanical rotary pump as well as second mechanical rotary rough pump paired with a diffusion pump. Films are deposited at roughly 10 mTorr of pressure maintained by a leak valve controlling the flow of Argon gas. The primary components of the system can be seen in Figure 2.16. A gate valve closes off system from the diffusion pump during the rough pumping of the system to get it to high enough vacuum. The films are deposited at room temperature and observe no long-range ordering. This is an important factor in keeping the activation energy low for pyramid growth, exploiting the phase change of the thin film from a solid to a liquid to create the eutectic.

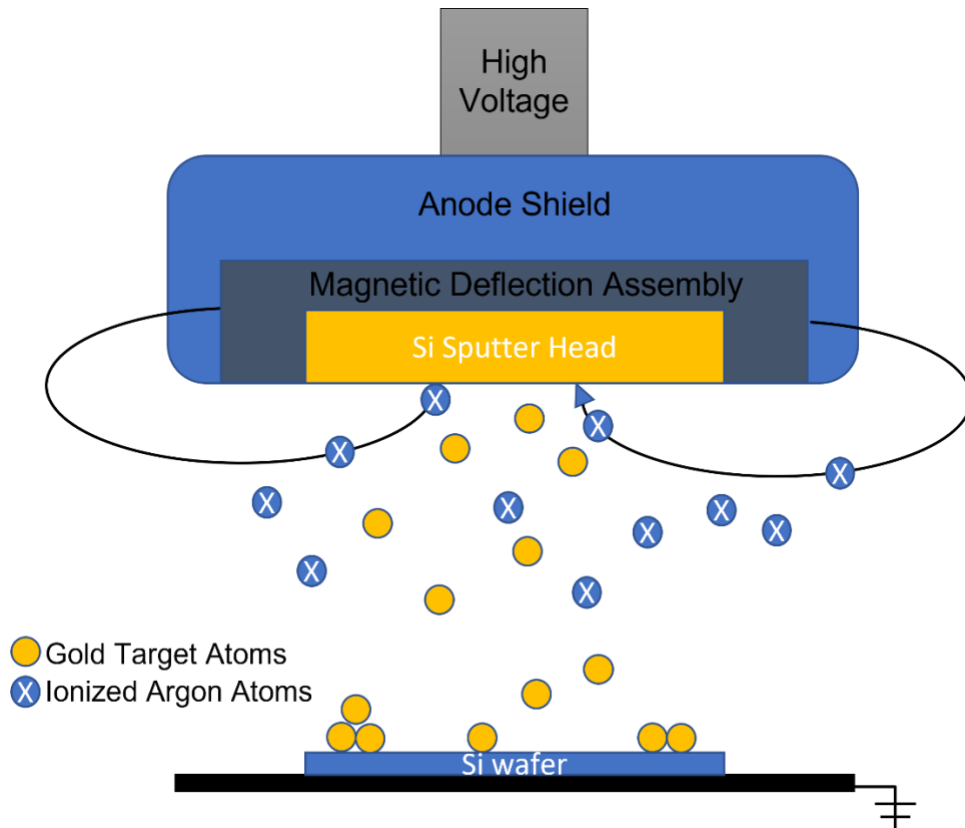


Figure 2.17 Magnetron sputter head setup.

Argon is used to generate a plasma for sputtering. With the application of a strong electric field the ionized atoms are propelled to the sputter target, Au or Si, and material is physically dislodged. This material begins to deposit on the surface and forms the thin film. See Figure 2.17 for a schematic graphic of the deposition process. The rates of deposition were calibrated with the use of a masked sample analyzed with a profilometer. This process was repeated a second time with AFM to ensure the results were consistent.

CHAPTER III

EXPLOITING EUTECTIC FORMATION AND PHASE SEPERATION TO PRODUCE PLASMONIC METAMATERIALS

Section 1: Introduction

In this chapter I report on our initial success in creating a repeatable process to produce mesopyramids. A surface characterization was performed to begin to build a framework from which we could explain pyramid formation. This was accomplished with the use of Scanning Election Microscopy (SEM) and Energy Dispersive Spectroscopy (EDS) to quantify the elemental configuration of the structures. This topic will be further expanded to the bulk properties of the MP and is the focus of Chapter 4. Spectral data was also obtained to probe the basic plasmonic properties of the pyramids as well as examine the nature of the light reflected i.e. the polarization.

Section 2: Methods

Samples were prepared by DC sputtering a 25 nm thick Au film onto an RCA cleaned Si(100) substrates with a native oxide. Samples were annealed in a custom-built vacuum chamber that has a base pressure of 50 mTorr. The system was back filled with air to a pressure of 150 ± 5 mTorr, at which time the sample temperature was ramped up at a rate of ~ 23 °C/minute until it reached its maximum temperature of 700°C, where it soaked for 30 minutes. At the end of the soaking cycle the heater was turned off and the sample allowed to cool to room temperature, where the

cooling rate to 300 °C was approximately 20 °C/minute, where 300 °C is below the Au-Si eutectic melting point. The chamber pressure was maintained at 150 mTorr during the cool down phase of growth.

Section 3: Results

This process produces well-defined circular delineated zones with diameters in the range of 500-1000 μm . Similar behavior has been observed for Au films on Si.[9], [49] Scanning electron microscopy (SEM) micrographs of these zones reveal the formation of mesoscopic polyhedron Au structures[50], which are referred to as meso-pyramids or simply pyramids. The SEM micrograph in Figure 3.1(a) is of one such delineation zone consisting of a large pyramid (20 μm x 25 μm) surrounded by a distribution of many smaller pyramids, typically <10 μm on a side. We believe that this is the first observation of pyramids of this size. Note that all of the pyramids in Figure 3.1(a) are aligned in the same direction, specifically, parallel to the [001] and [010] directions of the Si(100) surface, which has been previously reported.[7], [50]–[52] Furthermore, a delineation zone may contain a single pyramid or many, as in the case of Figure 3.1(a). Displayed in Figure 3.1(b) is a high-resolution SEM micrograph of a large Au pyramid (23.6 μm x 26.3 μm) that clearly reveals its unique surface morphology. The surface of the pyramid in Figure 3.1(b) consists of many long surface channels on the order of 1 μm in width and as long as 10 μm . The surface channels radiate on average outward from the center to the perimeter of the pyramid. This type of surface morphology is only observed for taller pyramids with heights on the order of tens of microns. Au pyramids that have a height less than approximately 5 μm have cavities, as opposed to surface channels. Both morphologies are a consequence of diffusion of Si and will be addressed shortly.

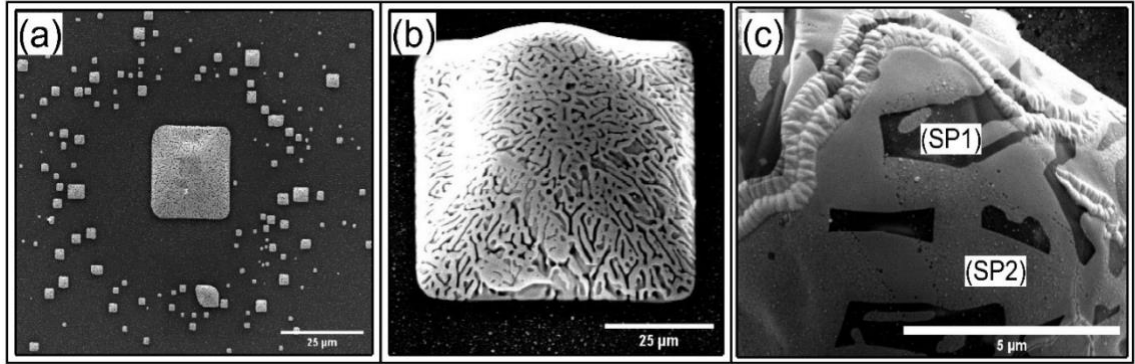


Figure 3.1 (a) A SEM image of a large Au pyramid surrounded by a cluster of smaller Au pyramids, (b) a SEM image of a single Au pyramid, where the surface texturing is resolved, and (c) a high-resolution SEM image of an Au pyramid that was quickly quenched, where SP1 is a region where Si remained in what are usually cavities and SP2 is the typical Au rich region of the pyramid.

Section 4: Discussion

Surface texturing of Au structures supported on Si have been attributed to the formation of an Au-Si eutectic phase and subsequent phase separation of Au and Si.[53] [54] [55] [56] Furthermore, Lindner et al. [57] observed similar texturing of the Au catalyst on the tip of a Si nanowire, where in this case the Au-Si eutectic[44] provides the Si for the Si nanowire forming below. Their results suggest that the texturing of the Au surfaces[58] in their studies correspond to cavities, similar to our findings. However, this is indirect evidence. In an effort to conclusively verify that the cavities in the Au pyramid in Figure 3.1(b) are due to phase separation of the Au-Si eutectic and subsequent diffusion of Si out of the pyramid[59], pyramid formation was aborted by turning off the sample heater prior to reaching the maximum temperature of 700 °C. Typically, this involved turning off the sample heater once it reached 400 °C. Consequently, these experimental runs excluded any soaking of the sample, where soaking is defined as the amount of time that the system was held at the target temperature. An SEM micrograph of a representative

example of a partially formed Au pyramid is presented in Figure 3.1(c). The surface is solid but with light and dark contrasting regions, as opposed to cavities like in Figure 3.1(b). The contrast arises from differences in electron scattering associated with the different Z numbers of Au and Si. Energy dispersive spectroscopy (EDS) was performed on a dark (SP1) and light (SP2) region of the pyramid of Figure 3.1(c) to obtain the relative ratios of gold to silicon. The EDS of SP1 in Figure 3.1(c) indicates a composition of 95.4% Si and 4.6% Au, while the EDS of SP2 indicates a composition of 6.4% Si and 93.6% Au. Note that EDS analysis of pyramids similar to that in Figure 3.1(b) had the following composition: cavities - 85.7% Au and 14.3% Si and intact regions - 98.1% Au and 1.9% Si, where the higher Si content of the cavities is consistent with them previously being filled with Si. The conclusion is that the cavities in the Au pyramids are the result of phase separation of the eutectic where the formation of Si rich regions are precursors to the cavities that form when Si vertically diffuses from the pyramid to the Si substrate. The shape of the Si rich regions in the in Fig. 1c are exactly the same as the morphology of the Au catalysts at the tips of Si nanowires reported by Lindner, et al.[57] and supports our conclusions that phase separation of the eutectic occurs, followed by diffusion to the Si substrate. In Lindner's case, to the underlying Si nanowire. The rippled tracks on the surface of the pyramid in Figure 3.1(c) are an interesting artifact of aborted pyramid formation, but presently beyond the scope of this work.

The surface morphology of the pyramid in Fig. 1(b) is typical of pyramids with heights > 5 μm . For these taller pyramids, randomly aligned voids are replaced by interconnected surface channels that have an average alignment relative to the symmetry plane of a face of the pyramid that is defined as the line connecting the middle of the base of the face to the apex of the pyramid. Channels to the left of the symmetry plane have an average clockwise rotation of 30° and those to the right have an average counterclockwise rotation of 30° . Note that the surface channels produce Au plateaus on the surface with the same orientation. The effects of the orientation of these plateaus on the optical properties of the pyramids will be discussed shortly. We believe that

the diffusion of Si out of the taller pyramids is a combination of Si diffusion in the interior vertically back into the substrate and Si diffusion parallel to the surface of the pyramids either towards the edges and back into the substrate or to cavities that vertically extend to the bottom of the pyramid.

Cross sectional SEM of the Au pyramids was performed to better understand the formation of the Au-Si eutectic, as well as the subsequent formation of the Au pyramids and their alignment with the Si substrate. The samples were cast in resin, cut, and polished. A cross sectional SEM image of a pyramid is displayed in Figure 3.2(a). Note that >50% of the volume of the pyramid is subsurface. This indicates that Si is scavenged from the substrate and that the mechanism of their formation is surface diffusion of Au [60] [61] concomitant with dissolving of and incorporation of Si into the Au-Si eutectic [62]. Figure 3.2(b) is a high-resolution EDS map of the pyramid/Si interface, where green corresponds to Au and purple to Si. The pyramid is predominantly comprised of Au with small quantities of Si, consistent with the analysis in Figure 3.1. More importantly, a 200 nm boundary layer with a rapidly increasing concentration of Si exists at the pyramid/Si interface, which is consistent with Si reincorporation into the Si substrate, i.e. the final phase of pyramid formation.

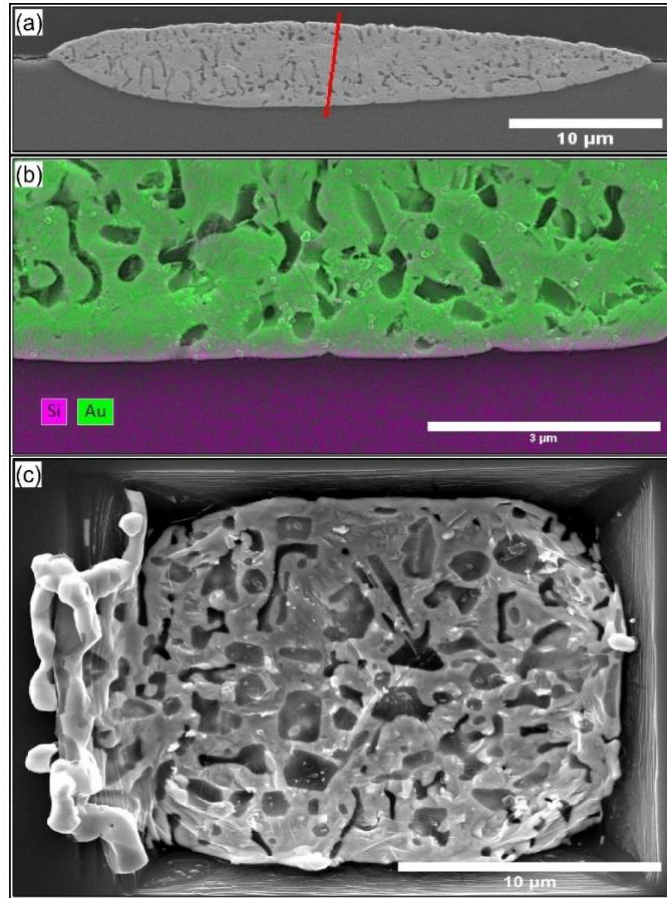


Figure 3.2 (a) Cross sectional SEM image of an Au pyramid, (b) an EDS map of Au pyramid-Si substrate interface, and (c) a SEM image of a partially formed pyramid that shows the etching of the Si(100) substrate caused by the formation of the Au-Si eutectic.

The question of the indexing of the pyramids to the Si(100) lattice is intriguing and to date, an open question. Specifically, does indexing occur during the formation of the eutectic or as Si is driven from the Au pyramid? To definitively answer this question, we performed experiments using Au layers with thicknesses less than 20 nm, where thin Au layers allow us to image the foundation upon which the pyramids form. Displayed in Figure 3.2(c) is a SEM image of an early stages of pyramid formation. It is apparent that the Au-Si eutectic forms by scavenging Si from the substrate preferentially in the $[00\bar{1}]$ direction, which produces a rectangular trough with walls in the $[100]$ ($[\bar{1}00]$) and $[010]$ ($[0\bar{1}0]$) directions. It can therefore be concluded that the indexing

of the Au pyramids occurs at the initial phase of their formation and is a consequence of preferential etching in the $[00\bar{1}]$ and the formation of a rectangular profile, which obviously corresponds to the minimum free energy configuration of the system[63]. These locations serve as nucleation points for the pyramids, where Matthews et al.[49] have developed a diffusion model for this system that takes into account the flux associated with Au-Si alloying[64][65][66].

The unique polyhedron shape and surface topology of these pyramids makes them a well-suited material for research into surface plasmon polaritons (SPP), where SPP optoelectronic devices are being of great interest to the scientific and engineering communities. For instance, a subwavelength nanodevice takes advantage of dual nature of SPP having a photonic component as well as an electronic component that allow them to be focused in volumes below the diffraction limit [67]. The naturally occurring surface channels (plateaus) on the surface of the pyramids created by Si diffusion to the substrate should be ideal structures for launching SPPs. Note that lithographic formation of polyhedron structures are already being explored for use as metalenses. Our ability to produce this unique texturing using thin films and annealing processes greatly reduces the cost and waste in metalenses fabrication. Scattering spectra (non-specular reflection) of an Au pyramid, similar to the one in Figure 3.1(b) is displayed in Figure 3.3(a), that was acquired using an unpolarized broad spectrum light source. The spectrum reveals two strong absorption bands at 550 and 650 nm. These correspond to transitions from the d-band to sp-band in the conduction band at the X and L zone centers of the Au Brillouin zone [68]. The locations of the SPP modes in Figure 3.3(a) have a one to one correspondence to the photoluminescence modes of Au nanorods reported by Imura et al.[69] Note that the observation of two SPP modes of Au is typically only observed with nanohole arrays [70]–[73]. Based on the cross-sectional SEM of the Au pyramids in Figure 3.2, one can assume that the scattering from the surface of the pyramids is due to the Au cavities on the surface of the pyramid created between two neighboring surface plateaus. Based on the plasmonic properties of Au nanorods [69] and Au nanohole

arrays[70]–[73] and their similarity to the scattering spectrum of the Au pyramids, we propose that the cavities on the pyramid surface and their alignment of 30° relative to the mirror plane of the pyramid face produce the scattering spectrum in Figure 3.3(a). Specifically, the scattering spectrum is a function of the large aspect ratio of the plateaus and their alignment to one another. In effect, the surface texturing of each pyramid is a natural 2D quasiperiodic plasmonic array. The spacing between aligned cavities ranges from 200-500 nm and therefore on the order of the wavelength of visible light, ergo, perfectly capable of producing collective optical effects of scattered light.

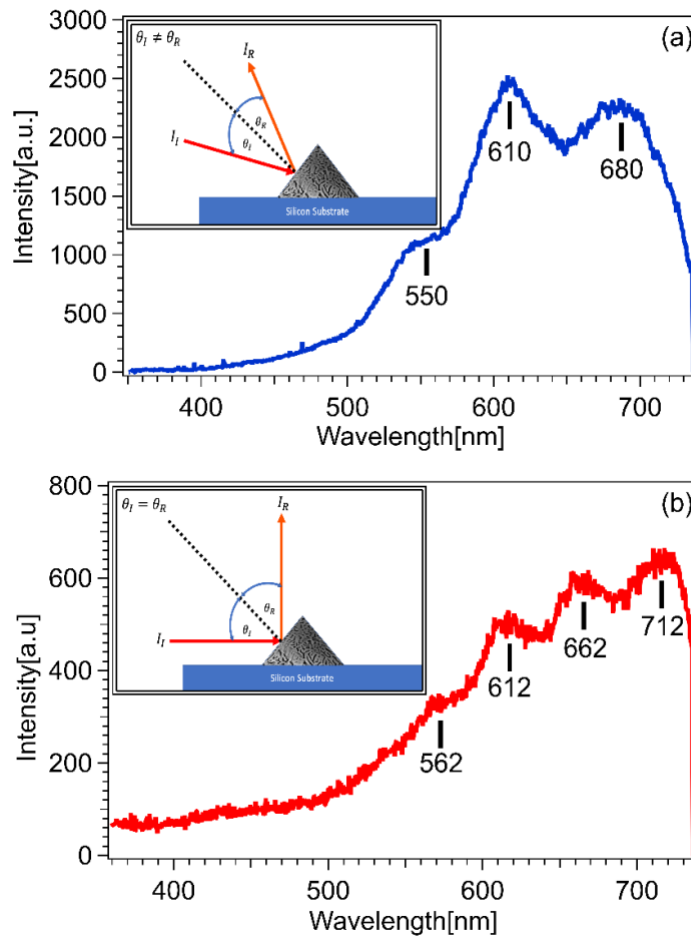


Figure 3.3 (a) The scattering spectrum of an Au pyramid. (b) Far field specular data taken with the same light source.

The plasmonic array produced by the plateaus can be approximated either as the superposition of two parallel gratings offset from one another by 60° or more coarsely as an array of chevrons aligned along the mirror plane of the face of the pyramid. Both of these configurations have been used in a variety of metaoptics designs [22], [74]–[79]. The superposition of the two orientations of the plateaus on the pyramids will produce linearly polarized light, where the polarization vector is parallel to the mirror plane of the pyramid face. Assuming the scattered light from each side of the mirror plane of the pyramid face are in phase, the superposition of the two polarized wavefronts, \hat{n}_{net} , is defined as,

$$\begin{aligned}\hat{n}_{net} &= \hat{n}_1 + \hat{n}_2 \\ &= (\cos\theta\hat{y} + \sin\theta\hat{z}) + (-\cos\theta\hat{y} + \sin\theta\hat{z}) \\ &= 2\sin\theta\hat{z}\end{aligned}$$

where \hat{y} is parallel to the base of the pyramid face and \hat{z} is parallel to the mirror plane. In order to test this hypothesis, specular reflection measurements were conducted on the Au pyramids. Displayed in Figure 3.3(b) is a representative specular reflectivity spectrum. The spectrum exhibits what appear to be four absorption bands, i.e. four SPP modes. However, this is not the case since the wavelength spacing between the peaks or valleys is a constant value of 50 nm. Consequently, the peaks and valleys derive from interference phenomena. It has been determined that they are beats arising from interference within the spectrometer itself. This was confirmed by the removal of the fiber optic cable from the experimental setup, coupling the spectrometer directly to our microscope. The observation of beats in Figure 3.3(b) is a verification that reflection of light by the Au pyramids produces polarized light. The pyramids, therefore, are multifunctional in that they are strong SPP structures as well as polarizers. We hypothesize that

the latter capability will produce additional interesting optical phenomena that is worthy of further investigation. To directly verify that the reflected light is polarized, the light source was passed through a polarizer and the intensity of multiple regions of the spectrum in Fig. 3(a) were measured as a function of polarization angle. The scattered light intensity as a function of the angle of polarization is displayed in Fig. 4. The maxima occur when the polarization is parallel to the mirror plane of the face of the pyramid ($\pi = 0$ and $\pi / 2$). An excellent fit of the experimental data is obtained with a sinusoidal function (red curve in Fig. 4). The surface of the pyramids produces p-polarized light parallel to the mirror plane of the faces of the pyramid. The results in Fig. 4 demonstrate that light scattering off the pyramid produces polarized light, and that maximum scattering of polarized light occurs for a polarization parallel to the mirror planes of the faces of the pyramids, i.e. p-polarized light.

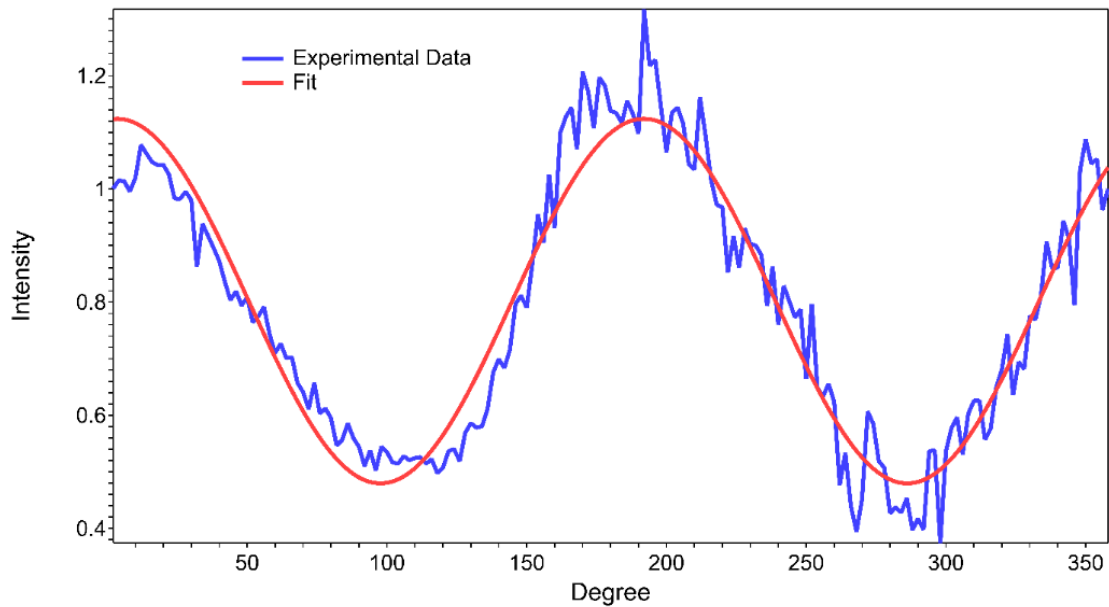


Figure 3.4 Specular collected polarized light intensity as a function of polarization angle from the surface of a pyramid.

Section 5: Conclusion

In summary, mesoscopic Au polyhedron structures (pyramids) with unique nanoscale texturing were produced by annealing a 25 nm Au thin films on a Si [100] substrate and are product of the formation of an Au-Si eutectic, Au diffusion and subsequent phase separation of the eutectic [80]. Greater than 50% of the pyramid is subsurface. The indexing of the pyramids to one another along the [001] and [010] directions of the Si(100) surface) is due to eutectic formation-induced preferential etching of the Si substrate. The pyramids have a sponge-like structure due to the reabsorption of Si into the substrate upon cooling. This morphology extends to the surface, and in the case of large pyramids, produces a chevron-like surface topology that is well suited for launching surface plasmon polaritons, as determined by scattering spectroscopy (non-specular reflectivity). In addition to launching SPP, the chevrons produce polarized light for specular reflection. The simplicity of the process and modest cost of production lends itself to the development of new technology, such as SPP sensors[81], light polarizing optical elements and metaoptics [82].

CHAPTER IV

GOLD-SILICIDE EUTECTIC DYNAMICS AND MESOPYRAMID FORMATION

Section 1: Introduction

In this chapter I expand on the work presented in the previous chapter with respect to pyramid formation. Mesopyramid formation is a dynamic process with many dependent variables to be considered. This chapter presents the steps from start to finish of mesopyramid formation beginning with the tri-layer of Au and Si and ending with the phase separation of the eutectic and final elemental configuration of pyramids. This diction will be supported by the binary phase diagram of AuSi and a computational kinetic model of a binary phase separation.

Eutectics are a fascinating class of a material having a lower melting point than that of its individual components, thereby, broadening their use where their constituents would be excluded due to their high melting temperatures [83]. In the never-ending search for new materials or new morphologies of known materials, phase separation of a eutectic could be harnessed to produce materials with unique morphologies that, in turn, produce new and unique physical properties. In fact, phase separation has been utilized to create unique morphologies in polymers [84]–[89] and alloys [85], [88], [90]–[100], for use in photovoltaics[85], [87], sensors [89] and photonics [88], [90], to name a few. One of the most well studied eutectics is gold silicide because of their well-established affinity for one another [101]–[107]. By combining gold (Au) and silicon (Si) at different ratios, researchers have been able to form different phases of these industrially

Begin relevant elements in unique forms such as nanowires, nanosprings and nanorods [106]–[108].

The fundamental kinetics of AuSi that leads to a phase separation is well established [8][109][110], yet the opportunity to harness this phenomena for technological applications has yet to be fully realized. For example, Au is a well-known plasmonic material, where Au nanoparticles support stationary surface plasmon (SP) states [111][112][113] and Au films support non-stationary surface plasmon polaritons [114][115][116]. Therefore, phase separation of the AuSi eutectic is a potential process for producing Au plasmonic materials given that it is well established in the literature that Au supports on Si produce interesting nanoscale structures [7], [50]–[52] [117]. Presented herein are the results of the eutectic induced formation of Au mesopyramids. The effect of the maximum temperature of the eutectic on phase separation upon cooling is also investigated, as well as the subsequent stoichiometry of the Au mesopyramids.

This study differs from the majority of phase separation studies in that the substrate is an active participant in the process. Specifically, the substrate serves as reservoir of Si for the formation of the AuSi eutectic and a sink for Si during phase separation. This added degree of freedom has profound effects on the morphology and stoichiometry of the Au structures that form upon phase separation. The process described below produces Au polyhedron shaped structures, which are hereon referred to as mesopyramids (MP), with dimensions on the order of tens of microns. The structures have surfaces consisting of plateaus and channels and an interior with numerous voids. Their formation can be understood by examining the free energy of the system and mass transport between the MP and the Si substrate.

Section 2: Au Mesopyramid Preparation

The samples were prepared on RCA cleaned P-type Si(100) with and without a native oxide for the purpose of gaining a better understanding of the role of the native oxide on MP formation. First a 10 nm layer of Au was deposited, followed by a 4 nm layer of Si and then a 10

nm Au capping layer. The purpose of the Au capping layer was to mitigate oxidation of the Si layer. Gold and silicon were deposited by magnetron sputtering at rates of 1.25nm/s and 0.66nm/s, respectively. The calibration of the deposition rates was determined using a Bruker MMRC DektakXT Stylus Profilometer. The thickness of the layers ensured a Si:Au ratio of 1:5, which will produce a AuSi eutectic containing 19% silicon with a corresponding melting temperature of 362°C [118]. The samples were annealed in a custom-built vacuum oven consisting of a closed heater module inside a vacuum chamber. The chamber pressure was maintained at 150mTorr \pm 5mTorr during the warmup, soak, and cool down phases of growth by simultaneously pumping with a mechanical pump and a controlled leak of atmosphere into the chamber via a leak valve.

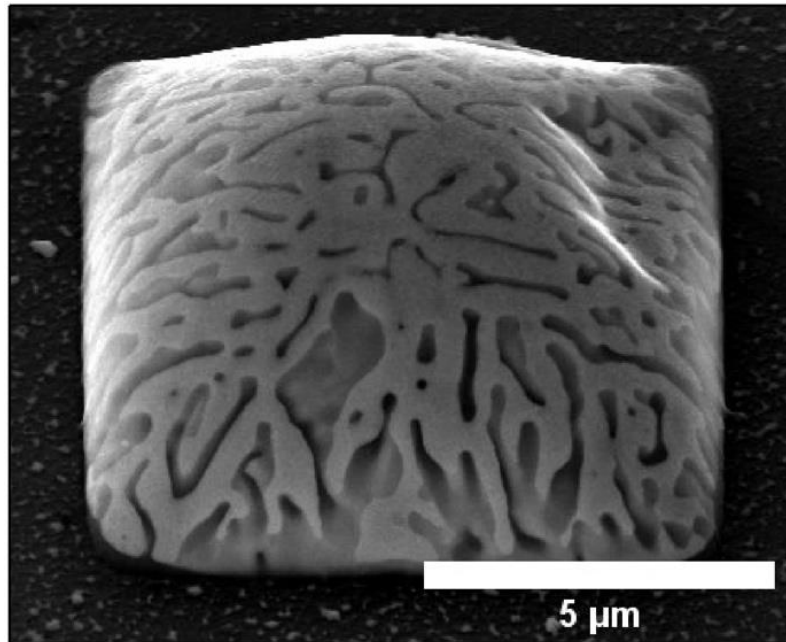


Figure 4.1 An SEM micrograph of a mesopyramid taken at 17 degrees with respect to the horizontal plane to illustrate the pyramid like geometry.

A typical growth consists of a ramp rate of 23 oC/min. to the maximum temperature, followed by a soak for 30 min., then heater power is cut, and the system passively cools down. The typical cool down rate from a maximum temperature of 700 oC to 300 oC, which is below the eutectic melting temperature of ~360 oC, is typically 20 oC/min. A scanning electron microscope (SEM) micrograph of a typical MP grown at 700 oC is presented in Figure 4.1. The MP is approximately 9 μm x 9 μm , however, MP with sides in excess of 50 μm have been observed. While the height of this as-grown MP cannot be determined from the micrograph, their heights typically range from 2-5 μm depending on their size.

The surface morphology of the MP in Figure 4.1 is typical of MP of this size or larger. The surface can be described as a series of channels that cut into, and run parallel, to the surface with corresponding elongated plateaus in between. The interior of the MP is porous in nature with large micron scale cavities, which is discussed below. The surface and bulk morphologies are attributed to phase separation and the primary subject of this work. To investigate the eutectic kinetics of MP formation, a series of mesopyramid samples were grown with increasing maximum temperatures. All samples were prepared in the aforementioned manner with the same thin film ratios and thicknesses. A total of four samples were annealed at successively higher maximum temperatures in steps of 100°C from 400°C and to 700°C. Once a sample reached its maximum temperature the heater power was turned off (no soak cycle) and they were allowed to cool.

Section 3: Sample Characterization

The scanning electron microscopy (SEM) micrographs and elemental analysis of the MP were acquired with an FEI Quanta 600 field emission ESEM equipped with a Bruker energy dispersive X-ray spectrometer (EDS). The x-ray probe energy was 5 KeV to ensure shallow probe depth, i.e., probe depths of gold and silicon of 30nm and 10nm, respectively. In order

characterize the morphology and elemental composition of the interior of the MP using SEM, the samples were cleaved in half, cast in a polymer resin to stabilize the MP, and the cleaved edge polished. Stabilization was needed to keep the MP from excessively deforming or smearing during polishing. Polishing was performed using an Allied High Tech Miltiprep System Precision Polisher. This produced an ultra-smooth cross section of the MP that preserved the cross-sectional morphology of the MP. Cross sectional SEM imaging and EDS analysis were performed on the polished samples without a C or Au conductive coating. The EDS line scan analysis was performed with an electron energy of 5 keV, which corresponds to a probe depth of 100 nm for gold and 300 nm for silicon, respectively. The line scan was chosen over that of a single point to obtain an average atomic ratio Si and AU within the MP. Three pyramids with similar dimensions were analyzed for each maximum annealing temperature.

Section 4: Results

The Au mesoscopic pyramid in Figure 4.1 is representative of the larger structures produced. The MP have a rectangular base with sides that range from a few microns to tens of microns and heights in the range of 2-5 microns. Ergo, the base of the MP is much larger than the height. The micrograph in Fig. 1 was taken at 17° with respect to the surface of the substrate to accentuate the polyhedron shape of the structures, ergo, the use of mesopyramid as a descriptor. The angle of the facets on these pyramids is a function of the ratio of the base to the height. The surface topography of a pyramid consists of channels that cut into their surface bounded by plateaus. The channels/plateaus are on the order of 1 μm in width and microns in length. The orientation of the channels is on average is such that they radiate outward from the center of the MP to the perimeter. Another unique feature of some but not all MP is the distorted region in the upper right side of the MP in Figure 4.1, where this region of the MP has collapsed. This is more pronounced in the center of the MP in Figure 4.2. Note the ripples of distortion encircling the collapsed zone. The authors attribute to phase separation of Au and Si and the subsequent

destabilization of the MP's mechanical integrity. This is a topic of future study and will not be addressed at this time.

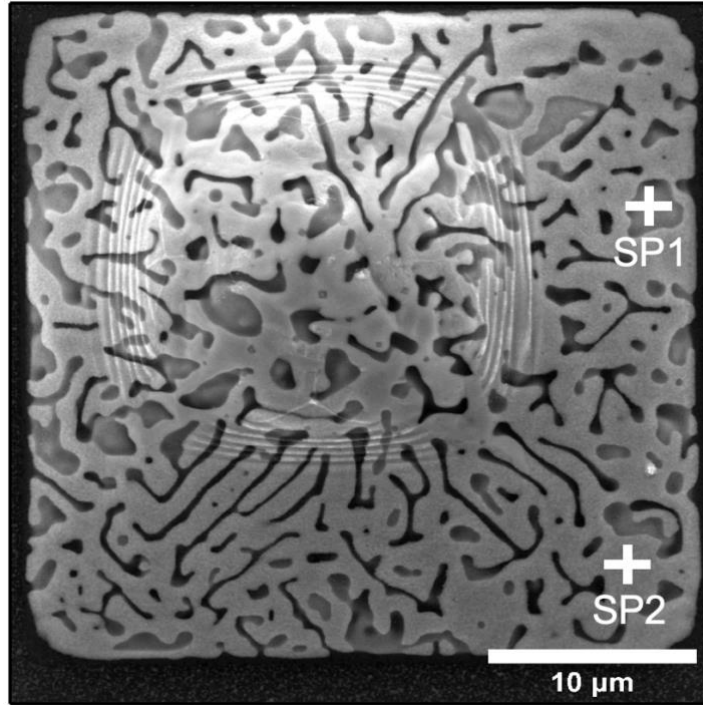


Figure 4.2 An SEM top-down micrograph of a mesopyramid, where the crosses marked SP1 (channel) and SP2 (plateau) indicate the locations where EDS analysis was performed.

The Si and Au composition of the bottom of the channels and the top of the plateaus was analyzed using EDS. The crosses labelled SP1 and SP2 in Figure 4.2 indicate the locations where EDS spectra were acquired. The x-ray intensity was 5 KeV. The normalized at.% of Si and Au at SP1 (channel) are 54% and 46%, respectively. At SP2 (plateau), the normalized at.% of Si is 12% and 88% for Au. Note that these values are not an exact quantitative measurement of the atomic percentages because neighboring regions may be contributing to the signal, which may explain the ~7:1 ratio of Au:Si, as opposed to the 5:1 ratio reported by Green at al. [102]. Instead, they demonstrate the relative differences in the ratios of Si to Au between the two regions, which in turn provides insight into the origin of their formation. Namely, the near surface region of the

bottom of the channels are Si rich relative to the corresponding sample volume of the plateaus. This is attributed to phase separation [119], where at some point the channels were filled with Si and will be addressed in detail shortly.

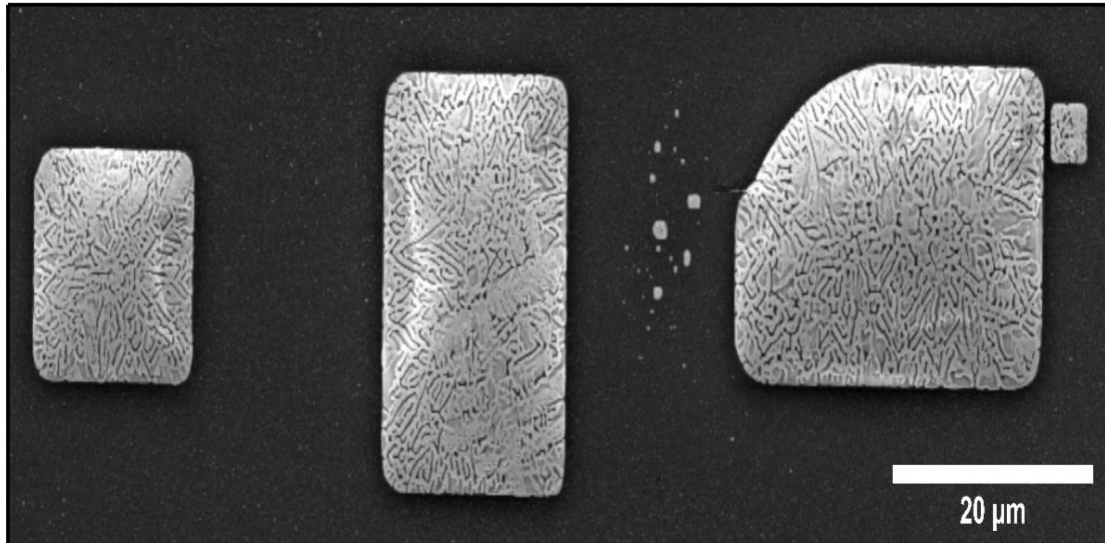


Figure 4.3 An SEM micrograph of three aligned mesopyramids.

In addition to isolated MP, clusters of MPs are observed, as in Figure 4.3. The pyramids are predominantly rectangular, but are occasionally misshapen, like the large pyramid on the right of Figure 4.3. This could be due to defects in the bulk lattice of the Si substrate. More importantly, all the MP, regardless of their size, are aligned with one another, parallel to the [001] and [010] directions of the Si(100) surface, which is consistent with previous reports [7], [50]–[52]. The alignment is indicative of indexing of the MP with the Si substrate. Therefore, the substrate is an active participant in mesopyramid formation. Displayed in Figure 4.3 is a SEM image of the remnants of a MP that reveals the etching pattern of the eutectic into the Si substrate.

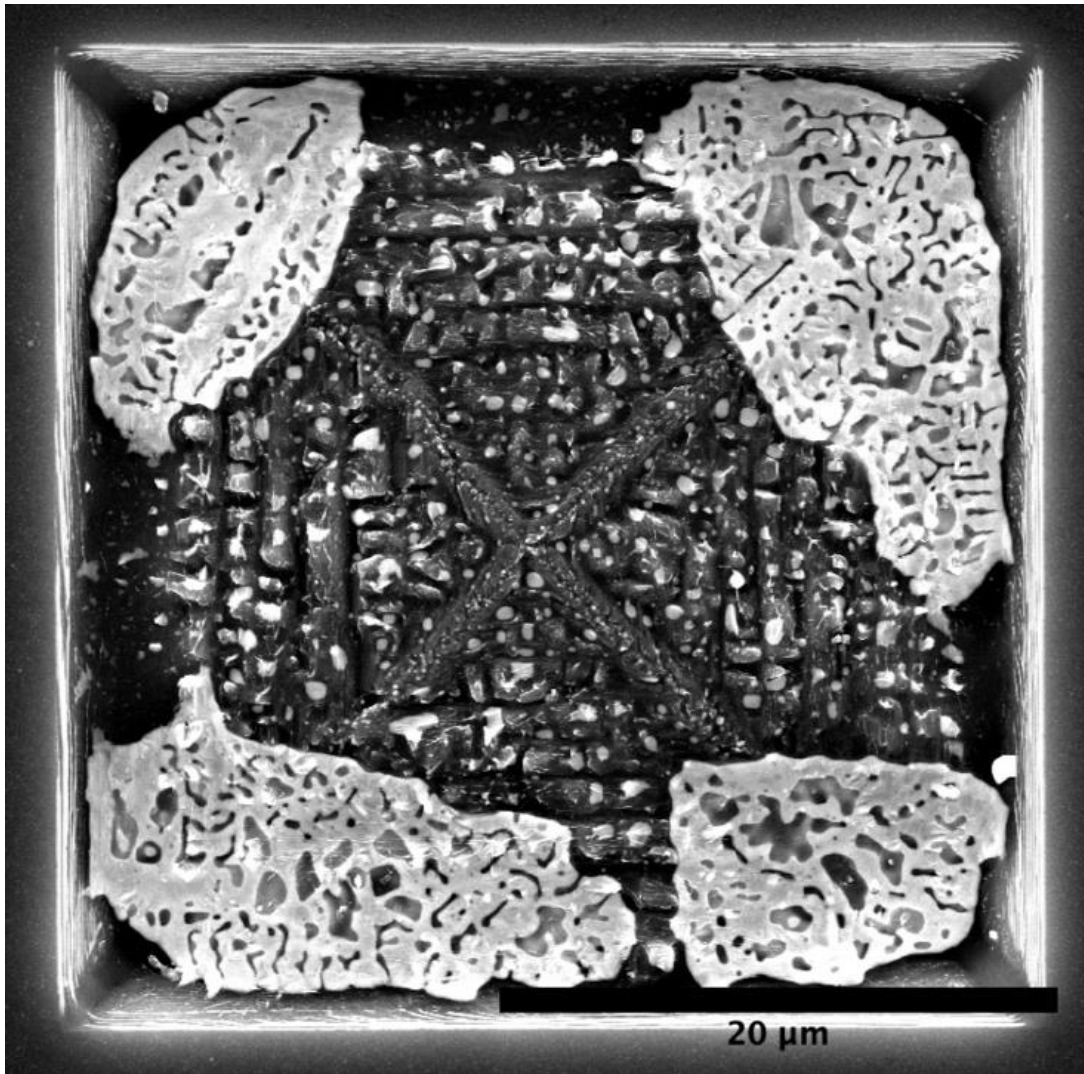


Figure 4.4 An SEM micrograph of AuSi eutectic-induced etching of the Si substrate.

The eutectic preferentially etches the Si substrate in the $[010]$, $[0\bar{1}0]$, $[001]$ and $[00\bar{1}]$ directions, creating a rectangular trough in the surface. See Figure 4.4. Therefore, the alignment and four-fold symmetry of the MP is due to the preferential etching in the aforementioned crystal directions. The cross corresponds to the boundary between two orthogonal crystal directions.

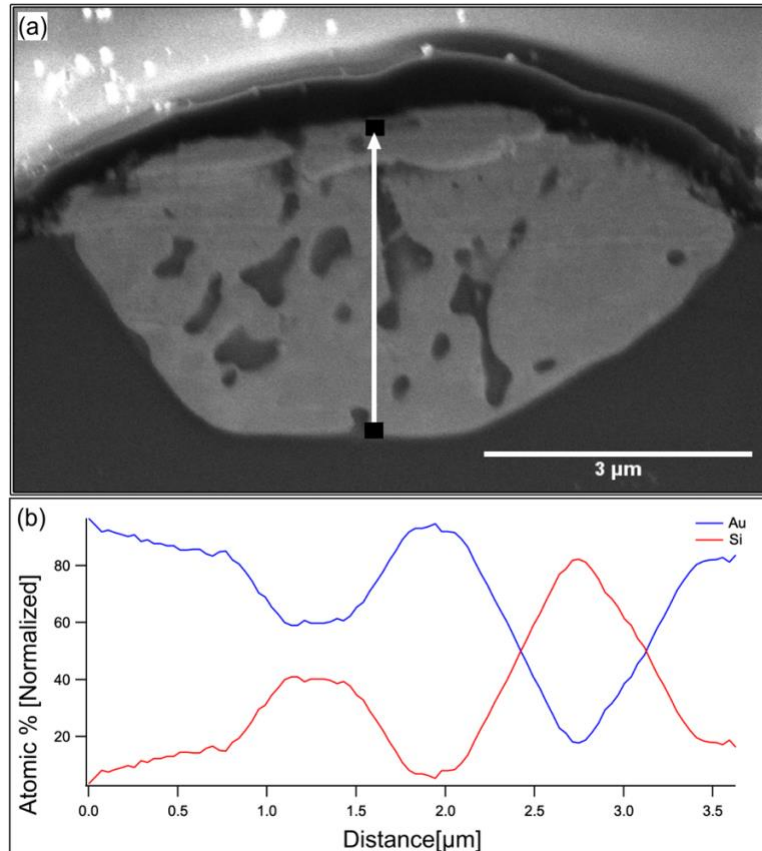


Figure 4.5 (a) An SEM micrograph of the cross section of an Au mesopyramid. The bright region above the pyramid is epoxy used to cast the sample for cross-sectioning. The dark regions within the pyramid are cavities that form due to phase separation of the AuSi eutectic. (b) The elemental at% line scan for Si and Au along and in the direction of the white arrow in (a).

Cross sectional SEM was performed to better understand MP formation. An example is displayed in Figure 4.5(a). Note that the top of the MP was slightly deformed by the casting process, where the bright region above the MP is the polymer. Figure 4.5(a) shows that the majority of the MP is subsurface, and that the Si substrate is partially consumed during formation. In effect, Si from the substrate is incorporated into the MP. The dark regions in Figure 4.5(a) are voids, similar to the channels on the surface, but vertically orientated to the surface of the MP. The white arrow in Figure 4.5(a) indicates the position and direction of the EDS line scan

analysis of the MP. The data was truncated as is indicated at the black boxes at both ends of the line scan arrow to avoid spikes in the silicon signal due to the proximity to the substrate/MP interface or a precipitous drop in Au signal at the polymer/MP interface. The normalized at.% concentrations of Si and Au as a function of location is displayed in Figure 4.5(b). Once again, the relevant information is the ratio of Si to Au, as opposed to their absolute values. The solid regions of the pyramid are primarily Au. However, the spikes in the at.% of Si correlate with the regions of the line scan that pass near or over the voids, which is consistent with the EDS analysis of the channels and plateaus at the surface of the pyramids. Note that approximately two thirds of the MP is subsurface.

Section 5: Discussion

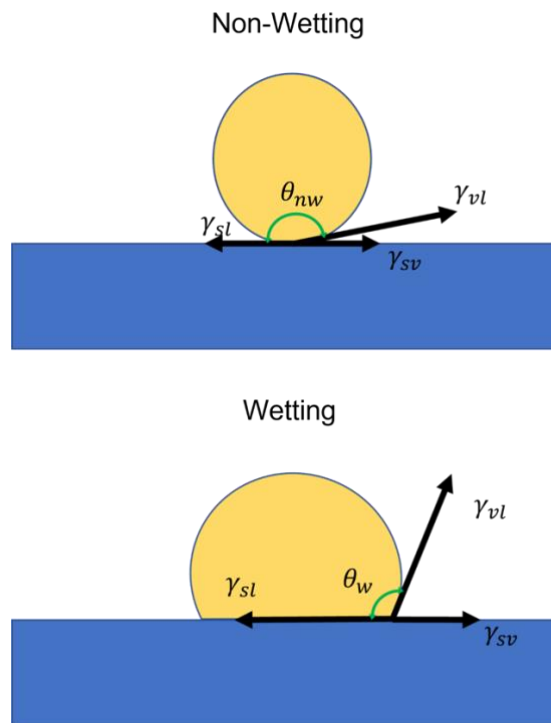


Figure 4.6 A schematic diagram of the surface tensions of a liquid drop on a solid surface for non-wetting (top) and wetting (bottom) geometries. γ_{sl} , γ_{vl} , and γ_{sv} are the surface tensions at the solid-liquid, vapor-liquid, and solid-vapor interfaces, respectively.

The ability of the eutectic to etch the Si substrate (Figure 4.4) is mitigated by the native oxide layer on the surface of the silicon substrate, as suggested by Ishikawa et al. [120]. While it is well established that Au will readily diffuse into Si with annealing [61], the native oxide acts as a barrier to diffusion of Si from the substrate (Si reservoir) into the Au layer. In addition, wetting of SiO₂ by Au increases with increasing temperature, as determined by the contact angle [7]. Therefore, the energetics of the Au/SiO₂/Si interface is critical to the initial phase of MP formation. Thermodynamically, the work of adhesion of Au on Si or Au on SiO₂ is a function of the surface tension between the solid-liquid (γ_{SL}), vapor-liquid (γ_{VL}) and the solid-vapor (γ_{SV}) interfaces and is macroscopically described by the contact angle (θ). Generally speaking, $\theta < 90^\circ$ corresponds to wetting and $\theta > 90^\circ$ to nonwetting (see Figure 4.6). In the present study, work of adhesion of the system is dictated by the chemistry of the surface and the composition of the Au layer. It is well documented that the annealing of Au films on Si with either a native oxide [121] or a thick thermal oxide [122] causes the film to break up into irregularly shaped droplets. The fact that the droplets are not spherical indicates that the Au/SiO₂ interface is not perfectly dewetting, i.e., the work of adhesion is higher than a system where Au forms spherical droplets. Furthermore, the imperfect nature of the nonwetting assists with MP formation. To test this hypothesis, a sample was prepared where the native oxide on a Si wafer was chemically removed with HF, the tri-layer of Au/Si/Au immediately sputtered onto the surface and placed in the oven and the sample annealed in the same manner required to produce MP. No pyramids formed on this sample. The experiment was repeated multiple times, and in all cases, pyramids were not observed. Instead, a stochastic array of near spherical droplets covered the substrate. This does not exclude the formation of MP if annealed at 900 °C or higher but demonstrates that it is energetically unlikely with the conditions of this study (annealing temperature, pressure, Au thickness). We therefore argue that the lack of MP formation is the transition of the system from a semi-wetting environment to a nonwetting environment upon the removal of the native oxide.

The impact of the nonwetting environment is multifaceted. First, the work of adhesion is greater for a nonwetting environment than a wetting environment [123], which in turn affects the ability of the AuSi eutectic to scavenge Si from the substrate. To understand this, consider the work of adhesion to be a measure of the energy needed to remove an Au atom from the Au droplet [123], which is supported by the fact that the enthalpy of fusion of AuSi is ~6-7 KJ/mol [8], [124] and significantly lower than ~12-13 KJ/mol [125] for Au, ~ 12 KJ/mol for Si [126], and ~ 9 KJ/mol for SiO₂ [127]. Therefore, in the wetting environment, less energy is required to remove an Au atom from the droplet to form the eutectic. This argument can be extended to Au surface diffusion. Specifically, the wetting environment favors the release of Au from the droplet, thereby facilitating Au surface diffusion. Assuming that diffusing Au atoms need to find a defect in the native oxide for MP to form [120], [128], the greater the number of Au atoms diffusing across the surface, the greater the probability that they will find said defects. The observation of lines of MP nucleated along scratches on the Si substrate supports the hypothesis of defect induced nucleation. Wetting can also affect the size of the MP. Typically, large MP are surrounded by circular denuded zones [9], [128], indicative of Au surface diffusion to the MP in the center of the denuded zone. However, smaller Au pyramids like the ones in Figure 4.3 are observed near larger MP, but typically outside the denuded zone. The scarcity of these smaller MP in the proximity of larger MP is indicative of Ostwald ripening [129]–[131]. In this case, too, wetting of Au on SiO₂ assists ripening because of the lower surface diffusion activation energy of Au on SiO₂ [104] relative to Si [132].

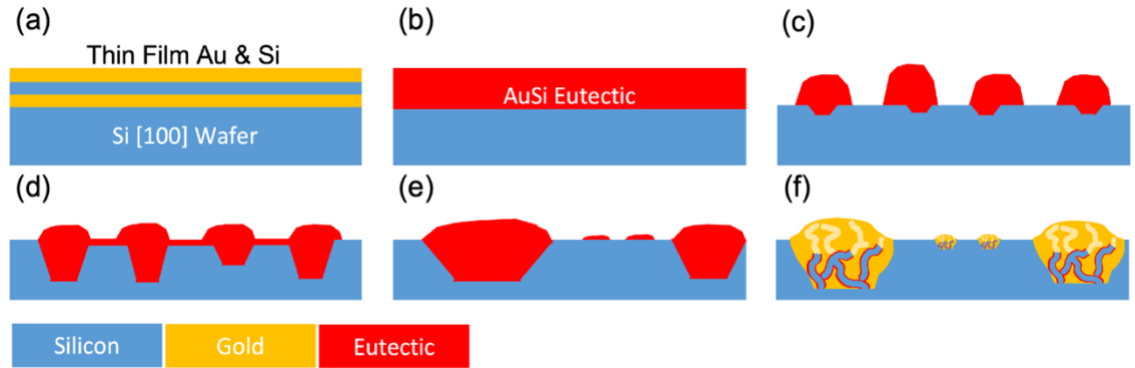


Figure 4.7 Mesopyramid formation process: (a)Thin Au & Si film deposition. (b) Formation of eutectic at $T > T_E$. (c) Nucleation of mesopyramids at silicon oxide film defects (d) Etching along primary axis of Si substrate. (e) Mesopyramid growth due to Ostwald ripening. (f) During cool down phase separation occurs and a eutectic boundary layer forms at the interface of the two phases through which Si diffuses back into the Si Substrate. A native oxide at the Si surface is assumed but not shown.

With an understanding of the importance of the wetting environment on the energetics of MP formation, the keys steps of their formation are illustrated in Figure 4.7. Starting with the Au/Si/Au tri-layer film (Figure 4.7(a)), the initial phase of MP formation upon heating is the transformation of the tri-layer into a single AuSi eutectic layer (Figure 4.7(b)). This primes the system to be at or near the percentage of silicon to gold ratio necessary to achieve a eutectic with the lowest temperature of 362 °C, ergo, the AuSi eutectic forms at an annealing temperature in the neighborhood of 362 °C. We hypothesize that the eutectic lowers the activation energy of Au diffusion into the Si substrate and/or Si from the substrate into the eutectic. With the eutectic formed and a temperature above 362 °C, the eutectic breaks up into droplets, concomitant with nucleation at defects in the native oxide [128], as depicted in Figure 4.7(c). This process is highly dynamic due to the rapidly changing environment associated with eutectic formation. At a sufficiently high temperature the eutectic begins to incorporate Si from the substrate, i.e. a subsurface eutectic phase, as depicted in Figure 4.7(d). This is accompanied by surface diffusion

of Au to regions where the subsurface eutectic is established, under the assumption that the probability of adding an Au atom is larger than the probability of an Au diffusing away. However, this is not to say that Au diffuse from nucleation sites are forbidden. Concomitant with the accumulation of Au is the consumption of Si from the substrate [133], i.e. one Si atom for every Au atom added, which results in the growth of the MP above and below the surface. Eventually, diffusion between nucleation sites leads to Ostwald ripening and the formation of large MP at the expense of smaller MP (Figure 4.7(e)). We suggest that a complete model of the formation and subsequent Ostwald ripening of mesopyramids accounts for subsurface diffusion of Au between MPs. The final step of MP formation (Figure 4.7(f)) is the phase separation of Au and Si and the reincorporation of Si into the substrate. This is the most intriguing aspect of MP formation and worthy of further discussion.

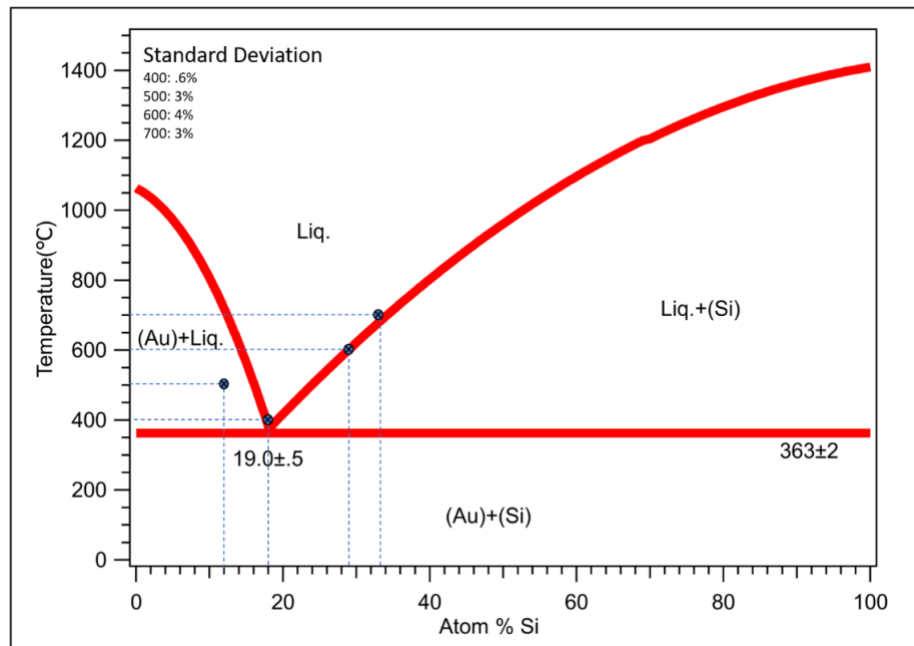


Figure 4.8 AuSi phase diagram superimposed with experimental data.

The concentration of Si in the eutectic is a function of the annealing temperature per *the binary phase diagram* of AuSi Eutectic in Figure 4.8 [44]. Therefore, this should be reflected in

the average concentration in MP with rapid quenching that doesn't inhibit phase separation but does limit the reincorporation of Si into the substrate. It is our hypothesis that the concentration of Si in the MP prior to cooling is manifested in the post cooling concentration. This hypothesis has been tested by annealing four samples to 400 °C, 500 °C, 600 °C and 700 °C, respectively, and immediately allowed to cool. Cross sectional EDS line scans were acquired for three MP per sample, where care was taken to use similar sized MP. The average at.% of Si in a MP as a function of the maximum annealing temperature is overlaid on the AuSi phase diagram in Figure 4.8. As expected, the data demonstrates that the load capacity of Si in the eutectic is a function of the maximum annealing temperature. Note that these values are not an indication of the maximum at.% of Si over the course of the experiment since some Si may have been reincorporated into the substrate. Interestingly, the at.% of Si of three of the four samples falls on the eutectic boundary. This supports the hypothesis by Ferralis et al. [133] that during a controlled cool down the at. % of Si in the eutectic tracks the eutectic phase boundary or liquidous line.

We now turn our attention to AuSi phase separation. A computational three-stage phase separation kinetics model of a liquid binary mixture by Hazra et al. [134] correlates well with the observations reported herein. The model uses a single position, time dependent order parameter,

$$\phi(r, t) = x_A(r, t) - x_B(r, t)$$

where $x_A(r, t)$ and $x_B(r, t)$ are the mole fractions of the solvent and solute, respectively. In the present case, Au is the solvent and Si is the solute. All interactions are expressed in terms of Lennard-Jones potentials. In the present case, this is the potential between atoms of silicon and gold. In conjunction with the Langevin equation, the following generalized Langevin equation for the order parameter is derived:

$$\ddot{\phi} + \zeta \dot{\phi} + \omega^2 \phi = A(t)$$

where ζ represents dynamical friction, $A(t)$ is a random force term characteristic of Brownian motion and related to ζ [134], and $\omega^2\phi$ is the rate of change of the velocity with respect to ϕ , respectively. The solution to the above equation has exponential growth during the initial stages of phase separation, i.e the formation of domains of the solute (Si). The next stage of phase separation is characterized by the presence of slow dynamics (power law behavior), which is dominated by diffusion and evaporation. Evaporation in this context is defined as the migration of Si out of domains of Au. In addition, domains of Si merge with one another, akin to Ostwald ripening. Further coarsening into spinodal bands occurs, i.e. spinodal decomposition [135]–[137]. Evidence of spinodal decomposition within the MP has previously been reported [138]. The final stage of the three-stage phase separation kinetics model is characterized by a smoothing of the newly formed boundaries between the areas of high silicon and gold concentrations following a logarithmic fit to the evolution of the order parameter. Evidence for this final stage of the kinetic model, as it pertains to the evolution of the MP, is the relatively smooth walls of the channels on the surface of the MP in Figures. 4.1 and 4.2, and similarly, the voids in the interior of the MP in Figure 4.5(a). Therefore, the three-stage model of phase separation accurately describes the phase separation in the MP.

One aspect of the of MP formation that the three-stage model of Hazra et al. [134] does not account for is the formation of the voids themselves because in the simulation the system is quenched in such a way that the Lennard-Jones fluid-solid transition is avoided, which is clearly not the case for the AuSi eutectic as a function of at.% of Si in Au or Au in Si. In effect, the model isn't designed for the formation of channels on the surface of the MP or voids within the interior. The following model is proposed for their formation. We begin with the assumption that a gold silicide layer exists at the boundaries of the spinodal bands. This is supported by the work of Green et al. [102] who after high temperature annealing observed a 30 Å thick gold silicide layer on the surface of an Au film supported on. In the case of the MP, the AuSi eutectic at the

interface of the spinodal band acts as a “highway”, whereby Si in the spinodal bands diffuses to the Si substrate, as depicted in Figure 4.7(f), thereby creating the channels in the surface and voids within the interior of the MP. As Si is reincorporated into the Si substrate, Si is ‘harvested’ from the spinodal bands to maintain the eutectic boundary layer if the temperature is above the minimum eutectic temperature. In effect, the eutectic boundary layer follows the liquidus in the AuSi phase diagram Fig. 8 per our experimental observations. The EDS line scan data in Figure 4.5(b) clearly shows a correlation between increases in the Si signal and proximity to the walls of voids. We postulate that trace amounts of silicon remain in or on the walls of the cavities. The surface channels similarly form but in this case Si travels to the edge of the MP and is reincorporated into the substrate. In effect, we are proposing a modified three-stage model that takes into account the solidification of both Au and Si upon phase separation except for at a boundary layer separating them.

Section 6: Conclusion

By applying the fundamental governing principles of eutectic dynamics to gold silicide, a comprehensive multistage model has been developed to describe the formation of polyhedron shaped Au mesostructures, referred to as mesopyramids. The formation of the structures requires participation of the Si substrate, both as a source and sink of Si, as well as template for the shape, alignment, and morphology of the mesopyramids. Because of the participation, the system is more complicated than a simple binary phase transition. Correlation of the AuSi phase diagram and with experimental results demonstrate that the stages of mesopyramid formation is driven by minimization of the free energy, which tracks the liquidus line of the eutectic phase diagram. Finally, the unique surface and bulk morphologies are realized through the participation of the substrate, which in turn, requires a modified phase separation kinetics model of a liquid binary mixture to reproduce the experimental results. From the standpoint of materials processing, eutectic phase separation can be exploited as a way to create large areas with the surface

morphology reported here. The square geometry of the MP should exhibit interesting diffraction properties and is topic of future study. Furthermore, they could be useful for meta-optics, surface enhanced Raman spectroscopy sensors and surface plasmon polariton technology.

CHAPTER V

FAR-FIELD DIFFRACTION AND OPTICAL PROPERTIES FROM MESO-SCALED AU PYRAMIDS

Section 1: Introduction

In this chapter we change our focus from the eutectic dynamics of mesopyramid growth to the optical properties of these structures. The first optical investigation was an analysis of the surface properties of light interacting with the pyramids and the diffraction patterns produced. Important to this work was the discovery of a second configuration of mesopyramid that will be discussed shortly. This new geometry will have important implication with respect to the plasmonic properties that will be presented later. With a simple experimental setup, we demonstrate these structures' ability to behave as spherical mirrors. This approximation is supported by a model that is in good agreement with our physical results.

Herein we present results of a diffraction experiment obtained from the surface of 3D meso-scaled Au pyramidal and inverse pyramidal structures formed on Si(100) [139]–[141], where the former refers to convex structures that protrude from the surface, henceforth referred to as mesopyramids (MP). The latter refers to concave structures that are depressed into the substrate, henceforth referred to as inverse mesopyramids (IMP). The four-fold pyramid-like geometry is easily identifiable when illuminated and visualized from directly above their apex or the bottom in the case of the IMP. The far-field reflectivity of the two types of structures is examined.

Analysis of their corresponding far-field diffraction patterns and lensing properties exhibit similar and dissimilar optical characteristics. Combining the far-field properties with their SPP activity has the potential to lead to a new family of metaoptics.

Section 2: Materials Preparation and Experimental Details

A detailed explanation of MP and AMP fabrication can be found in Refs. [138]. Briefly, mesopyramids are grown on RCA cleaned Si(100) with a native oxide. A tri-layer of Au/Si/Au at a ratio of 10nm/4nm/10nm is sputtered onto the substrate. The purpose of the tri-layer is to promote the formation of the AuSi eutectic, thereby lowering the processing temperature. The native oxide on the Si surface enhances wetting of the surface, which energetically favors interactions between the AuSi eutectic and the substrate. The structures are formed by annealing at 750 °C in a custom-built reactor at a pressure of ~150 mTorr. The annealing process consists of a 15 min. ramp from room temperature to the maximum temperature, soaking for 30 min. at the maximum annealing temperature, at which point the reactor is turned off and the sample allowed to cool down under vacuum. Micrographs of the MP and IMP were acquired with a FEI Quanta 600E Scanning Electron Microscope. Surface profiles of the meso-structures were acquired with Oxford Asylum MFP3D Infinity Atomic Force Microscope (AFM). The AFM data was acquired in tapping mode using a AC160TS-R3 silicon tip with a 7nm end radius. This mode was chosen due to the delicate nature of the structures. Any physical contact with the samples had the risk of altering their morphology and adversely affecting the diffraction measurements. The significant differences between the extremes of the height profiles of the MP and IMP relative to the substrate at times caused the tip to drift far from near resonance, where the time for the tip to reestablish its near resonance frequency typically exceeded the line scan rate. This drift produces artifacts in the form of troughs in the 2D map. To mitigate this effect, the line analysis for the height differential was done perpendicular to the longitudinal path of the AFM tip.

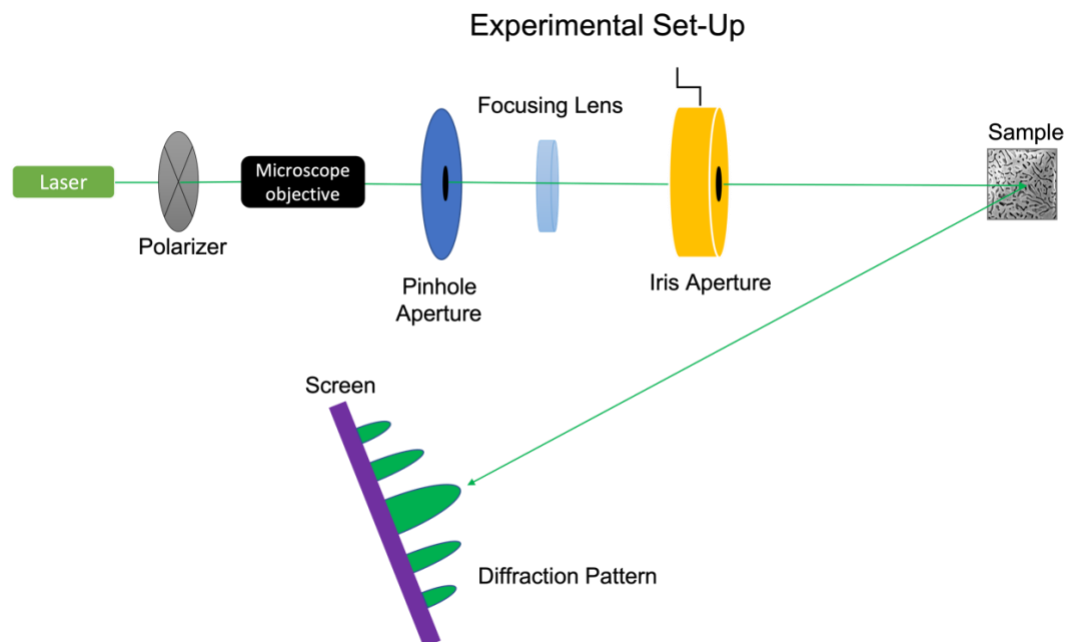


Figure 5.1 Experimental setup used for the diffraction studies.

Far-field diffraction measurements were performed on MP and AMP structures using the experimental setup in Figure 5.1. The sample and the optics were mounted on a linear optical track to facilitate adjustments and ease of alignment. The diffraction patterns were generated using a 30 mW, 532 nm diode laser. The beam was passed through a Glan-Thompson polarizer model 10GT04 from Newport, then focused with a 10x objective onto a 0.7 mm diameter aperture and then focused onto individual MP and IMP structures with a convex lens. An iris was placed between the lens and the sample to mitigate aberrations. The polarizer was used to modulate the intensity of the laser beam. The reflected light was imaged on a screen approximately 125 cm from the sample. With this optical setup, the beam's spot size at the sample was calculated to be $\sim 53 \mu\text{m}$. The sample was mounted on an optical stage with XYZ motion and rotation about the focal plane. The distance from the sample to the screen was kept fixed at 125 cm for all measurements. This was done to ensure that the diffraction patterns relative size was consistent between both types of meso-structures. A hole was cut into the center

of the screen to allow the zero-order light to pass through, thereby mitigating the overloading of the digital camera used to capture the diffraction images.

Section 3: Results

The geometries and surface morphologies of the MP and IMP are critical to evaluating their far diffraction patterns and understanding the differences between said patterns. While a sample will have many meso-structures across the surface, for this study, the choice of structures was restricted to MP and AMP with similar shapes and on the same order of size. The Au MP and IMP are easily located on the sample by looking for large circular patterns on the order of hundreds of microns. These patterns correspond to regions where MP and IMP have scavenged the Au during their formation. We refer to these regions as denuded zones. The SEM image in panel (a) of Figure 5.2 is an example of a denuded zone centered around the MP used in this study. Note that there are smaller denuded sites within the larger zone that correspond to smaller Au meso-structures that co-formed with the large MP. Figure 5.2(b) is an SEM image of the prominent MP in the center of the denuded zone in Figure 5.2(a). Note the unique topography of channels and plateaus on the surface of the MP, which arises from phase separation of the gold-silicon eutectic during the cooldown period of their formation, where Si scavenged from the substrate is reincorporated into the substrate [138] [62], [103], [142]–[144]. The square base of the MP and IMP is due to preferential etching along the [100], $[\bar{1}00]$, [010], and $[0\bar{1}0]$ of Si(100) substrate [17]–[20].

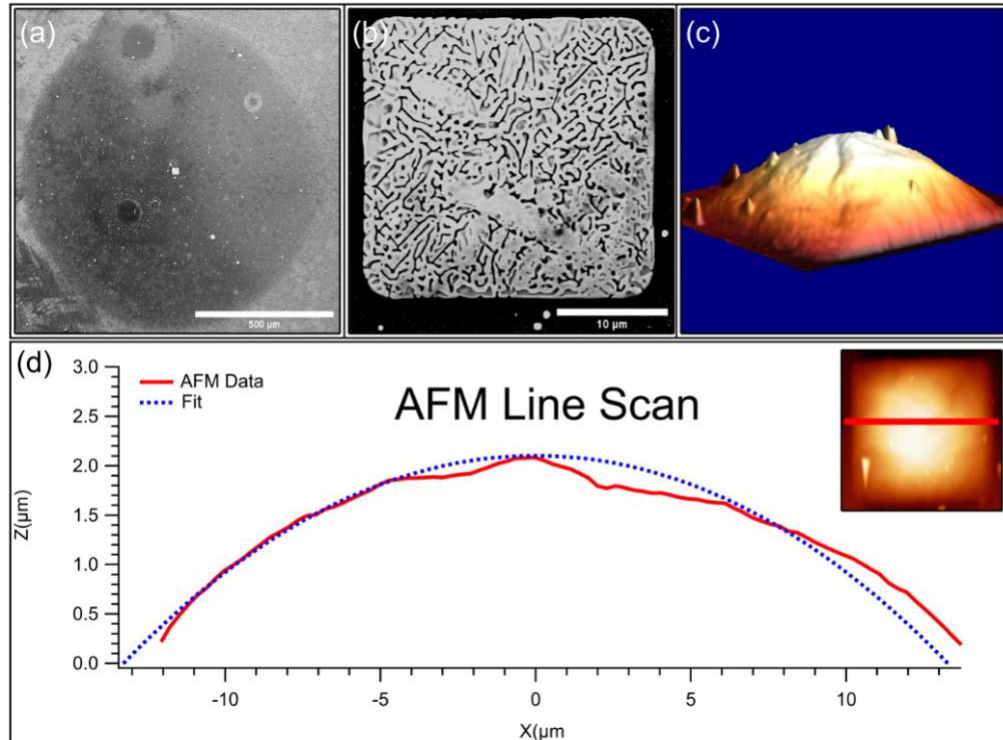


Figure 5.2 (a) A SEM micrograph of the denuded zone with a Au mesopyramid at the center. (b) A high magnification SEM micrograph of the mesopyramid located in the center of the denuded zone in (a). (c) 3D rendering of the AFM imaging of the mesopyramid in (b). (d) The AFM line scan profile of the mesopyramid in (b), where the inset shows the location of the line scan on the mesopyramid. The dashed blue line is the calculated radius of curvature for the MP.

Figure 5.2(c) is a 3D rendering of the AFM profile of the MP in Fig. 5.2(b) and Fig. 5.2(d) is a representative line scan. The scale of the vertical axis is approximately 1/6 of the horizontal axis in order to accentuate the curvature of the MP. The line scan profile in Fig. 5.2(d) can be approximated with a radius of curvature of 43 μm (blue dotted line) Treating the MP as a convex spherical mirror, its focal point is approximately half the radius of curvature or 23 μm . The treatment of the MP as a convex spherical mirror will be discussed in the next section.

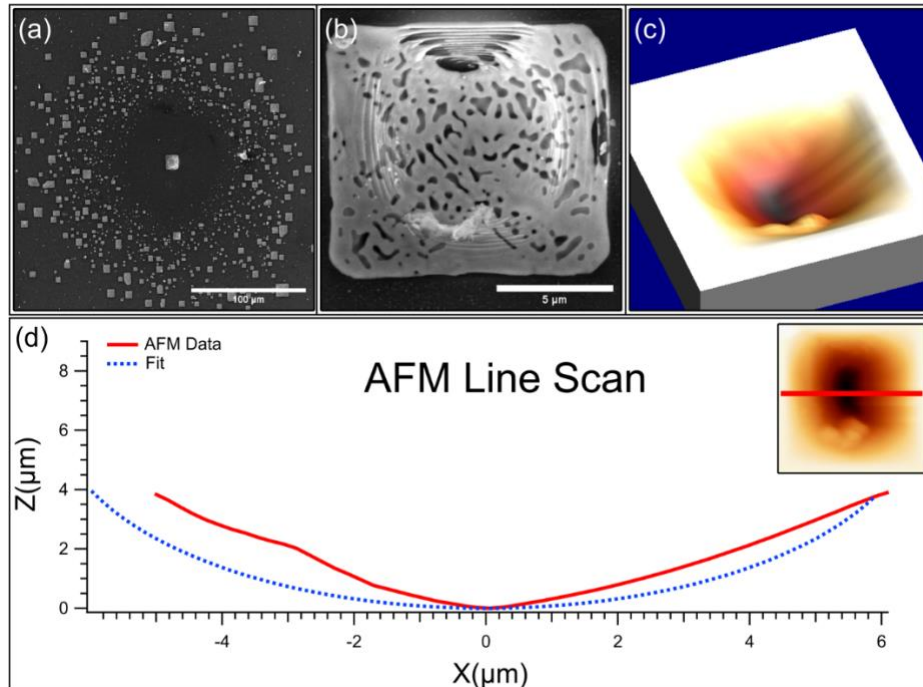


Figure 5.3 (a) An SEM image of the denuded zone with a Au inverse mesopyramid at the center. (b) A high magnification SEM of the Au inverse mesopyramid located in the center of the denuded zone in (a). (c) 3D rendering of the AFM data of the inverse mesopyramid in (b). (d) The AFM line scan profile of the inverse mesopyramid in (b), where the inset shows the location of the line scan on the inverse mesopyramid. The fit line is the calculated radius of curvature for the inverse mesopyramid.

The analysis of the Au inverse mesopyramid is summarized in Figure 5.3(a). To the best of our knowledge, the clustering of smaller meso-structures (MP and/or IMP) outside of the perimeter of the denuded zone is unrelated to the formation of IMP since similar clustering has been observed around MP. The SEM in Figure 5.3(b) of the IMP reveals the presence of a significant depression slight offset from the center of the structure concomitant with surface ripples radiating outward from the center of the depression. This unique topography results from phase separation of the AuSi eutectic during cooldown, where Si has once again been reincorporated into the Si substrate. An IMP is an MP that collapsed in on itself, creating the

concave meso-structures or concave micromirror. While all the meso-structures have a sponge-like interior scaffolding that forms during cooldown, concomitant phase separation, IMP have less structural integrity. We hypothesize that large voids form in the Si substrate underneath the MP during the eutectic formation and do not refill with Si during phase separation; thus, a large fraction of the MP is unsupported by the substrate and prone to collapsing. We suspect that the ripples form either because the surface of the MP is larger than the final surface of the IMP or only part of the MP collapses or a combination of both. Figure 5.2(c) is a 3D rendering of the AFM data of the IMP in Figure 5.3(b). The line scan profile in Figure 5.3(d) is through the center of the IMP, where once again, the vertical scale has been accentuated. The IMP has a negative radius of curvature of 6.5 μm . Similarly, the blue dotted line is the fit of our approximation of the radius of curvature to the physical data. Treating the IMP as a concave spherical mirror, the radius of curvature corresponds to an approximate focal length of 3.25 μm . The difference in the sign of the radius of curvature between the MP and IMP impacts their corresponding diffraction patterns.

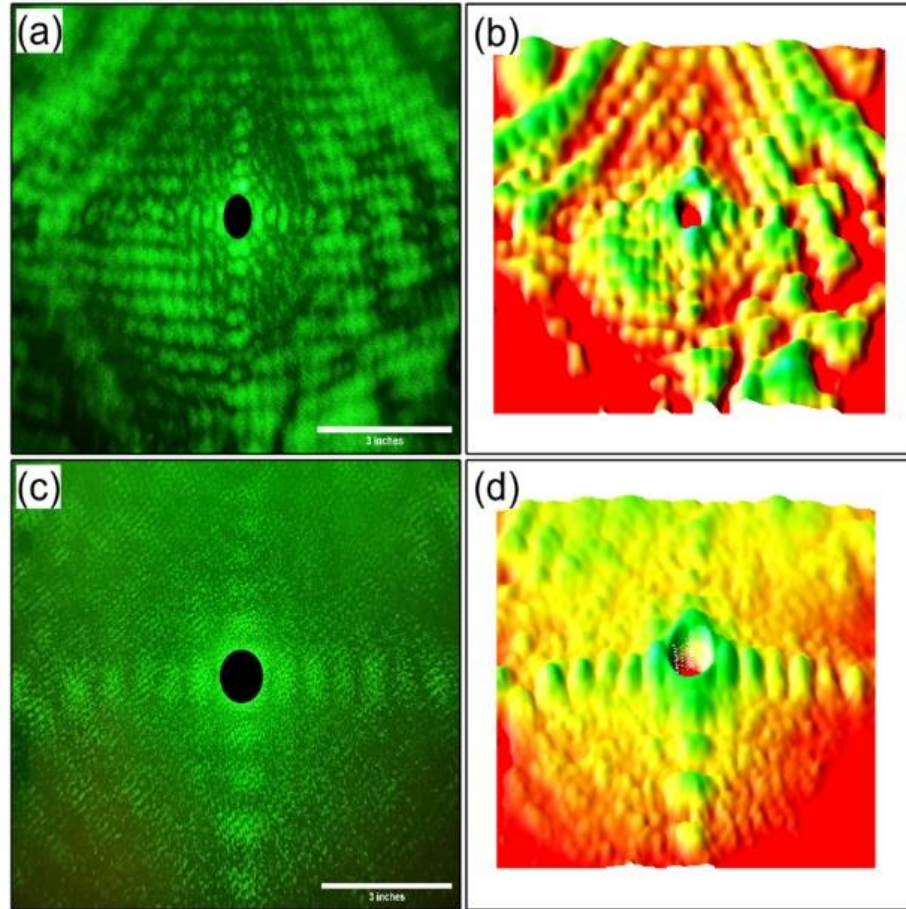


Figure 5.4 (a) The diffraction pattern produced by the mesopyramid in Figure 5.2(b) and (b) is a 3D thermal map of the diffraction pattern. (c) The diffraction pattern produced by IMP in Figure 5.3(b) and (d) is a 3D thermal map of the diffraction pattern.

The far-field diffraction patterns produced by the MP and IMP are displayed in Figures 5.4(a) and (c), along with corresponding 3D thermal maps (Figures 5.4(b) and (d)), respectively. The 3D thermal maps illustrate the differences of intensities throughout the pattern. Both meso-structures produce a Fraunhofer diffraction patterns typical of a square aperture [21]–[25]. It is worth noting that the distance from the pinhole to the sample and the sample to the screen are the same for both measurements. There is a direct correlation between the morphology of the meso-

structures, specifically, the eccentricities and signs of their curvatures, meso-structures on the finer details of their respective Fraunhofer diffraction patterns.

Section 4: Discussion

The formation of the Fraunhofer diffraction pattern with a square aperture is a well-documented optical phenomenon that is easily modeled [154]–[156]. The fact that light reflected by the MP and IMP produces a Fraunhofer diffraction pattern demonstrates that they can be modeled as an aperture through which light passes, i.e., a square array of emitters. The far-field approximation for diffraction can be applied here because the emitter is on the order of tens of microns, and the screen is over 100 cm away [157], i.e. the observation point, \mathbf{R} (screen in Fig. 1), is much larger than the dimensions of the aperture (\mathbf{r}), where the center of the aperture is the origin, one can perform a binomial expansion about (r/R) . In addition, one assumes that the \mathbf{k} -vector is constant. This allows one to write the electric field of the light passing through a square aperture at a point P on the screen as:

$$E(P) = \frac{\varepsilon_A e^{i(\mathbf{kR}-\omega t)}}{R} \iint e^{ik(Yy-Xx)/R} dydx, \quad \{\text{Eq.1}\}$$

where the integral is over the area of the aperture, represented by x and y , where X and Y represent the position on the screen. The integral has the following solution:

$$EP) = \frac{A\varepsilon_A e^{i(\mathbf{kR}-\omega t)}}{R} \frac{\sin \alpha'}{\alpha} \frac{\sin \beta'}{\beta}, \text{ where } \alpha = \frac{kbY}{aR} \text{ and } \beta = \frac{kbX}{aR}, \quad \{\text{Eq.2}\}$$

where a and b are the dimensions of the aperture. The modulus squared of Eq. 2 is the intensity, $I(P)$, as a function of position on the screen:

$$I(P) \sim \left(\frac{\sin \alpha'}{\alpha} \right)^2 \left(\frac{\sin \beta'}{\beta} \right)^2 \quad \{\text{Eq.3}\}.$$

The diffraction pattern for a square aperture using Eq. 3 is displayed in Figure 5.5. The results of the model are in excellent agreement with the diffraction patterns of both types of meso-structures (Figure 5.4). Because Eq. 3 does not account for the rounded corners of the MP and IMP, it cannot replicate the diagonal bands observed in Figure 5. 4 [153]. Note that the diagonal features are pronounced for the MP and less so for the IMP, which we will now address.

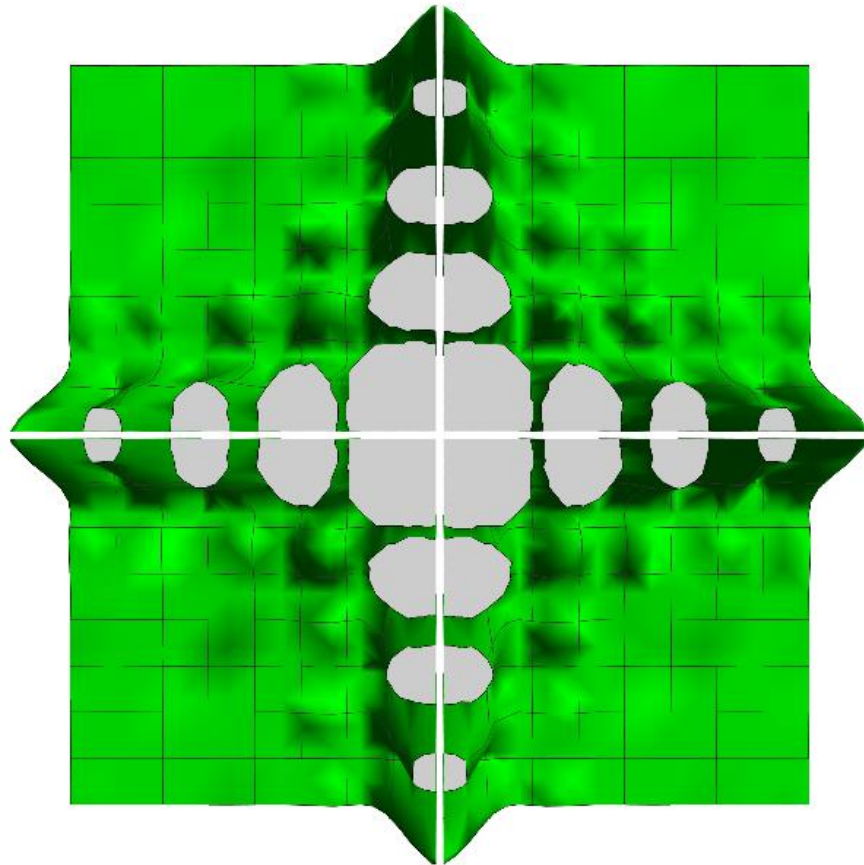


Figure 5.5 A simulation of the Fraunhofer diffraction pattern using Equation 3.

From the observer's perspective (the screen), the mesopyramids are a square aperture constructed with concave and convex lenses. Consequently, the Fraunhofer far field approximation fails to capture effects associated with the positive and negative curvatures of the

MP and IMP, respectively. Accounting for this, the MP has properties of a convex mirror and the IMP that of a concave mirror. Therefore, the MP should minify the diffraction image relative to a planar square aperture. Conversely, the IMP will magnify or minify the diffraction pattern relative to a planar square aperture depending on the object's position, i.e., the pinhole in Figure 5.1, relative to the focal point of the IMP. The ray traces for the convex MP and the concave IMP mirrors as a function of the position of an object relative to their focal points are illustrated in Figure 5.6. The focal points of the MP and IMP are calculated using their radii of curvatures using the mirror formula:

$$\frac{1}{s_o} + \frac{1}{s_i} = \pm \frac{1}{f'} \quad \{\text{Eq.4}\}$$

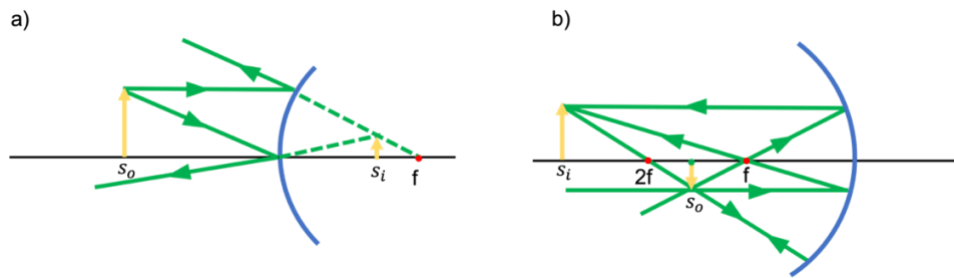


Figure 5.6 The light ray trace of (a) a convex mirror (mesopyramid) and (b) a concave mirror (inverse mesopyramid).

where s_o is the position of the object, s_i is the position of the image, R is the radius of curvature of the mirror, and $f (= -R/2)$ is the focal length of the mirror. R is positive (negative) for a convex (concave) mirror. The concavity, in conjunction with the location of the object relative to the mirror's focal point, determines whether the image (diffraction pattern) is magnified or minified. The MP (convex mirror) will always produce a minified image relative to the object. Note that the image formed by the MP is virtual, i.e., on the right-hand side of the position pole of the mirror in Figure 5.6(a). In the case of the IMP, the object's location relative to its focal point will

determine whether the image is magnified or minified. For magnification by the IMP (concave mirror), the following conditions apply for the position of the object and image:

$$f < s_o < 2f, \quad \{\text{Eq.5}\}$$

$$\infty > s_i > 2f. \quad \{\text{Eq.6}\}$$

Once again, the size and position of the screen remained fix for the diffraction experiments.

Therefore, the differences between them are due to differences in magnifications produced by the MP and IMP. Given the large radius of curvature of 43 mm for the MP, the diffraction image in Figure 5.4(a) is only minified slightly, i.e., it is, effectively, a nondivergent image from a planar mirror. Furthermore, we have concluded that the diffraction image produced by the IMP in Figure 5.4(c) is magnified relative to Figure 5.4(a). Ergo, Figure 5.4(c) is a magnified image of the inner Fraunhofer pattern in Figure 5.4(a). So, not only do the MP and IMP behave as square apertures that produce Fraunhofer diffraction patterns, they also act as lenses that magnify or minify the pattern. For the ratio of the IMP to MP, we calculate the relative magnification to be 2.75.

Section 5: Conclusion

The far-field reflective properties of Au mesoscale mirrors naturally formed during the phase separation of AuSi eutectic have been explored. The convex gold meso-structures have a fourfold symmetry reminiscent of a rounded pyramid, ergo, mesopyramid (MP), while the concave structures have a nearly equivalent inverse geometry, ergo, inverse mesopyramid (IMP). Both meso-structures produce a far-field Fraunhofer diffraction pattern and, therefore, meso-structures have been modeled as square apertures. The MP diffraction pattern has diagonal lines outside the Fraunhofer pattern that are attributed to its rounded corners. Similar but fainter diagonal lines are also observed for the IMP. Atomic force microscopy analysis of the shape of the MP and IMP reveals that they have radii of curvatures of 43 μm and 6.5 μm and can be viewed

as square-shaped convex and concave mirrors, respectively. The large radius of curvature of the MP indicates that it will produce a slightly minified diffraction pattern relative to a planar square mirror. However, the smaller radius of curvature of the IMP will create a magnified image relative to the MP. Consequently, the diffraction pattern produced by the IMP is a magnified image of the inner Fraunhofer pattern of the MP, sans diagonal lines. Therefore, the diffraction pattern produced by reflecting light off the two meso-structures is that of a square aperture, and the curvatures of their surfaces enables them to magnify or minify the resulting Fraunhofer diffraction pattern. In other words, they are mirrors that behave like square apertures constructed with a convex and concave lens. These naturally occurring MP and IMP may be useful in constructing nonlinear and meta-optics that combine plasmonic characteristics with their far-field optical properties. Surface enhanced Raman scattering comes to mind as an immediate application of these meso-structures. Furthermore, MP and IMPS might prove useful for optical encryption because no two meso-structures are the same.

CHAPTER VI

SURFACE PLASMON POLARITON THEORY

Section 1: Introduction

In this chapter I will discuss the basic governing principles of surface plasmon polaritons (SPP) in the context of its application to my research. The decision to devote a stand-alone chapter to this subject was due, in part, to the fact that detection of the SPP on the surface of MP and IMP was the primary motivation for my research. Although there seems to be a wide range of interpretations of SPP data, there is, however, a consensus on where to start when discussing the phenomena. A semi-infinite conductor/dielectric continuous interface is the standard materials combination and geometry for developing the theoretical model of SPP coupling to light, propagation and scattering and, therefore, the approach I take. I will then move to a different geometry to germane to my experimental setup. The intent of the discussion is to provide a theoretical foundation for interpreting the experimental results presented in the next chapter and by no means a complete review of the theory of SPP.

A surface plasmon polariton is an electromagnetic excitation that propagates at the interface between a conductor and dielectric. This phenomenon is confined to the surface or interface because the electric field normal to the surface is theoretically/mathematically designed to exponentially decay into the dielectric the metal, i.e. in directions normal to the metal/dielectric interface.

Begin An SPP is excited or launched in response to incident photons coupling with the conduction electrons at the surface of the metal. It should be noted that the energy prorogates as a wave thought the medium of these electrons and not the electrons themselves. Therefore, it is not a free surface current. The confinement of the magnetic field of the SPP makes them very sensitive to changes in surface topography of the surface. To embark on a theoretical model of SPP, I will begin with a brief discussion of Maxwells equations. This derivation comes from a Stefan et. Al [26]. I refer the reader to this text for a more detailed explanation.

Section 2: Maxwell's Equations and the Wave Equation

Maxwell's equations are:

$$\nabla \cdot \mathbf{D} = \rho_{ext} \{eq. 1\}$$

$$\nabla \cdot \mathbf{B} = 0 \{eq. 2\}$$

$$\nabla \times \mathbf{E} = -\frac{\partial \mathbf{B}}{\partial t} \{eq. 3\}$$

$$\nabla \times \mathbf{H} = J_{ext} + \frac{\partial \mathbf{D}}{\partial t} \{eq. 4\}$$

where, \mathbf{D} is the dielectric displacement, \mathbf{E} is the electric field, \mathbf{H} is the magnetic field and \mathbf{B} is the magnetic induction. In the context of SPP, it is assumed that there are no external charges or current densities i.e. ρ_{ext} and J_{ext} are both equal to zero. That is there is no external stimuli of the SPP system once the wave has been launched. Taking the curl of equation 3 and then inserting equation 4 into it, we arrive at the following relationship:

$$\nabla \times \nabla \times \mathbf{E} = -\mu_o \frac{\partial^2 \mathbf{D}}{\partial t^2} \{eq. 5\},$$

from which we can derive the wave equation for electromagnetic radiation. With the application of a few dot and cross product identities equation 5 simplifies to:

$$\nabla^2 \mathbf{E} - \frac{\varepsilon}{c^2} \frac{\partial^2 \mathbf{E}}{\partial t^2} = 0 \text{ \{eq. 6\}},$$

the easily recognizable wave equation. Next, we assume that the electric field is a plane wave of the form $\mathbf{E}(\mathbf{r}, t) = E(\mathbf{r})e^{-i\omega t}$. Plugging this expression for the electric field into equation 6 and arrive at Helmholtz' equation:

$$\nabla^2 \mathbf{E} + k_0^2 \varepsilon \mathbf{E} = 0 \text{ \{eq. 7\}},$$

where we define $k_0^2 = \frac{\omega}{c}$, ω the angular frequency and c is the speed of light in vacuum, and ε is the dielectric permittivity or relative permittivity. We are now ready to apply the define our coordinate space to work out the details of SPP.

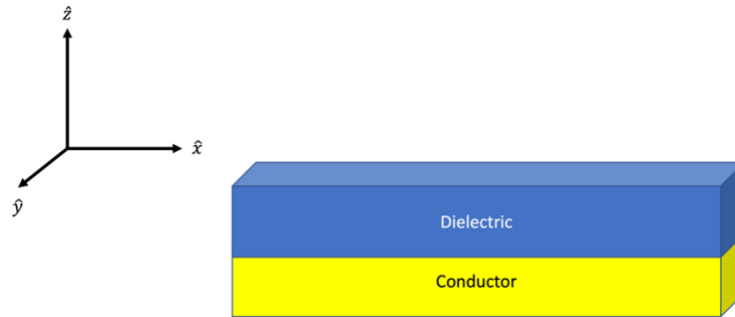


Figure 6.1 Configuration of conductor and dielectric with defined axis.

We define the direction of propagation of the SPP to be parallel to the interface between the dielectric and the conductor, i.e., in the x -direction at $z = 0$. See Figure 6.1. With this in mind, we revisit equation 7 with the restriction that the wave is confined to the interface and propagates in the x -direction, where the in-plane wave vector is defined as $\beta = k_x$. The electric field defined as $\mathbf{E}(\mathbf{x}, \mathbf{y}, \mathbf{z}) = \mathbf{E}(\mathbf{z})e^{-i\beta x}$, where the amplitude is only dependent on the z -direction because the film is assumed to be continuous and infinite. Plugging this into equation 7, we calculate:

$$\frac{\partial^2 E(z)}{\partial z^2} + (k_0^2 - \beta^2)E = 0 \text{ \{eq. 8\}}$$

We can apply the same methods to come up with expressions for the magnetic field, where $\mathbf{B} = \mu\mu_0\mathbf{H}$. We are now ready to look at the electromagnetic modes that satisfy the boundary conditions. Considering a harmonic time dependence $\frac{\partial}{\partial t} = -i\omega$ and a propagation along the x-direction $\frac{\partial}{\partial x} = i\beta$. Also, because of the homogeneity in the y-direction, all derivatives of $\frac{\partial}{\partial y} = 0$.

Using Maxwell's equations 1-4, we arrive at a system of equations:

$$\frac{\partial E_y}{\partial z} = -i\omega\mu_0 H_x \text{ \{eq. 9\}}$$

$$\frac{\partial E_z}{\partial z} - i\beta E_z = i\omega\mu_0 H_y \text{ \{eq. 10\}}$$

$$i\beta E_y = i\omega\mu_0 H_z \text{ \{eq. 11\}}$$

$$\frac{\partial H_y}{\partial z} = i\omega\varepsilon_0\varepsilon E_x \text{ \{eq. 12\}}$$

$$\frac{\partial H_x}{\partial z} - i\beta H_z = -i\omega\varepsilon_0\varepsilon E_y \text{ \{eq. 13\}}$$

$$i\beta H_y = -i\omega\varepsilon_0\varepsilon E_z \text{ \{eq. 14\}}$$

For this system of equations there are two sets of self-consistent solutions with different polarizations. If the magnetic field is perpendicular to the direction of propagation, the wave is defined as a transverse magnetic wave or TM wave with the following components of the electric and magnetic field: E_x , E_z and H_y . If the electric field is perpendicular to the direction of propagation, the wave is defined as a transverse electric wave or TE wave with the following components of the electric and magnetic field: H_x , H_z and E_y . For a TM wave, eqs. 10-14 reduce to:

$$E_x = -i \frac{1}{\omega \epsilon_0 \epsilon} \frac{\partial H_y}{\partial z} \{eq. 15\}$$

$$E_z = -\frac{\beta}{\omega \epsilon_0 \epsilon} H_y \{eq. 16\}$$

The TM wave equation is now defined as,

$$\frac{\partial^2 H_y}{\partial z^2} + (k_0^2 \epsilon - \beta^2) H_y = 0 \{eq. 18\}.$$

For TE wave, eqs. 10-14 reduce to:

$$H_x = i \frac{1}{\omega \mu_0} \frac{\partial E_y}{\partial z} \{eq. 19\}$$

$$H_z = \frac{\beta}{\omega \mu_0} E_y \{eq. 20\}$$

The TE wave equation is defined as,

$$\frac{\partial^2 E_y}{\partial z^2} + (k_0^2 \epsilon - \beta^2) E_y = 0 \{eq. 21\}.$$

We now have the necessary relationships to describe SPP behavior at an interface. Specifically, we can address define the dispersion relationships governing SPP excitation. This will be an important factor considering the topography of the mesostructures. This has implications on the angle of incident of incoming light used to excite SPP and the effect of surface inhomogeneities on the excitation of SPP.

Section 3: SPP at the Dielectric Conductor Interface and the Dispersion Relation

When considering a propagating wave at the interface of the dielectric and a conductor, special attention must be paid to the dielectric permittivity. For $z > 0$, i.e., the dielectric, the dielectric permittivity, ϵ_2 , must be real and positive, For $z < 0$, i.e., the metal, the real part of the dielectric permittivity, ϵ_1 , must be negative. These conditions are fulfilled for ω below the bulk plasma frequencies. At this point we can examine the TM solutions. For $z > 0$,

$$H_y(z) = A_2 e^{i\beta x} e^{-k_2 z} \{eq. 22\}$$

$$E_x(z) = iA_2 \frac{1}{\omega \epsilon_0 \epsilon_2} k_2 e^{i\beta x} e^{-k_2 z} \{eq. 23\}$$

$$E_z(z) = -A_1 \frac{\beta}{\omega \epsilon_0 \epsilon_2} e^{i\beta x} e^{-k_2 z} \{eq. 24\}.$$

For $z < 0$

$$H_y(z) = A_1 e^{i\beta x} e^{k_1 z} \{eq. 25\}$$

$$E_x(z) = -iA_1 \frac{1}{\omega \epsilon_0 \epsilon_1} k_1 e^{i\beta x} e^{k_1 z} \{eq. 26\}$$

$$E_z(z) = -A_1 \frac{\beta}{\omega \epsilon_0 \epsilon_1} e^{i\beta x} e^{k_1 z} \{eq. 27\}.$$

Defining $k_i \equiv k_{z,i}$ ($i = 1,2$) as the perpendicular component of the wave vector to the interface.

The reciprocals of the k_i 's are the decay lengths or penetration depths of the SPP into the two media. Continuity of H_y and $\epsilon_i E_z$ at the interface requires $A_1 = A_2$ or the ratio of the wave vectors is equal to the minus the ratio of the dielectric permittivities. By requiring that the sign of the real part of the dielectric permittivity of the conductor be negative for the conductor and

positive for the dielectric, the surface wave can only exist at the interface. The requirement that \mathbf{H}_y be compatible with equation 18 and $\frac{k_2}{k_1} = -\frac{\epsilon_2}{\epsilon_1}$, we arrive at the relationships for k_1 and k_2 :

$$k_1^2 = \beta^2 - k_0^2 \epsilon_1 \text{ \{eq. 28\}}$$

$$k_2^2 = \beta^2 - k_0^2 \epsilon_2 \text{ \{eq. 29\}}$$

Solving this system of equations, we arrive that the dispersion relation of a SPP at the interface between a conductor and a dielectric.

$$\beta = k_0 \sqrt{\frac{\epsilon_1 \epsilon_2}{\epsilon_1 + \epsilon_2}}.$$

It is worth noting the above derivation is for a TM wave and not TE. This is due to the fact that for $z < 0$, the condition of continuity leads to $A_1(k_1 + k_2) = 0$. Confinement at the surface requires that $A_1 = A_2 = 0$. This means that transverse electric waves cannot propagate along the interface, i.e. SPP can only be transverse magnetic waves.

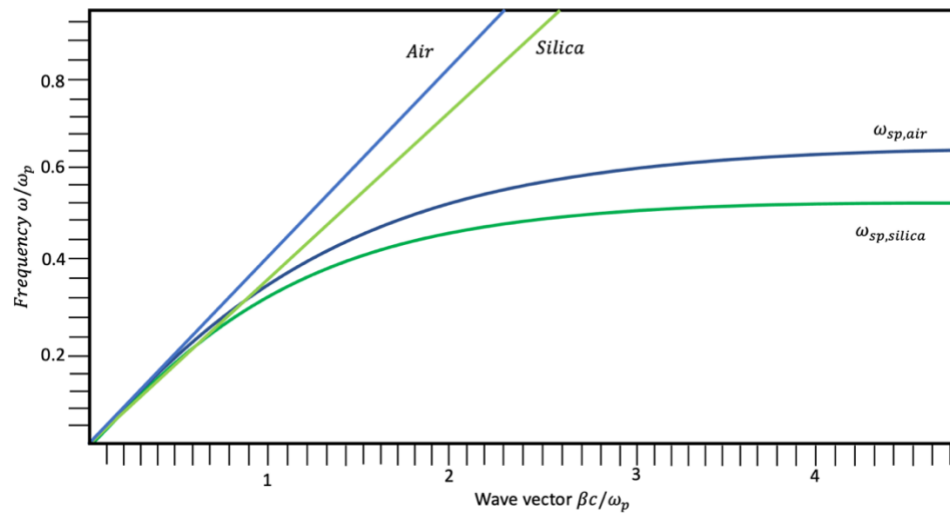


Figure 6.2 Dispersion curve of a Drude metal and air.

The dispersion curve in figure 6.2 is for a metal/air interface. Because the SPP is confined to the interface between these two materials, the dispersion curve lies to the right of the light line for both materials. Therefore, you need phase matching in order to couple and scatter SPP with this configuration. Phase matching can be accomplished with a grating or a prism. An alternative way of looking at the problem is from the point of view of conservation of wave vector momentum at the interface. To effectively launch SPP, the light must be incident at a resonance angle and have a specific polarization. To overcome the first requirement, we change our semi-infinite thin film to a defect ensemble. In doing so we change the nature of the geometry of the light line and the SPP dispersion curve. SPP can be excited at points where the light line crosses the SPP dispersion curve i.e. regions of the SPP dispersion to the left of the light line. We will touch on SPP coupling and scattering methods that more closely mirror my experiments in Chapter 6.

Section 4: Mechanisms for SPP Coupling and Launching

We begin by addressing the condition required to couple the energy of a photon to the sea of electrons at a smooth and continuous surface of a conductor. This discussion will center around the description of coupling and scattering, as presented by Zayats et al. (2004)[1]. I refer the reader to Ref. [1] for an in-depth review of the details. To effectively couple light to SPP, the frequency of the SPP and incident light must be equal. Given the broad range nature of the light source in my experimental setup, this condition is easily met. The frequencies of light that are not at the correct frequency is simply reflected/scattered. Another prerequisite is that the component of the wave vector of the light parallel to the surface must equal of the wave vector of the SPP, i.e., conservation of momentum parallel to the surface.

This phase matching condition can be stated as follows:

$$\sqrt{\epsilon_1} \frac{\omega}{c} \sin \theta = \frac{\omega}{c} \sqrt{\frac{\epsilon_1 \epsilon(\omega)}{\epsilon(\omega) + \epsilon_1}} \quad \{eq. 30\}$$

Where ϵ_1 is the dielectric permittivity of air and $\epsilon(\omega)$ is the frequency dependent dielectric of a metal. The angle θ is the angle of incident of the light. For this reason, SPP cannot be launch by illuminating the metal at random angles. This second condition is not easily overcome and requires special consideration. There two most common approaches used to ensure wave vector conservation at the interface. The first is the Kretschmann method where a prism is used to deliver the light at the correct angle for launching SPP[158]–[162]. The other approach is to use a grating that takes advantage of diffraction effects. Alternatively, one can work with a discontinuous conducting film with a broader range of SPP k-vectors. Components of this diffracted light whose wave vector coincide with the SPP wave vector will launch SPP[163]–[168]. This is a much less efficient method of couple. Conventional illumination of a rough surface can launch SPP but there will however be a lot of reflected light and the signal may be washed out in the noise. For this reason, a special experimental setup is needed to detect the signal due to SPP. With the use of a monochromator with sub nanometer resolution and a photo multiplier tube working with a lock-in analyzer one can detect these signals as will be discussed in the next chapter.

CHAPTER VII

SURFACE PLASMON POLARITONS ABSORPTION AND SCATTERING FACILITATED BY NANOSCALED TOPOGRAPHY OF MESOPYRAMIDS AND INVERSE MESOPYRAMIDS

Section 1: Introduction

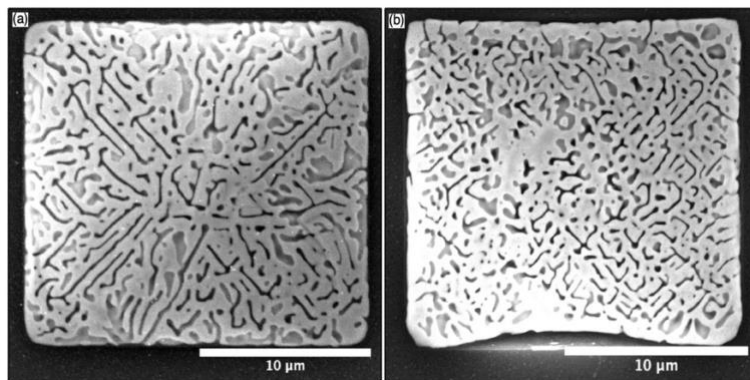


Figure 7.1 Scanning electron micrographs of (a) a mesopyramid and (b) inverse mesopyramid grown Si[100] wafer.

In this chapter I present the recent results of my work on the excitation of surface plasmon polaritons (SPP) on the surface of MP and IMP, see Figure 7.1, where once again it is the excitation of the conduction electrons at the conductor/dielectric interface produce a propagating transverse wave [27], [169]–[172]. The results presented herein represent where we are at this point in the project.

Therefore, the interpretation of the results remains open ended and the subject of continued research. It is meant to provide insight into our working hypothesis to explain the observed phenomena. I believe the results are scientifically significant because materials that are SPP active are at the forefront of optoelectronic device development [27]–[31].

Section 2: Experimental Setup:

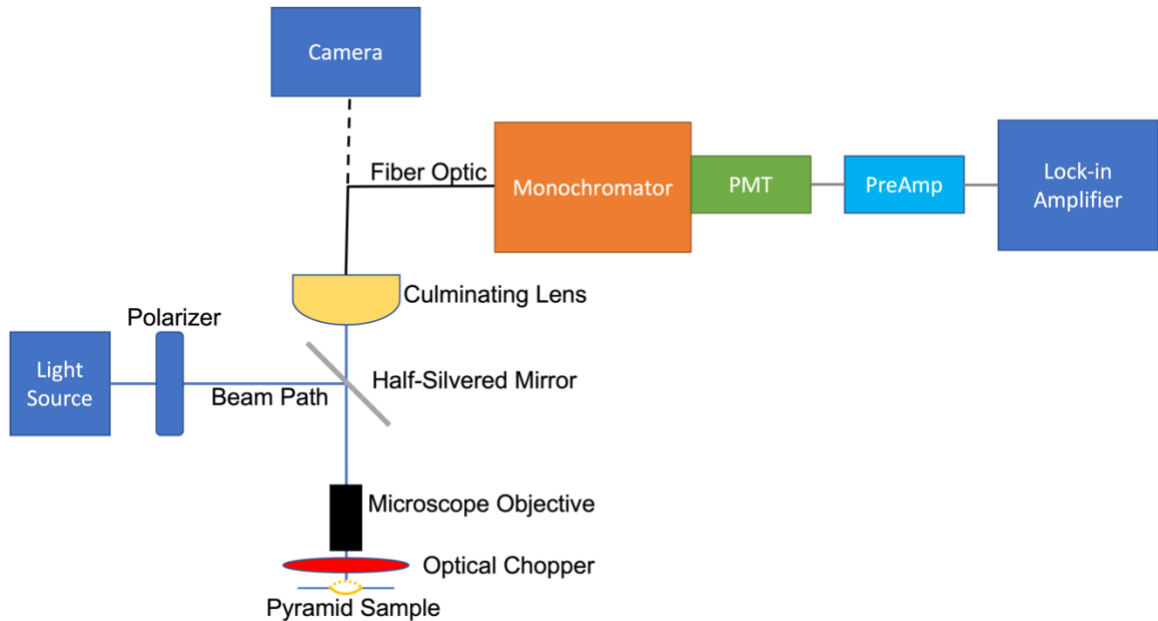


Figure 7.2 Experimental Setup

Figure 7.2 is a schematic of the experimental setup used for imaging surface plasmon polaritons on the surfaces of the MP and IMP. The same light source and detection (camera and/or monochromator) was used for all of the experiments. An Olympus BX51 microscope equipped with a polarized non-coherent white light source and a half-silvered mirror (inside the microscope) and either an oil immersion lens or a long working distance objective was used to illuminate as single MP or IMP. The intensity of the light intensity was kept fixed for all spectra acquired for a given MP or IMP. An Olympus Ach N 100x Oil Immersion lens with IMMOIL-F30CC type immersion oil was used to acquire images of SPP activity on the surface of a MP,

while an Olympus SLMPIan N 100x long working distance objective was used to acquire images and optical reflectivity spectra of SPP activity on the surface of the IMP. Optical reflectivity spectra acquired through the top of the microscope using a custom-built culminating lens that focused the light onto an optical fiber. The output of the optical fiber went to an Oriel Instruments Newport monochromator CS260-USB-2-MC-D. The monochromator was stepped through 400 nm to 800 nm in increments of 1 nm with a 3000 ms dwell time. A ThorLabs PMTSS photomultiplier tube (PMT) with a ThorLabs Tia60 preamplifier placed at the output of the monochromator served as the light detector. A Stanford Research 830 Lock-in Amplifier was used to increase the signal to noise of the output of the PMT. In order to use lock-in detection, an optical chopper was placed between the sample and the objective. Due to space constraints, lock-in detection was only used in conjunction with the long working distance objective. To ensure the phenomena we are reporting on was due to SPP and not an artifact of our setup, we used multiple types of objective lenses. For example, chromatic aberrations were minimized by using an oil immersion lens, while birefringent diffraction was avoided by using a long working distance objective. Note that by rotating the polarized light source in increments of 90°, we were able to show that phenomena we observed for the IMP tracked with polarization of the light. This will be explained in more detail below. Both MP and IMP produce optical responses that are consistent with the excitation and scattering of SPP. I will demonstrate that the geometry of the surfaces of the mesostructures, i.e. MP or IMP, plays an important role in how the light couples to SPP of Au.

Section 3: Results

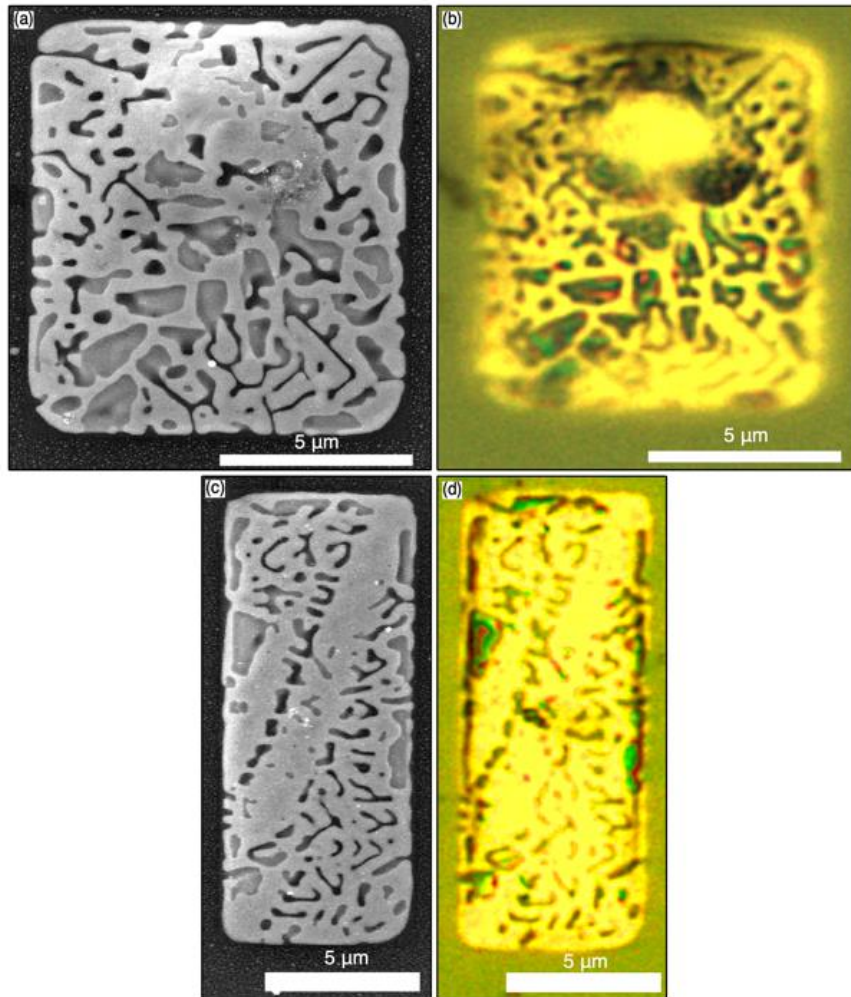


Figure 7.3 (a) An SEM micrograph of a MP and (b) the optical microscope image of the MP in (a) using white light and with oil immersion. (c) An SEM micrograph of a MP (d) the optical microscope image of the MP in (c) using white light and with oil immersion.

The initial attempts to identifying SPP activity on the surface of the mesopyramids are presented in Figure 7.3. The SEM micrographs in panels (a) and (c) show the details of the surface morphology of the MPs, while panels (b) and (d) are the corresponding oil immersion optical images obtained with a polarized white light source. The SEM micrographs were obtained with a FEI Quanta 600 ESEM with a beam energy of 5 keV. The corresponding optical images

obtained with a 100x oil immersion objective. This objective was chosen to provide the resolution necessary to resolve the cavities on the surface of the MP. Areas of red and green bright spots clearly correspond to the floors of the cavities. These red and green colors are due the SPP launching and subsequent scattering of the polarized light incident on the surface of the cavities. The oil immersion objective has a large numerical aperture of 1.25. The calculated range of angle of acceptance for our this set up is $\sim 75^\circ$. This is extremely important for launching SPP and will be discussed in more detail in the next section.

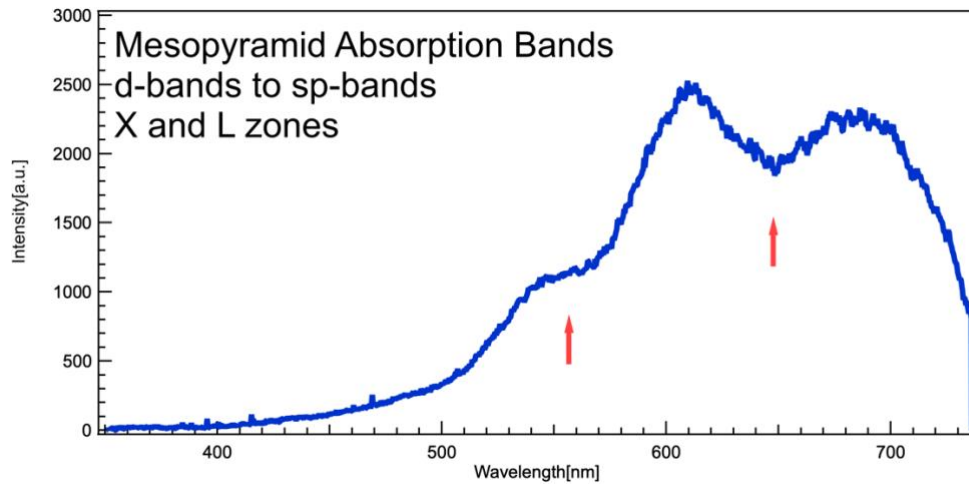


Figure 7.4 Reflectivity spectrum using a white light source of a single MP, where the arrows indicate SPP absorption bands at roughly 550nm and 650nm.

A representative reflectivity spectrum for a single MP using a p-polarized white light source is presented in Figure 7.4. Note the two large absorption bands in the spectrum at roughly 550nm and 650nm. These two absorption bands correspond to electron transitions from the Au d-band near the Fermi level to unoccupied sp-bands. The absorption bands correspond to the wavelengths of the red and green hotspots in Figure 7.3. Therefore, the hotspots are assigned to SPP scattering, where the wavelengths of the SPP absorption bands are also the wavelengths of light emission when SPP scatter and radiate light. In other words, the wavelengths that launch

SPP are also the wavelengths that are emitted. It merits restating that when observing the SPP behavior in the far field, the results represent a statistical average of the most prominent behaviors observed in the system. These results show in micrograph and spectrograph direct evidence of SPP launching and scattering at the MP.

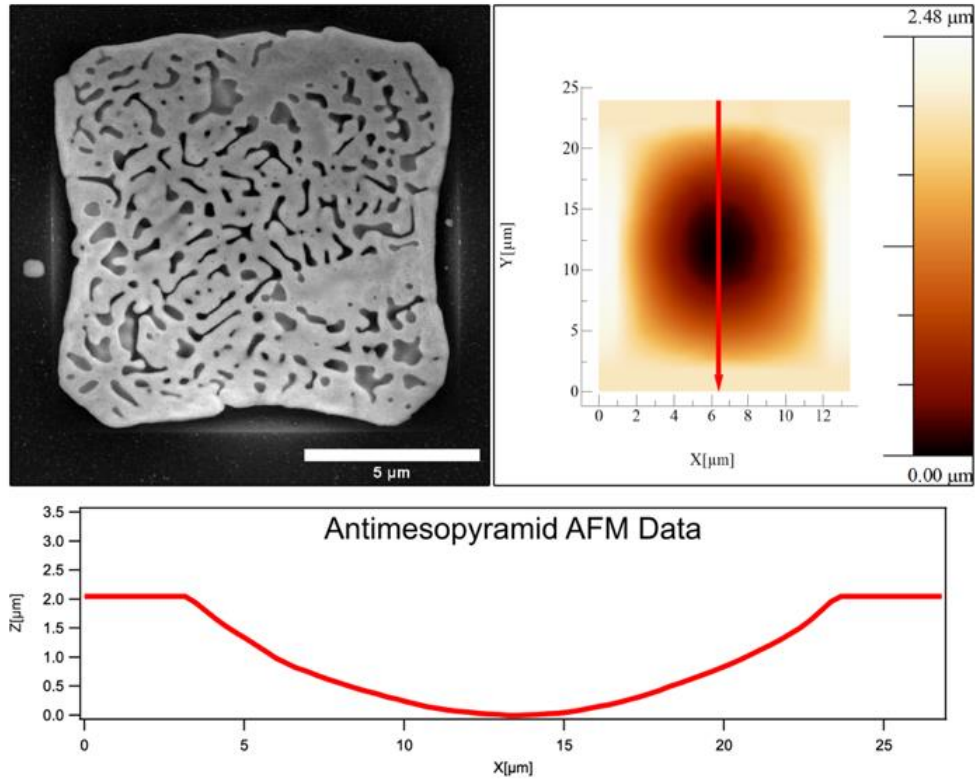


Figure 7.5 (a) An SEM of an inverse mesopyramid, (b) its corresponding atomic force microscopy profile, and (c) the line scan corresponding to the arrow in (b).

Next, we turn our attention to the geometry of the of the IMP. A note, we will only be discussing the geometry of the IMP as it pertains directly to its SPP signature. In the case of the MP, it is sufficient to say that the nanoscale dimensions of the cavities can be viewed as a planar feature with tens of nanometers of changes in its topography, where the resulting SPP into light is attributed to these slight changes in topography. The IMP profile is uniquely suited to facilitate in the couple of light to SPP mode when viewed with a long working distance objective. The

SEM/AFM characterization in Figure 7.5 is of the IMP for which SPP data presented here. The approximate dimensions of the IMP in Figure 7.5 are $20 \times 20 \text{ um}^2$ and 2 um deep. The AFM data is presented alongside a SEM micrograph in Figure 7.5. The bottom graph in Figure 7.5 is a depth profile line scan of the IMP taken from Figure 5(b). To illustrate the spherical profile of the IMP, the vertical axis is magnified. Due to the height differential of the IMP when focusing on the bottom of it, the optical path of incident light creates a principle and secondary beam path that when considered with the polarized nature of the incident light, effectively launches SPP [173]. A consequence of this is that the IMP must be positioned within a specific region of field of view to observe light emission associated with the scattering of SPP. The corresponding location within the field of view is illustrated in Figure 7.6. Interestingly, this location is not centered in the field of view. The blue bands are the areas within the field of view that SPP behavior is observed. More specifically, the green triangles are the facets of the IMP that we observe the signatures of SPP activity.

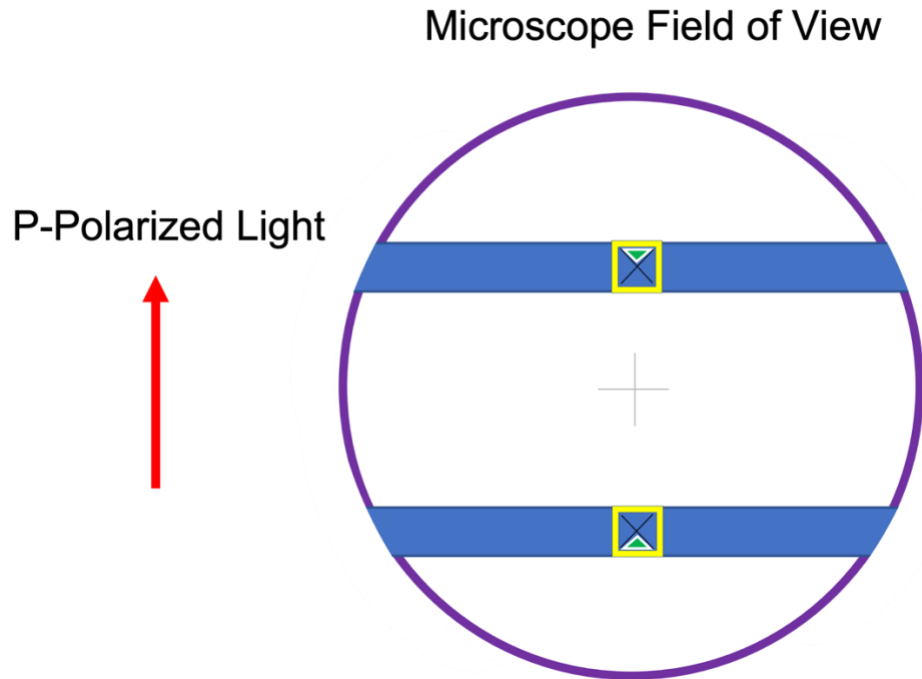


Figure 7.6 A schematic of the field of view of the microscope, where blue bands indicate areas within the field of view that SPP activity can be observed. The green triangles indicate the facets of the IMP that SPP behavior is observed. The red arrow indicates the direction of polarization of the light source.

For a given polarization, SPP activity is observed when the IMP is located in one to bands of the field of view that mirror one another. A corresponding change in the facet of the IMP that shows SPP activity also occurs. To further test/validate the observed optical effects dependent on the polarization of the light source, a key aspect of SPP excitation, the light source was rotated by 45° , i.e. the polarization of the light was rotated by 45° . Upon doing so, the observed phenomenon was only observed in bands of the field of view that are rotated 45° relative to those in Figure 7.6.

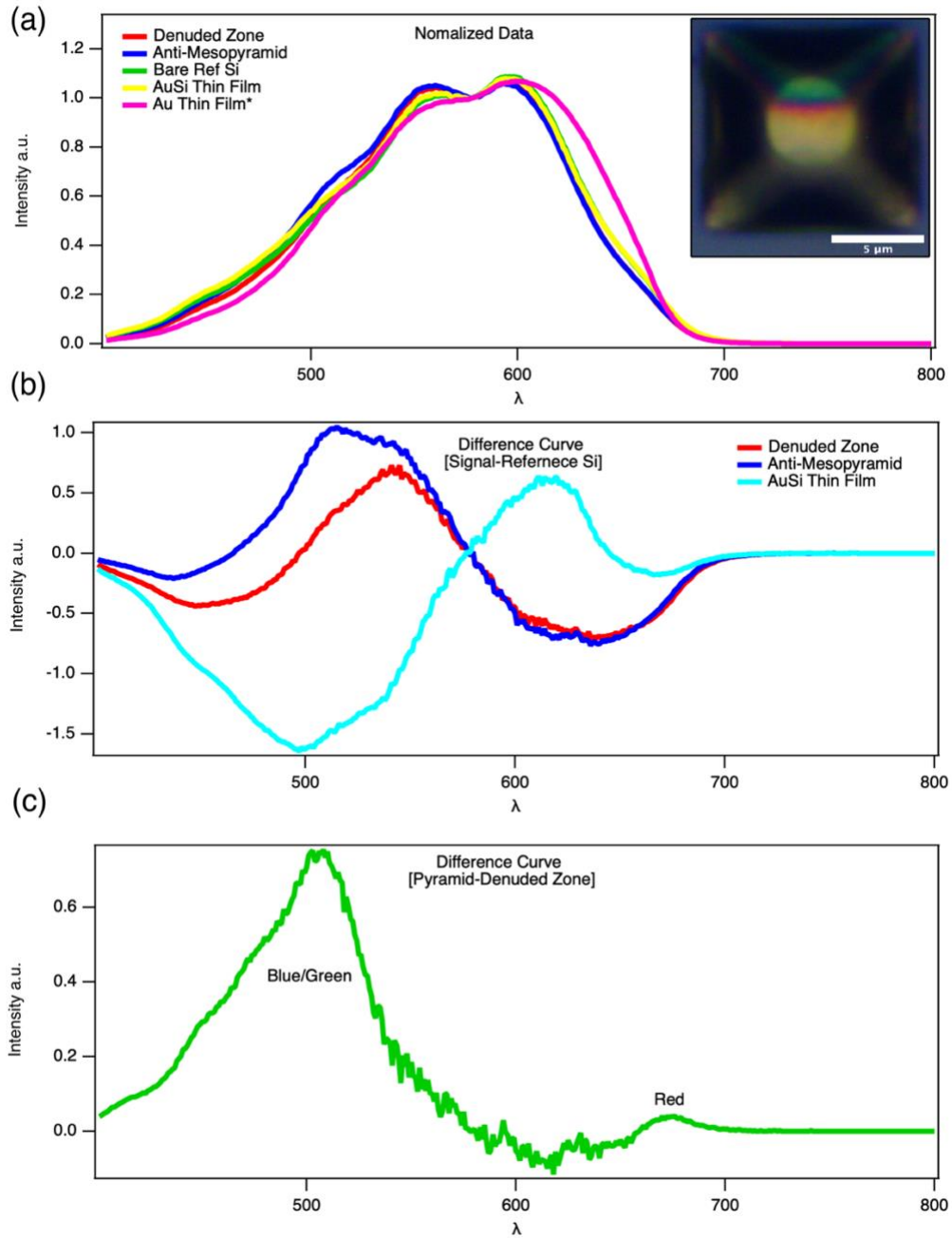


Figure 7.7 (a) Reflectivity spectra of a denuded zone, an IMP, a Si wafer, an AuSi tri-layer, and an Au thin film, (b) difference curves between the denuded zone, the IMP, and an AuSi tri-layer and the reference Si wafer spectrum, (c) a difference curve of the difference curves between the IMP and the denuded zone.

The reflectivity spectrum acquired with an incoherent p-polarized white light source of the IMP Figure 7.5 is displayed in Figure 7.7(a), where the inset is the optical image of the IMP. The incident and scattered light is being delivered and collected with a single long distance working objective with an angle of acceptance of roughly 37° . This narrow angle, coupled with the requirement that the focal point of the objective be below the IMP, limits the location of the IMP in the field of view for viewing SPP activity to the two bands in Figure 7.6. The order of the colors in these bands are another indication that the effects are likely due to SPP, as opposed to another optical effect. The predominance of the green and red are familiar wavelengths to the IMP. The presence of the blue between the red and green bands is inconsistent with the standard interference effect ones sees with soap bubbles, where the colors bands evolve from blue to green to red in accordance with a change in the wall thickness of the soap bubble from thinner to thicker. The slope of the IMP and the use of the long working distance objective allow one to observe SPP over a large area and, therefore, observe a broader range of wavelengths of scattered light [174], [175]. The spectrum in panel (a) is a collection of spectrums taken with different samples to perform a comparison of the optical properties of the IMP vs. the surrounding area, referred to as the denuded zone, contains residual Au that will have overlapping features with the IMP. The spectrum from the denuded zone can be subtracted from the IMP spectrum, as well as serve as a comparison spectrum for identifying spectral features unique to the IMP . In addition, reflectivity spectra were collected for the AuSi tri-layer, an Au film and a bare Si substrate. Once again, they are used as reference spectra either to normalize the IMP spectrum or for identifying unique features of the IMP spectrum. In Figure 7.7(b) three difference curves have been generated by subtracting the Si reference spectrum from the raw spectra of an AuSi tri-layer, an Au layer and the IMP. Note that the Au reference spectrum is for an as deposited film, i.e. unannealed. This was done to illustrate the differences between a planar film of Au and the IMP. In addition, in many SPP experiments, a continuous Au thin film is used to launch SPP [176]–

[181]. These films are considered to be semi-infinite and are the basis of a large body of theoretical work on SPP. Figure 7.7(c) is a difference curve of difference curves of the IMP and the DZ. This is the most important spectral data of this set up because it specifically represents the SPP phenomena on the surface of the IMP. A detailed discussion of the results will be covered in the next section.

Section 4: Discussion

In order to describe the mechanisms of SPP absorption and scattering of the Au mesopyramids, I will interpret the results for the MP and IMP separately and then reconcile them with one another. The rationale for this approach is differences in the geometry (convex vs. concave) the differences in the experimental setups used to probe their SPP properties. There are two conditions that must be met to effectively launch SPP on the surface of a dielectric/conductor interface such as an air/Au interface. The first is that the incident light must be frequency matched to that of the SPP one intends to excite. This condition is easily met with a broad-spectrum light source. The broad range of frequencies ensures that a component of the incident light matches that of the SP. The downside of this approach is the poor signal to noise ratio and why a monochromator is used in conjunction with lock-in detection and a photomultiplier tube for light detection. The second condition is a little more complicated to satisfy. To effectively couple photons to the Au conduction electrons, the component of the momentum or k-vector of the incident photon must be equal to the momentum of the SPP, where for a thin film this is achieved with an incident angle of the photon or resonance angle. This condition must be met when the system consists of a semi-infinite metallic planar surface and dielectric [38]. Simply put, the momentum at the interface must be conserved. There are two methods to conserve the k-vectors. One is to use a prism and p-polarized light incident at the correct angle relative to the normal to the dielectric conductor interface [158]–[162]. The other is to break up the surface of the thin film to break symmetry rules. This grating or defect ensemble creates a diffraction effect

of the incident light [163]–[168]. Components of the diffracted light that have wave a k-vector equal to that of the SPP can couple. This is referred to as non-resonance rough coupling. The surface topology of the MP and IMP achieve non-resonance rough coupling.

As was discussed in the experimental setup, the MP are imaged using a 100x oil immersion objective using a p-polarized white light source. The index matching oil eliminates the gradient of the index of refraction experienced when going from silica of the objective lens to air, thereby significantly improving resolution and the elimination of aberrations. The reader is referred to Figure 7.3. One of the characteristics of this type of lens is that it has a wide angle of acceptance or high numerical aperture. Taking this into consideration, the floors of these cavities can be treated as a semi-smooth surfaces with slight variations in pitch. These variations facilitate a secondary beam path when defocusing the objective, thus delivering light at a resonance angle that effectively couples to the SPP modes. This method of SPP launch has been reported Somekh et al. [173]. The use of white light, as well as the wide range of angles of incidence improves the efficiency of light-SPP coupling. It should also be noted that there are two colors observed for the MP using the oil immersion objective and that the wavelengths of these colors correspond to the SPP absorption modes at 550 nm and 650 nm in the reflectivity spectrum of a MP in Figure 7.4. Observing green or red in a particular region of a cavity is tentatively attributed to SPP scattering and the relative angle of the surface normal of the cavity relative to the optical axis of the objective. Closely examining the SEM micrographs in Figure 7.3(a) & (c), a correlation is observed between the location of the scattered light topological changes in the cavities. Furthermore, we argue that the reason why some of the cavities are inactive is either due to the fact that the light emitted by scattered SPP is outside of the angular acceptance of the objective or the k-vectors of the incidence doesn't match that of the SPP for those cavities. For the MP in Figure 7.3(b), the focal plane is the surface at the center of the MP. Therefore, the majority of the SPP activity is observed towards the center MP, while the edges are relatively inactive.

Alternatively, for the MP in Figure 7.4(d), the edges of the MP are the SPP areas and not the central area. Considering the k-vector of the transverse magnetic mode of the propagating SPP, any changes in the surface topography of a cavity will change the k-vector of the surface, which will cause SPP to scatter. Curved nano dimensional surfaces have long been used to launch and scatter surface plasmon polaritons [182]–[186].

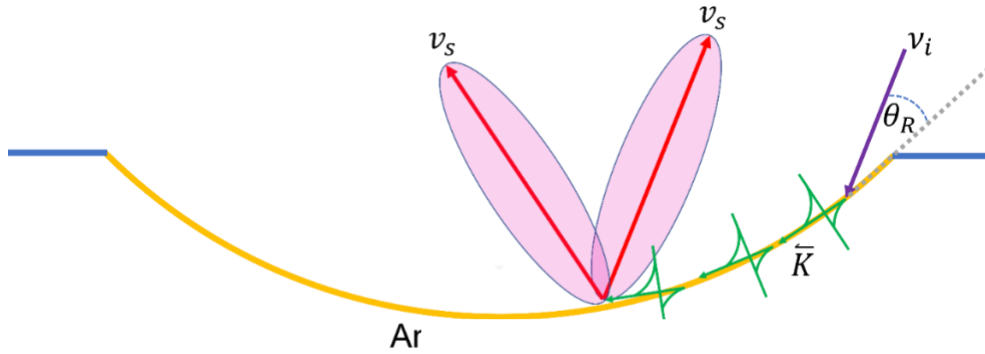


Figure 7.8 SPP Absorption and Scattering

At this point we will shift our discussion of SPP to scattering on the surface of IMP. Note that a long working distance objective was used for the experiments with the IMP. Per the earlier discussion, the acceptance angle for this object is almost half of that of the oil immersion lens. When viewing the IMP, the structure needed to be viewed within one of the two horizontal bands in the field of view (Figure 7.6). These bands correspond the secondary beam path of the objective. Within these bands, the p-polarized incident light was at the optimal angle to launch SPP. This setup in conjunction with rough coupling provided by the defect ensemble on the surface of the IMP fulfilled the frequency and wave vector requirements to launch SPP down a single facet. This was confirmed by moving the pyramid horizontal band in Figure 7.6. When this was done, the SPP behavior was observed on the opposite facet. Scattering of SPP occurs when the component of the k-vector of the SPP is no longer parallel to the interface between the IMP and the dielectric or air in this case. The observed light in the inset in Figure 7.7 is back scattered

light. The SPP scattering can be modeled as lobes or radiation patterns with the highest probability of detection [187]. Due to the curved profile of the IMP, as can be seen in the AFM depth profile scan in Figure 7.5, the light emitted by SPP scattering along the facet of the IMP is within the narrow cone of acceptance of the long working distance objective. Figure 7.7(c) is the spectral analysis of the SPP scattered emission spectrum. There is strong emission between 400-580 nm, which corresponds to the blue and green bands in the image of the IMP in the inset in Figure 7.7(a). Based on the AFM profile in Figure. 7.5 (c) of the IMP, we estimate that SPP are traveling as far as 5 μm before scattering. Propagation distances of surface plasmon polaritons of up to few centimeters have been reported [184]. The propagation of SPP over large distances has been an area of intense investigation and studies with a variety of experiment setups [188]–[192]. We hypothesize that the changes in the profile of the IMP, the discontinuities in its surface and the use of a long working distance objective are extremely efficient for launching and observing SPP. The wavelength range of light emitted by scattered SPP is likely due relaxation of electrons in the unoccupied Au sp band to the d-bands near the Fermi level near the X and L high symmetry points of the Au Brillouin zone [193].

Section 5: Conclusion

Mesopyramid and Inverse mesopyramids have been grown on a Si[100] substrate from a tri-layer of gold and silicon annealed in vacuo. These structures are striated with a stochastic distribution of nanoscale cavities that are a result of a phase separation of the AuSi eutectic. Imaging and spectroscopic probing of these structures under 100x magnification with both long working distance and oil immersion objectives allowed for a detailed investigation and analysis of their plasmonic properties. Examination of the MP using the oil immersion objective revealed areas of intense green (~520 nm) and red (~650 nm) light emission in cavities on their surface. Within these cavities, slight topological features are observed by SEM that correlated with the locations of the red and green emission. This is attributed to light coupling to SPP previously

observed in the reflectivity spectrum of a single mesopyramid. The ability to visually observe SPP is attributed to the large numerical aperture or wide angle of acceptance of the oil immersion objective that facilitates launching of SPP and amplification of SPP scattering into light due to the confinement created by the cavities on the surface of the MP. In the case of the inverse mesopyramid, SPP coupling, and scattering is indirectly observed over distances of up to 5 μm . The ability to indirectly observed SPP activity on the surface of the IMP is attributed to the use of a long-distance working objective and positioning the inverse mesopyramid in the secondary beam path of the objective, which effectively couple the incoming light to the SPP, as well as efficient collection of light emitted when SPP scatter. Due to the large area of plasmonic activity, spectroscopic reflectivity data was collected and analyzed by using a high-resolution monochromator, ultrasensitive photomultiplier tube for light detection and lock-in detection method. Due to the large number of defects in the surface of the IMP, wavevector matching of the incoming light with that of the SPP is easily achieved. The use of a broad band incoherent polarized white light source ensures frequency matching. The backscattered light observed on the surface of the IMP should be viewed as indirect evidence of SPP activity averaged over the a quadrant of its surface. Given the metalens-like texturing of these structures, I suggest that there are a wide variety of applications in optoelectronics where they could be used. Finding ways to change the properties of light with near 2D structures has the potential to greatly shrink the footprint of handheld devices or applications where space is a valuable commodity. Additionally, the focusing ability of the MP and IMP could find utility in momentum distribution or steering of solar sails.

CHAPTER VIII

CONCLUSION

The approach to this body research was to develop plasmonically active structures that efficiently couple light with the sea of electrons or plasma of electrons at the surface of Au mesostructures, thereby creating surface plasmon polaritons that propagate along their surface. We refer to these structures as mesopyramids or inverse mesopyramids for their obvious similarity to pyramids. The nanoscale topography of these structures in the form of plateaus and cavities in conjunction with the plasmonic character of Au is the motivation for utilizing them as metalenses and incorporating them into optoelectronic devices. By exploiting the behavior of the AuSi eutectic, I was able to develop a method for fabricating MP and IMP that lowered the thermal budget of the process. This provided impetus to obtain a provisional patent for these structures. My dissertation research began with addressing the reproducibility of pyramid growth or lack thereof. Initially, only a few pyramids grew on a 1 cm² Si substrate if they grew at all. I determined that the issue rested with the inability to form the AuSi eutectic and eutectic dynamics. I gained a better appreciation of the phase separation with the aid of SEM and EDS analysis. I identified the relationship between the native oxide of SiO₂ on the Si surface and surface tension of the eutectic by performing MP growth experiments with and without the native oxide. The conclusion is that a native oxide is necessary and without its MP formation at moderate temperatures (< 900 °C) is not possible. With this knowledge, I was able to determine

begin the entire cycle thermodynamic cycle of MP formation, as opposed the piecemeal approach previously undertaken by other researchers.

Now that MP could be regular produced and with a high density, I was able to analyze the elemental composition of the mesopyramids and its dependence to annealing temperature. I designed an experiment using MP samples produced with four different annealing temperatures. I used cross-sectional analysis and EDS data was generated annealing vs. composition map of the MP. EDS of the bulk elemental composition elucidated the ability for the eutectic to scavenge silicon from the substrate. This shed light on the fact that the substrate is an active participant in pyramid formation. Not only are the MP uniform aligned with the lattice structure of the Si(100) surface, but that the percentage of Si in the eutectics or silicon load capacity tracks the eutectic liquidus line of the binary phase diagram of the AuSi eutectic. The step in MP formation is the phase separation of Si and Au during the cool down portion of the MP growth process. In addition, the Si is reincorporated into the substrate, which is what leads to the nanoscale cavities in the surface, concomitant with the formation of plateaus, and through the bulk of the MP. These plateaus and cavities are well suited due to their sub-wavelength dimensions to interact with light, ergo, the launching of SPP.

The first optical measurement performed with the MP was a far field diffraction experiment. The experiments revealed that the light reflected off the MP produce Fraunhofer diffraction patterns. Modeling of the diffraction pattern revealed that the MP acts like a square aperture operating in transmission mode. During these experiments I discovered that I was not only producing MP but also inverse mesopyramids IMP, which have the same shape and surface topography of the MP but have a negative radius of curvature, i.e., are concave instead of convex. The differences in the diffraction patterns led to atomic force microscopy experiments that confirmed the existence of two configurations, the mesopyramid and the inverse mesopyramid. Modeling the structures as a square aperture with rounded edges provided an opportunity to

develop some basic coding skills and I was able to accurately reproduce the experimental diffraction patterns. The convex or concave surface profiles of the MP and IMP also affected the relative size of the diffraction pattern. The relative sizes of the Fraunhofer diffraction patterns revealed that the diffraction pattern produced by the IMP is magnified relative to the MP. This magnification is a function of IMP's concave profile but also the experimental parameters. Based on the AFM profiles of the MP and IMP, I determined that their profiles most closely matched a circle, i.e., they have a spherical profile. After determining the radii of curvatures of the MP and IMP, I used the theory of physical optics to determine their magnifying capabilities. I determined that the light source for the diffraction patterns was focused between $2f$ and f of the surface of the IMP, where f is the focal length of a mirror with the equivalent radius of curvature. For the MP that has a positive radius of curvature, it acts like a concave mirror that always creates a minified "virtual" image. My conclusion is that the MP and IMP can be modeled as square apertures constructed with lenses. With these results in mind, I was ready to turn my attention to SPP activity on the surfaces of the MP and IMP.

Finding ways to effectively launch SPP on the surface of the mesopyramids proved to be the most challenging part of dissertation. Again, it should be noted that this is a work in progress that those that come after me will have to complete. Therefore, the results presented in my dissertation of the SPP launching and scattering are a starting point for future research. The material presented represents the best explanations I have at this point in time. Returning the many challenges of this complex problem, I would like to point out a few challenges I encountered. There is a steep learning curve when breaking into the field of optics. There were many false positives in the early part of my dissertation that resulting in me developing a healthy level of skepticism of the results of my experiment that served me well. Switching to an oil immersion objective was a game changer because it allowed me to observe SPP activity in the cavities of the MP. The oil immersion objective increased the imaging resolution, thereby

revealing the green and red light being absorbed and reemitted from the bottom of the cavities on the surface of the MP. This data, coupled with SEM images of the surface of the MP lead to the identification of relationships between the angle of incidence of the incoming light and the launching of SPP and their eventual emission of light upon scattering. In addition, I postulate that the cavities act like resonators that amplify SPP scattering and subsequent emission of light. The propagation lengths of SPP inside the cavities is on the order of a micron. Reviewing the literature, I realized that it was possible to launch SPP much further. Switching to a single IMP, I again observed the signatures of SPP activity but over a large area relative to the MP. For the IMP I swapped out the 100x oil immersion lens for a 100x long working distance objective. In addition to the expected red and green light emission, blue light emission was also observed. The diffractive nature of the cavities, along with the concavity, produced a system that doesn't need to be operated at the tradition resonance angle in order to launch SPP. This effect is analogous to what is referred to as rough coupling, where surface roughness enhances the coupling of light to SPP. To ensure that this wasn't an aberration, the polarization of the light source was rotated by 90 degrees in order to demonstrate that the SPP activity required the light to be p-polarized relative to the orientation of the IMP. Because a large area of the IMP is SPP active, it was possible to acquire spectra of light emitted by scattered SPP. The spectrum verified light emission ranging from ~400nm to 650 nm, i.e., blue to green to red light. Being able to couple this data with spectra data provided ample support for my conclusions that the surfaces of the MP and IMP are highly SPP active.

The challenges when working in the field of SPP merits a few lines of consideration. Within the wide plasmonic community, there are a variety of experimental setups used to launch surface plasmon polaritons. Furthermore, there are a variety of methods for detecting SPP such as direct imaging using a digital camera vs. more robustly methods like reflection and transmission spectroscopy. Imaging of SPP is problematic and requires a bit of faith in one's results and

conclusions. Add to this the fact that there isn't a set of standards by which to claim successful launching or detection of SPP. Another contributing factor to this challenges of this field is the fact that much of the theory of SPP is based on a single infinite dielectric/conductor interface that is perfectly flat. These conditions are almost impossible to reproduce in the laboratory. Pushing the limits of classical electromagnetic theory to explain the many body physics of SPP is always going to have shortcomings. In a way, it worked to my advantage, causing me to scrutinize the arguments I was making based on the classical theory and to support the visual data with spectroscopic data that agreed with early reflectivity data, where SPP absorption bands were observed around 500 nm, 550 nm, and 650 nm. With the use of advanced detection techniques such as a photomultiplier tube and enhanced signal analysis tool like lock-in detection, I am confident we have demonstrated SPP absorption and scattering on the surfaces of the MP and IMP.

Looking forward there is plenty of room for continued development of the mesopyramids and inverse mesopyramids optical applications. Demonstration that these structures are capable of second harmonic generation is in the early stages. Another possible use of these mesostructures is for data encryption. The patterns the plateaus and cavities produce on the surface of a MP is unique to it, like a fingerprint. Using the pyramids as an optical key could be used to development encryption system that would be impossible to reproduce.

Another interesting area for future research is the engineering the MP and IMP SPP properties. Enhancement of their optical properties can be achieved by adding a dielectric or semiconducting adlayer on top of the surface of the mesopyramid. For instance, if the adlayer is a semiconductor, SPP may act as hot carriers that can be injected into the conduction band of the semiconductor, i.e. a hybrid rectifier. There is a wide variety of thin films that could be used for this purpose that have yet to be explored.

REFERENCES

- [1] A. V. Zayats, I. I. Smolyaninov, and A. A. Maradudin, “Nano-optics of surface plasmon polaritons,” *Physics Reports*, vol. 408, no. 3–4, pp. 131–314, Mar. 2005, doi: 10.1016/j.physrep.2004.11.001.
- [2] P. Simesen *et al.*, “Surface plasmon polariton excitation by second harmonic generation in single organic nanofibers,” *Opt. Express*, vol. 23, no. 12, p. 16356, Jun. 2015, doi: 10.1364/OE.23.016356.
- [3] Y. Li, M. Kang, J. Shi, K. Wu, S. Zhang, and H. Xu, “Transversely Divergent Second Harmonic Generation by Surface Plasmon Polaritons on Single Metallic Nanowires,” *Nano Lett.*, vol. 17, no. 12, pp. 7803–7808, Dec. 2017, doi: 10.1021/acs.nanolett.7b04016.
- [4] S. W. Bishnoi *et al.*, “SERS Biodetection Using Gold-Silica Nanoshells and Nitrocellulose Membranes,” *Analytical Chemistry*, p. 8, 2011.
- [5] “Development of an integrated single-fiber SERS sensor - ScienceDirect.” <https://www.sciencedirect.com/science/article/pii/S0925400500002914> (accessed Jan. 13, 2021).
- [6] “The Dawn of New Optics: Emerging Metamaterials | Features | Jan 2019 | Photonics Spectra.” https://www.photonics.com/Articles/The_Dawn_of_New_Optics_Emerging_Metamaterials/a64154 (accessed Jun. 30, 2020).
- [7] B. Ressel, K. C. Prince, S. Heun, and Y. Homma, “Wetting of Si surfaces by Au–Si liquid alloys,” *Journal of Applied Physics*, vol. 93, no. 7, pp. 3886–3892, Apr. 2003, doi: 10.1063/1.1558996.
- [8] H. S. Chen and D. Turnbull, “Thermal Properties of Gold-Silicon Binary Alloy near the Eutectic Composition,” *Journal of Applied Physics*, vol. 38, no. 9, pp. 3646–3650, Aug. 1967, doi: 10.1063/1.1710186.
- [9] G. Amato *et al.*, “Micro-IBA analysis of Au/Si eutectic ‘crop-circles,’” *Nuclear Instruments and Methods in Physics Research Section B: Beam Interactions with Materials and Atoms*, vol. 348, pp. 183–186, Apr. 2015, doi: 10.1016/j.nimb.2014.10.004.
- [10] J. Lee, W. Hasan, C. L. Stender, and T. W. Odom, “Pyramids: A Platform for Designing Multifunctional Plasmonic Particles,” *Acc. Chem. Res.*, vol. 41, no. 12, pp. 1762–1771, Dec. 2008, doi: 10.1021/ar800126p.
- [11] “Record-breaking metalens could revolutionize optical technologies.” <https://phys.org/news/2020-06-record-breaking-metalens-revolutionize-optical-technologies.html> (accessed Jun. 30, 2020).
- [12] “Metalenses at visible wavelengths: Diffraction-limited focusing and subwavelength resolution imaging | Science.” <https://science.sciencemag.org/content/352/6290/1190> (accessed May 25, 2021).

- [1] A. V. Zayats, I. I. Smolyaninov, and A. A. Maradudin, "Nano-optics of surface plasmon polaritons," *Physics Reports*, vol. 408, no. 3–4, pp. 131–314, Mar. 2005, doi: 10.1016/j.physrep.2004.11.001.
- [2] P. Simesen *et al.*, "Surface plasmon polariton excitation by second harmonic generation in single organic nanofibers," *Opt. Express*, vol. 23, no. 12, p. 16356, Jun. 2015, doi: 10.1364/OE.23.016356.
- [3] Y. Li, M. Kang, J. Shi, K. Wu, S. Zhang, and H. Xu, "Transversely Divergent Second Harmonic Generation by Surface Plasmon Polaritons on Single Metallic Nanowires," *Nano Lett.*, vol. 17, no. 12, pp. 7803–7808, Dec. 2017, doi: 10.1021/acs.nanolett.7b04016.
- [4] S. W. Bishnoi *et al.*, "SERS Biodetection Using Gold-Silica Nanoshells and Nitrocellulose Membranes," *Analytical Chemistry*, p. 8, 2011.
- [5] "Development of an integrated single-fiber SERS sensor - ScienceDirect." <https://www.sciencedirect.com/science/article/pii/S0925400500002914> (accessed Jan. 13, 2021).
- [6] "The Dawn of New Optics: Emerging Metamaterials | Features | Jan 2019 | Photonics Spectra." https://www.photonics.com/Articles/The_Dawn_of_New_Optics_Emerging_Metamaterials/a64154 (accessed Jun. 30, 2020).
- [7] B. Ressel, K. C. Prince, S. Heun, and Y. Homma, "Wetting of Si surfaces by Au–Si liquid alloys," *Journal of Applied Physics*, vol. 93, no. 7, pp. 3886–3892, Apr. 2003, doi: 10.1063/1.1558996.
- [8] H. S. Chen and D. Turnbull, "Thermal Properties of Gold-Silicon Binary Alloy near the Eutectic Composition," *Journal of Applied Physics*, vol. 38, no. 9, pp. 3646–3650, Aug. 1967, doi: 10.1063/1.1710186.
- [9] G. Amato *et al.*, "Micro-IBA analysis of Au/Si eutectic 'crop-circles,'" *Nuclear Instruments and Methods in Physics Research Section B: Beam Interactions with Materials and Atoms*, vol. 348, pp. 183–186, Apr. 2015, doi: 10.1016/j.nimb.2014.10.004.
- [10] J. Lee, W. Hasan, C. L. Stender, and T. W. Odom, "Pyramids: A Platform for Designing Multifunctional Plasmonic Particles," *Acc. Chem. Res.*, vol. 41, no. 12, pp. 1762–1771, Dec. 2008, doi: 10.1021/ar800126p.
- [11] "Record-breaking metalens could revolutionize optical technologies." <https://phys.org/news/2020-06-record-breaking-metalens-revolutionize-optical-technologies.html> (accessed Jun. 30, 2020).
- [12] "Metalenses at visible wavelengths: Diffraction-limited focusing and subwavelength resolution imaging | Science." <https://science.sciencemag.org/content/352/6290/1190> (accessed May 25, 2021).
- [13] "Ultrathin van der Waals Metalenses." <https://pubs.acs.org/action/cookieAbsent> (accessed Dec. 02, 2021).
- [14] "Imaging through Nonlinear Metalens Using Second Harmonic Generation - Schlickriede - 2018 - Advanced Materials - Wiley Online Library." <https://onlinelibrary.wiley.com/doi/full/10.1002/adma.201703843> (accessed Dec. 02, 2021).
- [15] M. L. Tseng *et al.*, "Metalenses: Advances and Applications," *Advanced Optical Materials*, vol. 6, no. 18, p. 1800554, Sep. 2018, doi: 10.1002/adom.201800554.

- [16] A. Afridi, J. Canet-Ferrer, L. Philippet, J. Osmond, P. Berto, and R. Quidant, “Electrically Driven Varifocal Silicon Metalens,” *ACS Photonics*, vol. 5, no. 11, pp. 4497–4503, Nov. 2018, doi: 10.1021/acsp Photonics.8b00948.
- [17] R. Wang *et al.*, “Multi-foci metalens for terahertz polarization detection,” *Opt. Lett.*, vol. 45, no. 13, p. 3506, Jul. 2020, doi: 10.1364/OL.395580.
- [18] C. Chen *et al.*, “On-chip monolithic wide-angle field-of-view metalens based on quadratic phase profile,” *AIP Advances*, vol. 10, no. 11, p. 115213, Nov. 2020, doi: 10.1063/5.0020329.
- [19] “Photonic crystal fiber metalens.” <https://www.degruyter.com/document/doi/10.1515/nanoph-2018-0204/html> (accessed Feb. 11, 2022).
- [20] W. Wang *et al.*, “Plasmonics metalens independent from the incident polarizations,” *Opt. Express*, vol. 23, no. 13, p. 16782, Jun. 2015, doi: 10.1364/OE.23.016782.
- [21] J. Chen *et al.*, “Tungsten Disulfide–Gold Nanohole Hybrid Metasurfaces for Nonlinear Metalenses in the Visible Region,” *Nano Lett.*, vol. 18, no. 2, pp. 1344–1350, Feb. 2018, doi: 10.1021/acs.nanolett.7b05033.
- [22] X. Ni, S. Ishii, A. V. Kildishev, and V. M. Shalaev, “Ultra-thin, planar, Babinet-inverted plasmonic metalenses,” *Light: Science & Applications*, vol. 2, no. 4, pp. e72–e72, Apr. 2013, doi: 10.1038/lsa.2013.28.
- [23] J. Luo *et al.*, “Tight focusing of radially and azimuthally polarized light with plasmonic metalens,” *Optics Communications*, vol. 356, pp. 445–450, Dec. 2015, doi: 10.1016/j.optcom.2015.08.025.
- [24] E. Prinz, G. Spektor, M. Hartelt, A.-K. Mahro, M. Aeschlimann, and M. Orenstein, “Functional Meta Lenses for Compound Plasmonic Vortex Field Generation and Control,” *Nano Lett.*, vol. 21, no. 9, pp. 3941–3946, May 2021, doi: 10.1021/acs.nanolett.1c00625.
- [25] J. Lin *et al.*, “Polarization-Controlled Tunable Directional Coupling of Surface Plasmon Polaritons,” *Science*, vol. 340, no. 6130, pp. 331–334, Apr. 2013, doi: 10.1126/science.1233746.
- [26] M. Stefan, *Plasmonics: Fundamentals and Applications*. United Kingdom: Springer Science, 2007.
- [27] B. D. Gupta and R. K. Verma, “Surface Plasmon Resonance-Based Fiber Optic Sensors: Principle, Probe Designs, and Some Applications,” *Journal of Sensors*, vol. 2009, pp. 1–12, 2009, doi: 10.1155/2009/979761.
- [28] “Surface plasmon-polariton amplifiers and lasers - ProQuest.” <https://www.proquest.com/docview/921585571/fulltextPDF/D185A8AEE79C47FEPQ/1?accountid=4117> (accessed Jul. 07, 2021).
- [29] “Surface plasmon–polariton length scales: a route to sub-wavelength optics - IOPscience.” <https://iopscience.iop.org/article/10.1088/1464-4258/8/4/S06/meta> (accessed Jan. 27, 2022).
- [30] “Surface-Plasmon Holography - ScienceDirect.” <https://www.sciencedirect.com/science/article/pii/S2589004220310762> (accessed Nov. 18, 2021).

- [31] F. Monticone, “A truly one-way lane for surface plasmon polaritons,” *Nat. Photonics*, vol. 14, no. 8, pp. 461–465, Aug. 2020, doi: 10.1038/s41566-020-0662-5.
- [32] “Leakage radiation microscopy of surface plasmon polaritons - ScienceDirect.” https://www.sciencedirect.com/science/article/abs/pii/S0921510707005995?casa_token=arlZu_EXkAIAAAAA:A76lF4uK7VjuO87X3l1n-0tpqp9W73RTojBm1xhmkuqPYD6TwWDKUkmzc-BWB0kgeyZMlyXB1w (accessed Feb. 28, 2022).
- [33] “Phys. Rev. B 51, 17916 (1995) - Near-field microscopy of surface-plasmon polaritons: Localization and internal interface imaging.” <https://journals.aps.org/prb/abstract/10.1103/PhysRevB.51.17916> (accessed Feb. 28, 2022).
- [34] “Surface plasmon resonance imaging | SpringerLink.” <https://link.springer.com/article/10.1007/s00216-004-2636-8> (accessed Feb. 28, 2022).
- [35] “Near-field photonics: surface plasmon polaritons and localized surface plasmons - IOPscience.” https://iopscience.iop.org/article/10.1088/1464-4258/5/4/353/meta?casa_token=xPr6Nfm0-A4AAAAA:YoVNMMFkdywGrINzTsd2bNSQ8yO7ohalfBuXKLi0fxEBoo6VjhwOtB75slk4gWRU4DGckEBJI2S1j39Kg6c (accessed Feb. 28, 2022).
- [36] “Near-Field Visualization of Strongly Confined Surface Plasmon Polaritons in Metal–Insulator–Metal Waveguides | Nano Letters.” https://pubs.acs.org/doi/abs/10.1021/nl801781g?casa_token=7Fw0A9JrT6UAAA:AA:Zg3q42MUcsbydr4U3lRnV3oF67KKhIwUVmM7As2dg2gGmrqsYus20Le05QvC8Zcr-qrVwHt72aCRGKA (accessed Feb. 28, 2022).
- [37] “Phys. Rev. B 51, 17916 (1995) - Near-field microscopy of surface-plasmon polaritons: Localization and internal interface imaging.” <https://journals.aps.org/prb/abstract/10.1103/PhysRevB.51.17916> (accessed Feb. 28, 2022).
- [38] A. V. Zayats, I. I. Smolyaninov, and A. A. Maradudin, “Nano-optics of surface plasmon polaritons,” *Physics Reports*, vol. 408, no. 3–4, pp. 131–314, Mar. 2005, doi: 10.1016/j.physrep.2004.11.001.
- [39] W. Zhou, R. P. Apkarian, Z. L. Wang, and D. Joy, “Fundamentals of Scanning Electron Microscopy,” p. 40.
- [40] “Compound magnetic and electrostatic lenses for low-voltage applications: Journal of Vacuum Science & Technology B: Microelectronics Processing and Phenomena: Vol 7, No 6.” <https://avs.scitation.org/doi/abs/10.1116/1.584683> (accessed Jan. 21, 2022).
- [41] S. J. Lim and J. H. Kang, “An Analysis for the Performance of Condenser Lens in SEM,” p. 2, 2010.
- [42] “Energy Dispersive X-ray Spectroscopy | SpringerLink.” https://link.springer.com/chapter/10.1007/978-4-431-66988-3_4 (accessed Jan. 27, 2022).
- [43] “Is Scanning Electron Microscopy/Energy Dispersive X-ray Spectrometry (SEM/EDS) Quantitative? - Newbury* - 2013 - Scanning - Wiley Online Library.”

- <https://onlinelibrary.wiley.com/doi/full/10.1002/sca.21041> (accessed Jan. 27, 2022).
- [44] W. Gerlaci-I and B. Goel, "GOLD SILICON PHASE DIAGRAM," p. 4.
- [45] "Rev. Mod. Phys. 75, 949 (2003) - Advances in atomic force microscopy." <https://journals.aps.org/rmp/abstract/10.1103/RevModPhys.75.949> (accessed Jan. 31, 2022).
- [46] "Dynamic atomic force microscopy methods - ScienceDirect." <https://www.sciencedirect.com/science/article/pii/S0167572902000778> (accessed Jan. 31, 2022).
- [47] "Atomic force microscopy - ScienceDirect." <https://www.sciencedirect.com/science/article/pii/0079681692900097> (accessed Jan. 31, 2022).
- [48] "Atomic Force Microscopy | SpringerLink." https://link.springer.com/article/10.1007/s00897960059a?error=cookies_not_supported&code=627cbdb2-8432-4e28-a49b-4516165c00f1 (accessed Jan. 31, 2022).
- [49] T. S. Matthews, C. Sawyer, D. F. Ogletree, Z. Liliental-Weber, D. C. Chrzan, and J. Wu, "Large Reaction Rate Enhancement in Formation of Ultrathin AuSi Eutectic Layers," *Physical Review Letters*, vol. 108, no. 9, Mar. 2012, doi: 10.1103/PhysRevLett.108.096102.
- [50] J. S. Wu, Y. F. Chen, S. Dhara, C. T. Wu, K. H. Chen, and L. C. Chen, "Interface energy of Au₇Si grown in the interfacial layer of truncated hexagonal dipyramidal Au nanoislands on polycrystalline-silicon," *Applied Physics Letters*, vol. 82, no. 25, pp. 4468–4470, Jun. 2003, doi: 10.1063/1.1586997.
- [51] K. Sekar, G. Kuri, P. V. Satyam, B. Sundaravel, D. P. Mahapatra, and B. N. Dev, "Growth and alignment of gold silicide islands on Br-passivated vicinal Si(111) surfaces," *Surface Science*, vol. 339, no. 1–2, pp. 96–104, Sep. 1995, doi: 10.1016/0039-6028(95)00606-0.
- [52] M. L. Munford, F. Maroun, R. Cortès, P. Allongue, and A. A. Pasa, "Electrochemical growth of gold on well-defined vicinal H–Si(111) surfaces studied by AFM and XRD," *Surface Science*, vol. 537, no. 1–3, pp. 95–112, Jul. 2003, doi: 10.1016/S0039-6028(03)00563-6.
- [53] "The Influence of Deposition Rate on the Structure and Morphology of Gold/Si...: EBSCOhost." <https://web.b.ebscohost.com/ehost/detail/detail?vid=0&sid=ffcca2a9-565d-4f0d-9243-556b6b68cc30%40sessionmgr102&bdata=JnNpdGU9ZWwhvc3QtbGl2ZQ%3d%3d> (accessed May 20, 2021).
- [54] "Silver- and Gold-Ordered Structures on Single-Crystal Silicon Surface After Thermal Deposition | Nanoscale Research Letters | Full Text." <https://nanoscalereslett.springeropen.com/articles/10.1186/s11671-016-1291-2> (accessed May 20, 2021).
- [55] "Strain mapping on gold thin film buckling and silicon blistering (Conference) | OSTI.GOV." <https://www.osti.gov/biblio/883781-oyTpOw/> (accessed May 20, 2021).
- [56] N. L. Abbott, A. Kumar, and G. M. Whitesides, "Using Micromachining, Molecular Self-Assembly, and Wet Etching to Fabricate 0.1-1- μ m-scale

- structures of Gold and Silicon,” *Chem. Mater.*, vol. 6, no. 5, pp. 596–602, May 1994, doi: 10.1021/cm00041a007.
- [57] J. K. N. Lindner, D. Bahloul-Hourlier, D. Kraus, M. Weigl, T. Mélin, and B. Stritzker, “TEM characterization of Si nanowires grown by CVD on Si pre-structured by nanosphere lithography,” *Materials Science in Semiconductor Processing*, vol. 11, no. 5–6, pp. 169–174, Oct. 2008, doi: 10.1016/j.mssp.2008.09.016.
- [58] D. Kim, A. L. Giermann, and C. V. Thompson, “Solid-state dewetting of patterned thin films,” *Appl. Phys. Lett.*, vol. 95, no. 25, p. 251903, Dec. 2009, doi: 10.1063/1.3268477.
- [59] C. Chang and G. Ottaviani, “Outdiffusion of Si through gold films: The effects of Si orientation, gold deposition techniques and rates, and annealing ambients,” *Appl. Phys. Lett.*, vol. 44, no. 9, pp. 901–903, May 1984, doi: 10.1063/1.94928.
- [60] W. R. Wilcox and T. J. LaChapelle, “Mechanism of Gold Diffusion into Silicon,” p. 8.
- [61] W. Lerch and N. A. Stolwijk, “Diffusion of gold in silicon during rapid thermal annealing: Effectiveness of the surface as a sink for self-interstitials,” *Journal of Applied Physics*, vol. 83, no. 3, pp. 1312–1320, Feb. 1998, doi: 10.1063/1.366831.
- [62] F. H. Baumann and W. Schröter, “Precipitation of gold into metastable gold silicide in silicon,” *Phys. Rev. B*, vol. 43, no. 8, pp. 6510–6519, Mar. 1991, doi: 10.1103/PhysRevB.43.6510.
- [63] F. Ruffino, A. Canino, M. G. Grimaldi, F. Giannazzo, F. Roccaforte, and V. Raineri, “Kinetic mechanism of the thermal-induced self-organization of Au/Si nanodroplets on Si(100): Size and roughness evolution,” *Journal of Applied Physics*, vol. 104, no. 2, p. 024310, Jul. 2008, doi: 10.1063/1.2955784.
- [64] A. Hiraki, M. Nicolet, and J. W. Mayer, “LOW-TEMPERATURE MIGRATION OF SILICON IN THIN LAYERS OF GOLD AND PLATINUM,” *Appl. Phys. Lett.*, vol. 18, no. 5, pp. 178–181, Mar. 1971, doi: 10.1063/1.1653615.
- [65] J. Knall, J.-E. Sundgren, G. V. Hansson, and J. E. Greene, “Indium overlayers on clean Si(100)2 x 1: Surface structure, nucleation, and growth,” *Surface Science Letters*, vol. 166, no. 2–3, p. A51, Feb. 1986, doi: 10.1016/0167-2584(86)90933-3.
- [66] Y. M. Shao, T. X. Nie, Z. M. Jiang, and J. Zou, “Behavior of Au-Si droplets in Si(001) at high temperatures,” *Appl. Phys. Lett.*, vol. 101, no. 5, p. 053104, Jul. 2012, doi: 10.1063/1.4739413.
- [67] P. Nagpal, N. C. Lindquist, S.-H. Oh, and D. J. Norris, “Ultrasoother Patterned Metals for Plasmonics and Metamaterials,” *Science*, vol. 325, no. 5940, pp. 594–597, Jul. 2009, doi: 10.1126/science.1174655.
- [68] G. T. Boyd, Z. H. Yu, and Y. R. Shen, “Photoinduced luminescence from the noble metals and its enhancement on roughened surfaces,” *Physical Review B*, vol. 33, no. 12, pp. 7923–7936, Jun. 1986, doi: 10.1103/PhysRevB.33.7923.
- [69] K. Imura, T. Nagahara, and H. Okamoto, “Plasmon Mode Imaging of Single Gold Nanorods,” *Journal of the American Chemical Society*, vol. 126, no. 40, pp. 12730–12731, Oct. 2004, doi: 10.1021/ja047836c.
- [70] H. Wang *et al.*, “The role of Rabi splitting tuning in the dynamics of strongly coupled J-aggregates and surface plasmon polaritons in nanohole arrays,” *Nanoscale*, vol. 8, no. 27, pp. 13445–13453, 2016, doi: 10.1039/C6NR01588C.

- [71] H. Gao *et al.*, “Rayleigh anomaly-surface plasmon polariton resonances in palladium and gold subwavelength hole arrays,” *Optics Express*, vol. 17, no. 4, p. 2334, Feb. 2009, doi: 10.1364/OE.17.002334.
- [72] J. M. McMahon, J. Henzie, T. W. Odom, G. C. Schatz, and S. K. Gray, “Tailoring the sensing capabilities of nanohole arrays in gold films with Rayleigh anomaly-surface plasmon polaritons,” *Optics Express*, vol. 15, no. 26, p. 18119, 2007, doi: 10.1364/OE.15.018119.
- [73] H. Gao, J. Henzie, and T. W. Odom, “Direct Evidence for Surface Plasmon-Mediated Enhanced Light Transmission through Metallic Nanohole Arrays,” *Nano Letters*, vol. 6, no. 9, pp. 2104–2108, Sep. 2006, doi: 10.1021/nl061670r.
- [74] M. Khorasaninejad, W. T. Chen, R. C. Devlin, J. Oh, A. Y. Zhu, and F. Capasso, “Metalenses at visible wavelengths: Diffraction-limited focusing and subwavelength resolution imaging,” *Science*, vol. 352, no. 6290, pp. 1190–1194, Jun. 2016, doi: 10.1126/science.aaf6644.
- [75] M. Khorasaninejad and F. Capasso, “Metalenses: Versatile multifunctional photonic components,” *Science*, vol. 358, no. 6367, p. eaam8100, Dec. 2017, doi: 10.1126/science.aam8100.
- [76] J. Valente, J.-Y. Ou, E. Plum, I. J. Youngs, and N. I. Zheludev, “Reconfiguring photonic metamaterials with currents and magnetic fields,” *Applied Physics Letters*, vol. 106, no. 11, p. 111905, Mar. 2015, doi: 10.1063/1.4913609.
- [77] N. Nandan, T. S. Saini, A. Kumar, and R. K. Sinha, “Design and analysis of chevrons shaped split ring resonator in the mid-infrared region,” San Diego, California, United States, Sep. 2015, p. 95441D. doi: 10.1117/12.2188341.
- [78] J. Valente, “Fabrication of planar nanomechanical photonic metamaterials,” *Journal of Optics*, vol. 20, no. 9, p. 093501, Sep. 2018, doi: 10.1088/2040-8986/aad8d6.
- [79] X. Chen *et al.*, “Dual-polarity plasmonic metalens for visible light,” *Nature Communications*, vol. 3, no. 1, Jan. 2012, doi: 10.1038/ncomms2207.
- [80] S. Mechler *et al.*, “Self-Consistent Interpretation of the 2D Structure of the Liquid Au 82 Si 18 Surface: Bending Rigidity and the Debye-Waller Effect,” *Phys. Rev. Lett.*, vol. 105, no. 18, p. 186101, Oct. 2010, doi: 10.1103/PhysRevLett.105.186101.
- [81] “Nano-textured metallic surfaces for optical sensing and detection applications - ScienceDirect.”
<https://www.sciencedirect.com/science/article/pii/S1010603008004218> (accessed Aug. 26, 2020).
- [82] N. C. Lindquist, P. Nagpal, A. Lesuffleur, D. J. Norris, and S.-H. Oh, “Three-Dimensional Plasmonic Nanofocusing,” *Nano Lett.*, vol. 10, no. 4, pp. 1369–1373, Apr. 2010, doi: 10.1021/nl904294u.
- [83] C. S. Hwang, Ed., *Atomic Layer Deposition for Semiconductors*. Boston, MA: Springer US, 2014. doi: 10.1007/978-1-4614-8054-9.
- [84] A. A. Alwattari and D. R. Lloyd, “Microporous membrane formation via thermally-induced phase separation. VI. Effect of diluent morphology and relative crystallization kinetics on polypropylene membrane structure,” *Journal of Membrane Science*, vol. 64, no. 1–2, pp. 55–67, Nov. 1991, doi: 10.1016/0376-7388(91)80077-J.

- [85] M. A. Brady, G. M. Su, and M. L. Chabynyc, “Recent progress in the morphology of bulk heterojunction photovoltaics,” *Soft Matter*, vol. 7, no. 23, p. 11065, 2011, doi: 10.1039/c1sm06147j.
- [86] D. G. Moore, L. Barbera, K. Masania, and A. R. Studart, “Three-dimensional printing of multicomponent glasses using phase-separating resins,” *Nat. Mater.*, vol. 19, no. 2, pp. 212–217, Feb. 2020, doi: 10.1038/s41563-019-0525-y.
- [87] H. Lee, C. Park, D. H. Sin, J. H. Park, and K. Cho, “Recent Advances in Morphology Optimization for Organic Photovoltaics,” *Adv. Mater.*, vol. 30, no. 34, p. 1800453, Aug. 2018, doi: 10.1002/adma.201800453.
- [88] Y. Wang, Z. Liu, B. Han, Z. Sun, J. Zhang, and D. Sun, “Phase-Separation-Induced Micropatterned Polymer Surfaces and Their Applications,” *Adv. Funct. Mater.*, vol. 15, no. 4, pp. 655–663, Apr. 2005, doi: 10.1002/adfm.200400201.
- [89] B. R. Crenshaw and C. Weder, “Phase Separation of Excimer-Forming Fluorescent Dyes and Amorphous Polymers: A Versatile Mechanism for Sensor Applications,” *Adv. Mater.*, vol. 17, no. 12, pp. 1471–1476, Jun. 2005, doi: 10.1002/adma.200401688.
- [90] A. Sundar, P. Farzinpour, K. D. Gilroy, T. Tan, R. A. Hughes, and S. Neretina, “Eutectic Combinations as a Pathway to the Formation of Substrate-Based Au-Ge Heterodimers and Hollowed Au Nanocrescents with Tunable Optical Properties,” *Small*, vol. 10, no. 16, pp. 3379–3388, Aug. 2014, doi: 10.1002/sml.201400383.
- [91] T. Buonassisi *et al.*, “Transition metal co-precipitation mechanisms in silicon,” *Acta Materialia*, vol. 55, no. 18, pp. 6119–6126, Oct. 2007, doi: 10.1016/j.actamat.2007.07.030.
- [92] B. Wei, D. M. Herlach, B. Feuerbacher, and F. Sommer, “Dendritic and eutectic solidification of undercooled Co–Sb alloys,” *Acta Metallurgica et Materialia*, vol. 41, no. 6, pp. 1801–1809, Jun. 1993, doi: 10.1016/0956-7151(93)90200-C.
- [93] F. Misják, P. B. Barna, and G. Radnóczy, “Growth of nanocomposite in eutectic Cu–Ag films,” *Thin Solid Films*, vol. 518, no. 15, pp. 4247–4251, May 2010, doi: 10.1016/j.tsf.2009.12.095.
- [94] A. Munitz, M. J. Kaufman, and R. Abbaschian, “Liquid phase separation in transition element high entropy alloys,” *Intermetallics*, vol. 86, pp. 59–72, Jul. 2017, doi: 10.1016/j.intermet.2017.03.015.
- [95] D. M. Shah, D. L. Anton, D. P. Pope, and S. Chin, “In-situ refractory intermetallic-based composites,” *Materials Science and Engineering: A*, vol. 192–193, pp. 658–672, Feb. 1995, doi: 10.1016/0921-5093(95)03318-1.
- [96] E. J. Sullivan, J. A. Tomko, J. M. Skelton, J. M. Fitz-Gerald, P. E. Hopkins, and J. A. Floro, “Lamellar instabilities during scanning laser melting of Al–Cu eutectic and hypoeutectic thin films,” *Journal of Alloys and Compounds*, vol. 865, p. 158800, Jun. 2021, doi: 10.1016/j.jallcom.2021.158800.
- [97] D. Mukherji, G. Pigozzi, F. Schmitz, O. Näth, J. Rösler, and G. Kosterz, “Nanostructured materials produced from simple metallic alloys by phase separation,” *Nanotechnology*, vol. 16, no. 10, pp. 2176–2187, Oct. 2005, doi: 10.1088/0957-4484/16/10/034.
- [98] J. H. Lee and J. D. Verhoeven, “Eutectic formation in the Ni–Al system,” *Journal of Crystal Growth*, vol. 143, no. 1–2, pp. 86–102, Oct. 1994, doi: 10.1016/0022-0248(94)90371-9.

- [99] M. A. Marcus, "Phase separation and crystallization in amorphous Pd-Si-Sb," *Journal of Non-Crystalline Solids*, vol. 30, no. 3, pp. 317–335, Jan. 1979, doi: 10.1016/0022-3093(79)90170-4.
- [100] Y. Takamatsu, H. Esaka, and K. Shinozuka, "Liquid-Phase Separation in the Interdendritic Region After Growth of Primary β -Sn in Undercooled Sn-2.8Ag-0.3Cu Melt," *Journal of Elec Materi*, vol. 41, no. 8, pp. 2035–2044, Aug. 2012, doi: 10.1007/s11664-012-2075-9.
- [101] "Silicide formation of Au thin films on (1 0 0) Si during annealing - ScienceDirect." <https://www.sciencedirect.com/science/article/pii/S0254058403002402> (accessed Sep. 21, 2021).
- [102] A. K. Green and E. Bauer, "Formation, structure, and orientation of gold silicide on gold surfaces," *Journal of Applied Physics*, vol. 47, no. 4, pp. 1284–1291, Apr. 1976, doi: 10.1063/1.322827.
- [103] H. Okamoto, "The Au–Si (Gold-Silicon) system," *Bulletin of Alloy Phase Diagrams*, vol. 4, no. 198, 1983, [Online]. Available: <https://doi.org/10.1007/BF02884878>
- [104] F. Ruffino, L. Romano, G. Pitruzzello, and M. G. Grimaldi, "High-temperature annealing of thin Au films on Si: Growth of SiO₂ nanowires or Au dendritic nanostructures?," *Appl. Phys. Lett.*, vol. 100, no. 5, p. 053102, Jan. 2012, doi: 10.1063/1.3679614.
- [105] "Nanosprings: Applied Physics Letters: Vol 79, No 10." <https://aip.scitation.org/doi/10.1063/1.1400079> (accessed Jul. 29, 2021).
- [106] "Silicon Carbide Nanosprings | Nano Letters." <https://pubs.acs.org/doi/abs/10.1021/nl034288c> (accessed Oct. 19, 2021).
- [107] "Gold nanorods: Synthesis, characterization and applications - ScienceDirect." <https://www.sciencedirect.com/science/article/pii/S0010854505000287> (accessed Oct. 19, 2021).
- [108] W. Lu and C. M. Lieber, "Semiconductor nanowires," *J. Phys. D: Appl. Phys.*, vol. 39, no. 21, pp. R387–R406, Nov. 2006, doi: 10.1088/0022-3727/39/21/R01.
- [109] "Vertical phase separation in spin-coated films of a low bandgap polyfluorene/PCBM blend—Effects of specific substrate interaction - ScienceDirect." <https://www.sciencedirect.com/science/article/pii/S0169433206011172> (accessed Sep. 21, 2021).
- [110] "Phys. Rev. E 72, 051801 (2005) - Evidence for vertical phase separation in densely grafted, high-molecular-weight poly(N-isopropylacrylamide) brushes in water." <https://journals.aps.org/pre/abstract/10.1103/PhysRevE.72.051801> (accessed Sep. 21, 2021).
- [111] "Damping of the localized surface plasmon polariton resonance of gold nanoparticles | SpringerLink." https://link.springer.com/article/10.1007/s00340-010-4064-0?error=cookies_not_supported&code=2a1aa007-9099-4710-b9cb-b3dd8a23bf99 (accessed Sep. 21, 2021).
- [112] "Ultrafast dephasing time of localized surface plasmon polariton resonance and the involved damping mechanisms in colloidal gold nanoparticles - ScienceDirect."

- <https://www.sciencedirect.com/science/article/pii/S0079681607000214> (accessed Sep. 21, 2021).
- [113] “Surface plasmon polariton beam focusing with parabolic nanoparticle chains.” <https://www.osapublishing.org/oe/fulltext.cfm?uri=oe-15-11-6576&id=134709> (accessed Sep. 21, 2021).
- [114] “Tailoring the sensing capabilities of nanohole arrays in gold films with Rayleigh anomaly-surface plasmon polaritons.” <https://www.osapublishing.org/oe/fulltext.cfm?uri=oe-15-26-18119&id=148572> (accessed Sep. 21, 2021).
- [115] “Optical characterisation of gold using surface plasmon-polaritons - IOPscience.” <https://iopscience.iop.org/article/10.1088/0305-4608/17/1/031/meta> (accessed Sep. 21, 2021).
- [116] “Scattering of surface plasmon-polaritons and volume waves by thin gold films | SpringerLink.” https://link.springer.com/article/10.1134/S0030400X10040120?error=cookies_not_supported&code=46bd1f04-57fd-471e-b442-6681832db474 (accessed Sep. 21, 2021).
- [117] “Exploiting eutectic formation and phase separation to produce plasmonic metamaterials: Journal of Applied Physics: Vol 130, No 12.” <https://aip.scitation.org/doi/10.1063/5.0060713> (accessed Oct. 13, 2021).
- [118] “Au-Si phase diagram [4]. | Download Scientific Diagram.” https://www.researchgate.net/figure/Au-Si-phase-diagram-4_fig1_4058572 (accessed Jan. 12, 2021).
- [119] N. Dice, A. J. Austin, and D. McIlroy, “Exploiting eutectic formation and phase separation to produce plasmonic metamaterials,” *Journal of Applied Physics*, vol. 130, no. 12, p. 125307, Sep. 2021, doi: 10.1063/5.0060713.
- [120] Y. Ishikawa, T. Saito, M. Sakashita, N. Shibata, and S. Zaima, “Formation of Au and AuSi_x-Pyramids in Separation by Implanted Oxygen Wafers with Si Pillars in SiO₂ Layer,” *Jpn. J. Appl. Phys.*, vol. 34, no. 11A, p. L1478, Nov. 1995, doi: 10.7567/JJAP.34.L1478.
- [121] P. M. Wojcik, P. V. Bakharev, G. Corti, and D. N. McIlroy, “Nucleation, evolution, and growth dynamics of amorphous silica nanosprings,” *Mater. Res. Express*, vol. 4, no. 1, p. 015004, Jan. 2017, doi: 10.1088/2053-1591/aa54dc.
- [122] D. Kim, A. L. Giermann, and C. V. Thompson, “Solid-state dewetting of patterned thin films,” *Appl. Phys. Lett.*, vol. 95, no. 25, p. 251903, Dec. 2009, doi: 10.1063/1.3268477.
- [123] D. N. McIlroy, D. Zhang, Y. Kranov, and M. G. Norton, “Nanosprings,” *Appl. Phys. Lett.*, vol. 79, no. 10, p. 1540, 2001, doi: 10.1063/1.1400079.
- [124] M. Zhang *et al.*, “Metastable phase formation in the Au-Si system via ultrafast nanocalorimetry,” *Journal of Applied Physics*, vol. 111, no. 9, p. 093516, May 2012, doi: 10.1063/1.4712342.
- [125] J. W. Arblaster, “Thermodynamic Properties of Gold,” *J. Phase Equilib. Diffus.*, vol. 37, no. 2, pp. 229–245, Apr. 2016, doi: 10.1007/s11669-016-0449-z.
- [126] E. P. Donovan, F. Spaepen, D. Turnbull, J. M. Poate, and D. C. Jacobson, “Calorimetric studies of crystallization and relaxation of amorphous Si and Ge

- prepared by ion implantation,” *Journal of Applied Physics*, vol. 57, no. 6, pp. 1795–1804, Mar. 1985, doi: 10.1063/1.334406.
- [127] P. Richet, Y. Bottinga, L. Denielou, J. P. Petitet, and C. Tequi, “Thermodynamic properties of quartz, cristobalite and amorphous SiO₂: drop calorimetry measurements between 1000 and 1800 K and a review from 0 to 2000 K,” *Geochimica et Cosmochimica Acta*, vol. 46, no. 12, pp. 2639–2658, Dec. 1982, doi: 10.1016/0016-7037(82)90383-0.
- [128] T. S. Matthews, C. Sawyer, D. F. Ogletree, Z. Liliental-Weber, D. C. Chrzan, and J. Wu, “Large Reaction Rate Enhancement in Formation of Ultrathin AuSi Eutectic Layers,” *Phys. Rev. Lett.*, vol. 108, no. 9, p. 096102, Mar. 2012, doi: 10.1103/PhysRevLett.108.096102.
- [129] I. Beszedá, E. G. Gontier-Moya, and Á. W. Imre, “Surface Ostwald-ripening and evaporation of gold beaded films on sapphire,” *Appl. Phys. A*, vol. 81, no. 4, pp. 673–677, Sep. 2005, doi: 10.1007/s00339-005-3254-9.
- [130] P. W. Voorhees, “The theory of Ostwald ripening,” *J Stat Phys*, vol. 38, no. 1–2, pp. 231–252, Jan. 1985, doi: 10.1007/BF01017860.
- [131] L. Ratke and P. W. Voorhees, *Growth and coarsening: Ostwald ripening in material processing*. Berlin ; New York: Springer, 2002.
- [132] S. Curiotto, F. Cheynis, F. Leroy, and P. Müller, “Surface diffusion of Au on 3 × 3 Si(111)–Au studied by nucleation-rate and Ostwald-ripening analysis,” *Surface Science*, vol. 647, pp. 8–11, May 2016, doi: 10.1016/j.susc.2015.11.015.
- [133] N. Ferralis, R. Maboudian, and C. Carraro, “Temperature-Induced Self-Pinning and Nanolayering of AuSi Eutectic Droplets,” *Journal of the American Chemical Society*, vol. 130, no. 8, pp. 2681–2685, Feb. 2008, doi: 10.1021/ja7101983.
- [134] M. K. Hazra, S. Sarkar, and B. Bagchi, “Three-stage phase separation kinetics in a model liquid binary mixture: A computational study,” *J. Chem. Phys.*, vol. 150, no. 14, p. 144501, Apr. 2019, doi: 10.1063/1.5055371.
- [135] “Theory of spinodal decomposition in alloys - ScienceDirect.”
<https://www.sciencedirect.com/science/article/pii/000349167190162X> (accessed Jul. 21, 2021).
- [136] K. Binder, “Theory of first-order phase transitions,” *Rep. Prog. Phys.*, vol. 50, no. 7, pp. 783–859, Jul. 1987, doi: 10.1088/0034-4885/50/7/001.
- [137] “Phys. Rev. A 11, 1417 (1975) - New computational method in the theory of spinodal decomposition.”
<https://journals.aps.org/pr/abstract/10.1103/PhysRevA.11.1417> (accessed Oct. 18, 2021).
- [138] “Exploiting eutectic formation and phase separation to produce plasmonic metamaterials: Journal of Applied Physics: Vol 130, No 12.”
<https://aip.scitation.org/doi/full/10.1063/5.0060713> (accessed Oct. 06, 2021).
- [139] “Frontiers | Exploration, novelty, surprise, and free energy minimization | Psychology.”
https://www.frontiersin.org/articles/10.3389/fpsyg.2013.00710/full?utm_source=newsletter&utm_medium=email&utm_campaign=Psychology-w42-2013 (accessed Jun. 15, 2021).
- [140] “Solved: The Mystery of the Nanoscale Crop Circles | Berkeley Lab.”
<https://newscenter.lbl.gov/2012/03/01/crop-circles/> (accessed Jun. 22, 2021).

- [141] J. S. Wu, Y. F. Chen, S. Dhara, C. T. Wu, K. H. Chen, and L. C. Chen, "Interface energy of Au₇Si grown in the interfacial layer of truncated hexagonal dipyramidal Au nanoislands on polycrystalline-silicon," *Appl. Phys. Lett.*, vol. 82, no. 25, pp. 4468–4470, Jun. 2003, doi: 10.1063/1.1586997.
- [142] R. P. Anantatmula, A. A. Johnson, S. P. Gupta, and R. J. Horylev, "The gold-silicon phase diagram," *JEM*, vol. 4, no. 3, pp. 445–463, Jun. 1975, doi: 10.1007/BF02666229.
- [143] M. Abouie, Q. Liu, and D. G. Ivey, "Eutectic and solid-state wafer bonding of silicon with gold," *Materials Science and Engineering: B*, vol. 177, no. 20, pp. 1748–1758, Dec. 2012, doi: 10.1016/j.mseb.2012.09.005.
- [144] B. Bokhonov and M. Korchagin, "In situ investigation of stage of the formation of eutectic alloys in Si–Au and Si–Al systems," *Journal of Alloys and Compounds*, vol. 312, no. 1–2, pp. 238–250, Nov. 2000, doi: 10.1016/S0925-8388(00)01173-7.
- [145] K. Oura, V. Lifshits, A. Zotov, and M. Katayama, *Surface Science An Introduction*, vol. First. Springer US, 1965.
- [146] "The crystal growth of silicon in Al-Si alloys | SpringerLink." <https://link.springer.com/article/10.1007/BF01112278> (accessed Dec. 02, 2021).
- [147] "Growth morphology of primary silicon in cast Al–Si alloys and the mechanism of concentric growth - ScienceDirect." <https://www.sciencedirect.com/science/article/pii/S0022024899003474> (accessed Dec. 02, 2021).
- [148] "The Relationship of Alpha and Beta Silicon Carbide - IOPscience." <https://iopscience.iop.org/article/10.1149/1.2779671/meta> (accessed Dec. 02, 2021).
- [149] J. Uozumi, H. Kimura, and T. Asakura, "Fraunhofer Diffraction by Koch Fractals: The Dimensionality," *Journal of Modern Optics*, vol. 38, no. 7, pp. 1335–1347, Jul. 1991, doi: 10.1080/09500349114551501.
- [150] Y. P. Feng *et al.*, "X-ray Fraunhofer diffraction patterns from a thin-film waveguide," *Appl. Phys. Lett.*, vol. 67, no. 24, pp. 3647–3649, Dec. 1995, doi: 10.1063/1.115346.
- [151] "Fraunhofer diffraction patterns from apertures illuminated with nonparallel light in nonsymmetrical Fourier transformers." <https://www.osapublishing.org/ao/fulltext.cfm?uri=ao-24-10-1549&id=61627> (accessed Nov. 02, 2021).
- [152] K. Patorski, "Fraunhofer Diffraction Patterns of Titled Planar Objects," *Optica Acta: International Journal of Optics*, vol. 30, no. 5, pp. 673–679, May 1983, doi: 10.1080/713821241.
- [153] M. F. Guasti and M. D. L. C. Heredia, "Diffraction Pattern of a Circle/square Aperture," *Journal of Modern Optics*, vol. 40, no. 6, pp. 1073–1080, Jun. 1993, doi: 10.1080/09500349314551141.
- [154] "Diffraction Pattern of a Circle/square Aperture: Journal of Modern Optics: Vol 40, No 6." <https://www.tandfonline.com/doi/abs/10.1080/09500349314551141> (accessed Aug. 30, 2021).
- [155] "Fresnel diffraction by a square aperture with rough edge - ScienceDirect." <https://www.sciencedirect.com/science/article/pii/S0030402615006531> (accessed Nov. 02, 2021).

- [156] T. Nakano and S. Kawata, “Numerical Analysis of the Near-field Diffraction Pattern of a Small Aperture,” *Journal of Modern Optics*, vol. 39, no. 3, pp. 645–661, Mar. 1992, doi: 10.1080/09500349214550611.
- [157] E. Hecht and A. Zajac, *Optics*. 1979.
- [158] “Experimental observation of the long-range surface-plasmon polariton.” <https://opg.optica.org/ol/fulltext.cfm?uri=ol-8-7-380&id=60013> (accessed Mar. 10, 2022).
- [159] “Phys. Rev. B 27, 1401(R) (1983) - Raman scattering mediated by surface-plasmon polariton resonance.” <https://journals.aps.org/prb/abstract/10.1103/PhysRevB.27.1401> (accessed Mar. 10, 2022).
- [160] “Phys. Rev. Lett. 101, 116801 (2008) - Coherent Exciton--Surface-Plasmon-Polariton Interaction in Hybrid Metal-Semiconductor Nanostructures.” <https://journals.aps.org/prl/abstract/10.1103/PhysRevLett.101.116801> (accessed Mar. 10, 2022).
- [161] “Spectral sensitivity of two-dimensional nanohole array surface plasmon polariton resonance sensor: Applied Physics Letters: Vol 91, No 12.” <https://aip.scitation.org/doi/full/10.1063/1.2789181> (accessed Mar. 10, 2022).
- [162] “Surface Plasmon Polariton Resonance of Gold, Silver, and Copper Studied in the Kretschmann Geometry: Dependence on Wavelength, Angle of Incidence, and Film Thickness | Journal of the Physical Society of Japan.” <https://journals.jps.jp/doi/full/10.7566/JPSJ.86.124721> (accessed Mar. 10, 2022).
- [163] “Design optimization of nano-grating surface plasmon resonance sensors.” <https://opg.optica.org/oe/fulltext.cfm?uri=oe-14-11-4842&id=90078> (accessed Mar. 10, 2022).
- [164] “Development of a prototype gas sensor using surface plasmon resonance on gratings - ScienceDirect.” <https://www.sciencedirect.com/science/article/pii/S092540059300871U> (accessed Mar. 10, 2022).
- [165] “Phys. Rev. Lett. 21, 1530 (1968) - Surface-Plasmon Resonance Effect in Grating Diffraction.” <https://journals.aps.org/prl/abstract/10.1103/PhysRevLett.21.1530> (accessed Mar. 10, 2022).
- [166] “Sensors | Free Full-Text | Theory and Applications of Surface Plasmon Resonance, Resonant Mirror, Resonant Waveguide Grating, and Dual Polarization Interferometry Biosensors.” <https://www.mdpi.com/1424-8220/10/11/9630> (accessed Mar. 10, 2022).
- [167] “Surface Plasmon Resonance Imaging of Biomolecular Interactions on a Grating-Based Sensor Array | Analytical Chemistry.” <https://pubs.acs.org/doi/abs/10.1021/ac0519209> (accessed Mar. 10, 2022).
- [168] “Surface plasmon resonance sensors based on diffraction gratings and prism couplers: sensitivity comparison - ScienceDirect.” <https://www.sciencedirect.com/science/article/pii/S0925400598003220> (accessed Mar. 10, 2022).
- [169] “Surface Plasmon Nanophotonics - Google Books.” <https://books.google.com/books?hl=en&lr=&id=7QLHU->

- 2QRSQC&oi=fnd&pg=PR7&dq=Surface+Plasmon+polariton+nanophotonics&ots=eK28RtCMf_&sig=fOKRqubySJbqKdj4OyIyNllv_E0 (accessed Jan. 27, 2022).
- [170] “Surface Plasmon Launching by Polariton Superradiance | ACS Photonics.” <https://pubs.acs.org/doi/abs/10.1021/acsphotonics.9b00193> (accessed Nov. 18, 2021).
- [171] “Surface Plasmon Polariton Resonance of Gold, Silver, and Copper Studied in the Kretschmann Geometry: Dependence on Wavelength, Angle of Incidence, and Film Thickness | Journal of the Physical Society of Japan.” <https://journals.jps.jp/doi/full/10.7566/JPSJ.86.124721> (accessed Jan. 28, 2022).
- [172] T. Søndergaard and S. I. Bozhevolnyi, “Surface plasmon polariton scattering by a small particle placed near a metal surface: An analytical study,” *Phys. Rev. B*, vol. 69, no. 4, p. 045422, Jan. 2004, doi: 10.1103/PhysRevB.69.045422.
- [173] M. G. Somekh, S. G. Liu, T. S. Velinov, and C. W. See, “Optical $V(z)$ for high-resolution 2π surface plasmon microscopy,” *Opt. Lett.*, vol. 25, no. 11, p. 823, Jun. 2000, doi: 10.1364/OL.25.000823.
- [174] “Phys. Rev. B 63, 205410 (2001) - Surface plasmon polariton propagation length: A direct comparison using photon scanning tunneling microscopy and attenuated total reflection.” <https://journals.aps.org/prb/abstract/10.1103/PhysRevB.63.205410> (accessed Mar. 07, 2022).
- [175] “Phys. Rev. Lett. 86, 3008 (2001) - Waveguiding in Surface Plasmon Polariton Band Gap Structures.” <https://journals.aps.org/prl/abstract/10.1103/PhysRevLett.86.3008> (accessed Mar. 07, 2022).
- [176] “Coupling efficiency of light to surface plasmon polariton for single subwavelength holes in a gold film.” <https://opg.optica.org/oe/abstract.cfm?uri=OE-16-5-3420> (accessed Mar. 07, 2022).
- [177] “High-Quality Ultrathin Gold Layers with an APTMS Adhesion for Optimal Performance of Surface Plasmon Polariton-Based Devices | ACS Applied Materials & Interfaces.” <https://pubs.acs.org/doi/abs/10.1021/acsami.7b07181> (accessed Mar. 07, 2022).
- [178] “Phys. Rev. B 75, 245405 (2007) - Theoretical analysis of dielectric-loaded surface plasmon-polariton waveguides.” <https://journals.aps.org/prb/abstract/10.1103/PhysRevB.75.245405> (accessed Mar. 07, 2022).
- [179] “Phys. Rev. B 78, 115115 (2008) - Efficiency of local surface plasmon polariton excitation on ridges.” <https://journals.aps.org/prb/abstract/10.1103/PhysRevB.78.115115> (accessed Mar. 07, 2022).
- [180] “Phys. Rev. Lett. 86, 3008 (2001) - Waveguiding in Surface Plasmon Polariton Band Gap Structures.” <https://journals.aps.org/prl/abstract/10.1103/PhysRevLett.86.3008> (accessed Mar. 07, 2022).

- [181] “Polymer-based surface-plasmon-polariton stripe waveguides at telecommunication wavelengths: Applied Physics Letters: Vol 82, No 5.” <https://aip.scitation.org/doi/abs/10.1063/1.1542944> (accessed Mar. 07, 2022).
- [182] “Curved long-range surface plasmon-polariton waveguides.” <https://opg.optica.org/oe/abstract.cfm?uri=OE-14-6-2365> (accessed Mar. 09, 2022).
- [183] “Dispersion relation of surface plasmon wave propagating along a curved metal-dielectric interface.” <https://opg.optica.org/oe/fulltext.cfm?uri=oe-16-7-4945&id=156863> (accessed Mar. 09, 2022).
- [184] “Leaky modes of curved long-range surface plasmon-polariton waveguide.” <https://opg.optica.org/oe/fulltext.cfm?uri=oe-14-26-13043&id=121423> (accessed Mar. 09, 2022).
- [185] “Photonic Hook Plasmons: A New Curved Surface Wave - Minin - 2018 - Annalen der Physik - Wiley Online Library.” <https://onlinelibrary.wiley.com/doi/full/10.1002/andp.201800359> (accessed Mar. 09, 2022).
- [186] “Surface plasmon polaritons on curved surfaces.” <https://opg.optica.org/optica/fulltext.cfm?uri=optica-6-1-115&id=404099> (accessed Mar. 09, 2022).
- [187] “Direct Radiations of Surface Plasmon Polariton Waves by Gradient Groove Depth and Flaring Metal Structure | IEEE Journals & Magazine | IEEE Xplore.” <https://ieeexplore.ieee.org/abstract/document/7254129> (accessed Jan. 06, 2022).
- [188] “Thermally Activated Variable Attenuation of Long-Range Surface Plasmon-Polariton Waves.” <https://opg.optica.org/jlt/abstract.cfm?uri=jlt-24-11-4391> (accessed Mar. 10, 2022).
- [189] “Integrated optical gyroscope using active Long-range surface plasmon-polariton waveguide resonator | Scientific Reports.” <https://www.nature.com/articles/srep03855> (accessed Mar. 10, 2022).
- [190] “Experimental observation of the long-range surface-plasmon polariton.” <https://opg.optica.org/ol/fulltext.cfm?uri=ol-8-7-380&id=60013> (accessed Mar. 10, 2022).
- [191] “Characterization of long-range surface-plasmon-polariton waveguides: Journal of Applied Physics: Vol 98, No 4.” <https://aip.scitation.org/doi/full/10.1063/1.2008385> (accessed Mar. 10, 2022).
- [192] “Curved long-range surface plasmon-polariton waveguides.” Accessed: Mar. 09, 2022. [Online]. Available: <https://opg.optica.org/oe/abstract.cfm?uri=OE-14-6-2365>
- [193] “Phys. Rev. B 33, 7923 (1986) - Photoinduced luminescence from the noble metals and its enhancement on roughened surfaces.” <https://journals.aps.org/prb/abstract/10.1103/PhysRevB.33.7923> (accessed Mar. 10, 2022).

APPENDICES

22159.00892

ASSIGNMENT

WHEREAS we, **David N. McIlroy** of 3823 Timberline Dr., Stillwater, Oklahoma 74074 and **Nathan P. Dice** of 14023 West 32nd Ave., Stillwater, Oklahoma 74074 (hereinafter "ASSIGNORS"), have made a certain invention titled "**GOLD-SILICIDE EUTECTICS AND ITS ROLE IN MESO-PYRAMID FORMATION**" for which a Provisional Patent Application was filed on October 29, 2020, and assigned Application Serial No. 63/107,300 (the "APPLICATION"); and

WHEREAS, we, ASSIGNORS hereby declare that we believe we are the original inventors of a claimed invention in the APPLICATION and in any patent application that claims priority to said APPLICATION;

WHEREAS, we, ASSIGNORS, hereby declare that the APPLICATION was made or authorized to be made by us;

WHEREAS, we, ASSIGNORS, hereby acknowledge that any willful false statements made in the above declarations is punishable under 18 U.S.C. 1001 by fine or imprisonment of not more than five (5) years, or both;

WHEREAS, **THE BOARD OF REGENTS FOR THE OKLAHOMA AGRICULTURAL AND MECHANICAL COLLEGES**, a body corporate located at 5th Floor Student Union, Stillwater, Oklahoma 74078, acting for and on behalf of OKLAHOMA STATE UNIVERSITY (hereinafter "ASSIGNEE"), is desirous of acquiring all right, title and interest in and to said APPLICATION and the invention described therein, and in and to any patents that may be granted based on the APPLICATION and on any patent application claiming priority to the APPLICATION or to which the APPLICATION claims priority from in the United States and its territorial possessions and in any and all foreign countries;

NOW, THEREFORE, in exchange of mutual promises and other consideration received, the receipt and sufficiency of which are hereby acknowledged, ASSIGNORS have sold, assigned and transferred, and by these presents do hereby sell, assign and transfer unto ASSIGNEE, our entire right, title and interest in and to said APPLICATION and the invention covered thereby in the United States of America and its territorial possessions and in all foreign countries, and the entire right, title and interest in and to any and all patents which may be granted based on any such patent application in the United States and its territorial possessions and in any and all foreign countries, and in and to any and all divisions, reissues, re-examinations, continuations


and extensions thereof, together with the right to sue and obtain damages for past, present and future infringement.

ASSIGNORS hereby covenant that no assignment, sale agreement or encumbrance has been or will be made or entered into which would conflict with this assignment.

ASSIGNORS further covenant that ASSIGNEE will, upon its request, be provided promptly with all pertinent facts and documents relating to said inventions and patents and/or patent applications represented thereby and legal equivalents as may be known and accessible to ASSIGNORS and will testify as to the same in any interference, litigation, or proceeding related thereof and will promptly execute and deliver to ASSIGNEE or its legal representatives any and all papers, instruments or affidavits necessary or desirable to ASSIGNORS to apply for, obtain, maintain, issue and enforce said application, said invention and said Letters Patent and said equivalents thereof.


Executed by the undersigned on the date indicated.

ASSIGNORS:



David N. McIlroy
1/21/20

Date



Nathan P. Dice
21 Jan 2021

Date



Funding: Funding provided by the Office of Naval Research (N00014-20-1-2433) and the Air Force Office of Scientific Research (G10004087).

Special Thanks to OSU Microscopy Lab. Specifically I want to thank Lisa Whitworth and Brent Johnson who helped generate all the AFM, SEM and EDS data in this body of work.

VITA

Nathan Philip Dice

Candidate for the Degree of

Doctor of Philosophy

Thesis: GOLD-SILICIDE EUTECTIC DYNAMICS OF MESOTEXTURED MATERIALS AND THEIR OPTICAL PROPERTIES

Major Field: Physics

Biographical:

Education:

Completed the requirements for the Doctor of Philosophy in your major at Oklahoma State University, Stillwater, Oklahoma in May of 2022. Completed the requirements for the Bachelor of Science in Physics at University of Idaho, Moscow, Idaho in August of 2018.

Experience:

Thin Films Scientist at Micron Inc. Boise, Idaho. Starting June 2022. Graduate Research Assistant at Oklahoma State University 2018-2022. Undergraduate Research Assistant at the University of Idaho 2015-2018. US Navy Corpsman 1st Marines 4th Battalion 2010-2015.

Publication:

Exploiting Eutectics Formation and Phase Separation to Produce Plasmonic Metamaterials. Published in the Journal of Applied Physics. Gold Silicide Eutectics Dynamics and Meso Pyramid Formation- Manuscript Under Consideration for Publication. Far-Field Diffraction Patterns from Meso-Scaled Pyramids- Manuscript Under Edit for Publication. Surface Plasmon Polaritons Absorption and Scattering Facilitated by Nano-scaled Topography of Mesopyramids and Inverse Mesopyramids- Manuscript Under Edit for Publication. Boron-induced metamorphosis of graphitic structures - a new form of mesoscopic carbon - ScienceDirect. Published in Carbon Trends

Miscellaneous:

Patent: US Provisional Patent "Gold-Silicide Eutectics and its Roles in Meso Pyramid Formation" No. 63/107,300. Bilingual: Speak, read, and write Brazilian Portuguese.